Spectroscopy of the Runaway B-Star HIP 60350

DIPLOMA THESIS

of

Andreas Irrgang

from

Cham, Germany

Performed at the

Dr. Karl Remeis-Observatory Bamberg
(Astronomical Institute of the University of Erlangen-Nuremberg)
Sternwartstraße 7, 96049 Bamberg

Supervised by

Prof. Dr. Ulrich Heber
PD. Dr. Norbert Przybilla

November 2009

Abstract

Young, massive stars in the Galactic halo are widely supposed to be the result of an ejection event from the Galactic disk forcing some stars to leave their place of birth as so-called runaway stars. In this thesis, a detailed spectroscopic and kinematic analysis of the runaway B-star HIP 60350 is presented to determine which runaway scenario – a supernova explosion disrupting a binary system or dynamical interaction in star clusters – may be responsible for HIP 60350's peculiar orbit.

A short introduction in Chapter 1 explaining the scientific motivation for this work is followed by a general astrophysical overview giving the necessary background information in Chapter 2. The main topics therein are classification, structure and evolution of stars putting special emphasis on B-type stars, nucleosynthesis, the structure of the Milky Way and runaway stars. Chapter 3 deals with astronomy's most powerful tool: spectroscopy. After discussing the procedure of data reduction and some practical aspects of spectrum optimization, the theoretical background of radiation transfer and its numerical solution is explained. Atmospheric parameters and their effects on the emitted spectrum are introduced and their determination by comparison with synthetic models is demonstrated. In Chapter 4, these techniques are applied to the runaway candidate HIP 60350 to derive atmospheric as well as stellar parameters which are essential for the remainder of the work. Using these outcomes, Chapter 5 illustrates the finding of the full phase space information of HIP 60350 with focus on the determination of the distance to the star and depicts the subsequent orbit computations intended to gain some indications of possible ejection scenarios. Among others, it is found that HIP 60350 qualifies as solid hyper-runaway candidate, i.e., a runaway star gravitationally unbound to the Milky Way. Chapter 6 discusses the pros and cons of the two competitive runaway scenarios in the light of the previous results and shows that both can account for the observations depending on the interpretation of the deduced abundance pattern. Finally, Chapter 7 briefly summarizes the results and gives a short outlook of what might follow.

Zusammenfassung

Junge, massereiche Sterne im Halo der Milchstraße sind nach gängiger Meinung die Folge eines Ejektionsereignisses aus der galaktischen Scheibe, welches einige Sterne zwingt, ihren Geburtsort als sogenannte Runaway Sterne (entweichende Sterne) zu verlassen. Diese Arbeit präsentiert eine detaillierte spektroskopische und kinematische Analyse des Runaway B-Sterns HIP 60350. Ziel ist es, herauszufinden, welches Szenario – eine Supernova Explosion in einem Doppelsternsystem oder dynamische Wechselwirkungen in Sternhaufen – für die ungewöhnliche Bahnkurve von HIP 60350 verantwortlich sein könnte.

Nach einer kurzen Einleitung in Kapitel 1, welche die wissenschaftliche Motivation dieser Arbeit erläutert, wird in Kapitel 2 eine allgemeine Einführung in die Astrophysik mit allen relevanten Hintergrundinformationen gegeben. Die wichtigsten Themen darin sind Klassifizierung, Aufbau und Entwicklung von Sternen, wobei besonderes Augenmerk auf Sterne des Typs B gelegt wird, sowie Nukleosynthese, die Struktur der Milchstraße und Runaway Sterne. Kapitel 3 behandelt das mächtigste Werkzeug der Astronomie: Spektroskopie. Nachdem die Datenreduktion und einige praktische Aspekte der Spektrumsoptimierung abgehandelt worden sind, werden die theoretischen Grundlagen des Strahlungstransportes und seine numerische Lösung erklärt. Atmosphärische Parameter und ihre Effekte auf das abgestrahlte Spektrum werden eingeführt und ihre Bestimmung anhand des Vergleichs mit synthetischen Modellen erläutert. Diese Analysetechniken werden in Kapitel 4 auf den Runaway Kandidaten HIP 60350 angewandt, um sowohl Atmosphären- als auch Sternparameter abzuleiten, die die Grundlage für den Rest der Arbeit bilden. Anhand dieser Ergebnisse wird in Kapitel 5 die komplette Phasenrauminformation von HIP 60350 bestimmt, wobei der Fokus auf der Entfernungsbestimmung des Sterns liegt. Darüber hinaus werden die anschließenden Berechnungen der Bahnkurve präsentiert, welche dazu dienen, Hinweise auf mögliche Ejektionsszenarien zu erhalten. Ein Ergebnis ist unter anderem, dass HIP 60350 als ernsthafter Kandidat für einen Hyper-Runaway Stern, d.h. ein Runaway Stern, der nicht gravitativ an die Milchstraße gebunden ist, gelten kann. Kapitel 6 diskutiert die Vor- und Nachteile der beiden konkurrierenden Ejektions-Szenarien im Angesicht der vorherigen Resultate und zeigt, dass je nach Interpretation des abgeleiteten Häufigkeitsmusters beide für die Beobachtungen verantwortlich sein können. Schließlich werden die Ergebnisse in Kapitel 7 knapp zusammengefasst und ein kurzer Ausblick über nötige Nachfolgeuntersuchungen gegeben.

Contents

1 Introduction

Astronomy is the oldest of all sciences. Its origins can be traced back to the early dawn of mankind, long before the first words were written down. Dealing with phenomena ranging from experiences of everyday life like the phases of the moon, over advanced observations and descriptions of, e.g., planetary motion or stellar evolution to the most fundamental question about the genesis of the whole universe, astronomy has fascinated people all along. However, its social role has changed significantly over the course of time: From being the basis for religious rituals and prophecies it developed to a practical tool, for instance helping to precisely forecast the seasons for the sake of agriculture or to determine positions in seafaring. It also led to radical changes in the world view such as Earth's displacement from the center of the universe resulting in a redefinition of the position of mankind in it. Today, astronomy is rather a pure and fundamental than practical science trying to satisfy man's wish to understand more and more the basic principles of nature and the universe.

To celebrate the outstanding astronomical contributions to society and culture the International Astronomical Union together with the United Nations proclaimed the year 2009 as the International Year of Astronomy. True to the slogan "The Universe, Yours to discover" it pursues among others the goal of arousing the interest of people to astronomical observation and to provide a modern image of this still evolving field of science. This particular year was chosen as it marks the 400th anniversary of the first astronomical observation through a telescope by Galileo Galilei and the publication of Johannes Kepler's "Astronomia nova", giving for the first time a correct description of the motion of the planets. Due to great minds like them and steadily improving telescopes awesome discoveries have been made since then and one can be confident that a lot more will follow: Ambitious plans for ever larger telescopes such as the European Extremely Large Telescope exist, opening up the opportunity to explore the first objects in the universe or the nature and distribution of dark matter or energy, respectively.

This exciting year 2009 seems to be just the right time to perform my diploma thesis at the Dr. Karl Remeis-Observatory in Bamberg. The motivation for this work is a discovery made here at the Remeis-Observatory and published last year: Heber et al. (2008) found the young, massive star HD 271791 to travel through the halo of our Milky Way at an extremely large velocity, even exceeding the Galactic[1] escape speed. The abnormal kinematic behavior compared to objects in its current environment and the fact that stars of its type usually are not found far outside of the Galactic disk lead to the assumption that HD 271791 was strongly forced to leave its place of birth as a so-called runaway star and eventually migrated to its present position. Before the finding of HD 271791 the only mechanism thought to be capable to produce motions unbound to the Galaxy was the interaction with a supermassive black hole, the only known being located at the center of the Milky Way. However, studies of the kinematics of the star excluded this possibility. Based on precise abundance analysis of the elements in the atmosphere of HD 271791, Przybilla et al. (2008) found an extreme supernova scenario to be the solution of the problem: HD 271791 is assumed to have been the secondary star in a binary system whose very massive primary component has ended its life in a huge explosion resulting from the collapse of its core, denoted as supernova or even hypernova. On the one hand the event has disrupted the formerly bound system releasing the secondary component approximately with its high orbital velocity. On the other hand it polluted the atmosphere of HD 271791 with material characteristic of such an explosion.

It is the purpose of this work to carry out a profound spectroscopic and kinematic analysis of the star HIP 60350, a runaway candidate sharing many properties with HD 271791, in order to reveal the origins of this peculiar stellar body. Interest in runaway stars is based on the hope to infer observational constraints on supernova events, binary and stellar evolution as well as on the Galactic gravitational potential helping to improve theoretical models on these subjects.

[1] Note that the term **G**alaxy in contrast to **g**alaxy is used synonymic to Milky Way.

2 Astrophysical Background

This chapter, based on the textbooks of Clayton, Carroll & Ostlie and Karttunen et al., is intended to give the necessary astrophysical background needed to understand the diploma thesis especially for those readers not familiar with that field of physics. The most important topics are classification, structure and evolution of stars putting special emphasis on B-type stars, nucleosynthesis, the structure of the Milky Way and runaway stars. Several technical terms are introduced, too.

2.1 Flux, Luminosity, Effective Temperature and Magnitudes

Examination of distant stars is solely based on their emitted light because no further information is obtainable. Proper definitions of physical quantities describing the features of electromagnetic radiation are therefore advisable.

First of all, the *specific intensity* I_ν is defined to be the energy $\mathrm{d}E_\nu$ per frequency interval $\mathrm{d}\nu$ that passes in time $\mathrm{d}t$ through an area $\mathrm{d}A_\mathrm{n}$ in direction of solid angle $\mathrm{d}\Omega$. The subscript n in $\mathrm{d}A_\mathrm{n}$ indicates that the normal to the area is meant to be parallel to the direction of the solid angle $\mathrm{d}\Omega$. With θ being the angle between normal and $\mathrm{d}\Omega$ one has $\mathrm{d}A_\mathrm{n} = \mathrm{d}A\cos(\theta)$ implying:

$$\mathrm{d}E_\nu = I_\nu \mathrm{d}A_\mathrm{n}\mathrm{d}\nu\mathrm{d}\Omega\mathrm{d}t = I_\nu \cos(\theta)\,\mathrm{d}A\mathrm{d}\nu\mathrm{d}\Omega\mathrm{d}t \tag{2.1}$$

The *total intensity* I is obtained by integrating I_ν over all frequencies:

$$I = \int_0^\infty I_\nu \mathrm{d}\nu \tag{2.2}$$

In practice, I is of little interest due to a lack of spatial resolution (except for the Sun). Summing the geometrically weighted intensity over all possible directions yields the net amount of energy flowing through an area $\mathrm{d}A$ per time interval $\mathrm{d}t$, an observable quantity called *flux* F:

$$F_\nu = \int_{4\pi} I_\nu \cos(\theta)\,\mathrm{d}\Omega \qquad F = \int_0^\infty F_\nu \mathrm{d}\nu = \int_{4\pi} I\cos(\theta)\,\mathrm{d}\Omega \qquad \mathrm{d}E = F\mathrm{d}A\mathrm{d}t \tag{2.3}$$

In astronomy, the energy radiated by a star per unit time is denoted as *luminosity* L. There is a simple relation between the flux f that is measured on Earth and luminosity provided no energy is absorbed between emission and detection and the former being constant in time: In this case energy conservation demands the flux integrated over a sphere with its center at the source to be identical to the power radiated by the star, that is, to the luminosity. Choosing the radius to be the distance d to the star and assuming isotropic radiation, i.e., the flux on the sphere being equal for all points, one has:

$$L = \int_{\text{Sphere}} f\mathrm{d}S = f\int_{\text{Sphere}} \mathrm{d}S = 4\pi d^2 f \tag{2.4}$$

Luminosity determination therefore requires knowledge of the distance d, one of the greatest challenges in astronomy since antiquity.

Assigning a temperature T to a star is a nontrivial task. One reason for this is that the surface of a star is not sharp but an extended atmosphere with a nontrivial temperature structure. The other is that the

definition of temperature by statistical physics is in principle only valid in thermodynamic equilibrium. Since stellar objects are close to but never completely in thermodynamic statistical equilibrium, the temperature gained for a star will depend on the physical quantity consulted for its determination. One way of getting a temperature relies on the Stefan-Boltzmann law stating that the total energy emitted per unit surface area of a blackbody in unit time is σT^4, whereby σ is the Stefan-Boltzmann constant. Applying this law to the surface of a spherical, symmetric star defines the *effective temperature* T_{eff} by means of the luminosity and the radius $R_\star$ of the star:

$$L = \int_{\text{Surface}} \sigma T_{\text{eff}}^4 \mathrm{d}S = \sigma T_{\text{eff}}^4 \int_{\text{Surface}} \mathrm{d}S = 4\pi R_\star^2 \sigma T_{\text{eff}}^4 \tag{2.5}$$

Apart from the Sun, however, stellar radii are hardly accessible by observation. Consequently Eq. 2.5 is not helpful to find stellar temperatures. Instead it is used to estimate the radius $R_\star$ from T_{eff} which has to be derived by other means. For instance, T_{eff} can be a parameter in calculations of model atmospheres that has to be varied until computed results match the observation. Another definition of temperature is given by the *color temperature* T_{c}, having the advantage of being independent of $R_\star$: It is chosen such that when inserted in Planck's function for the continuous spectrum of a blackbody this function yields the best fit to the measured specific flux f_ν. The term color refers to the fact that the fitting is usually done in limited wavelength intervals $[\lambda_1, \lambda_2]$ representing specific colors. Many other possibilities to assign stellar temperatures exist, e.g., the *excitation temperature* T_{exc} or *ionization temperature* T_{ion} making use of the population numbers of excited respectively ionized atoms, but will not be discussed here. Suffice to say that in thermodynamic equilibrium all temperatures are the same. In practice, they have to be calibrated with respect to the effective temperature by model atmospheres.

Bearing in mind that the human eye has a nearly logarithmic subjective response to radiant energy flux, it is evidently comfortable to replace the flux f by a logarithmic quantity when talking about the brightness of a visible object. Due to historic reasons this quantity, called *apparent magnitude* m, has the following definition:

$$m = -2.5 \log\left(\frac{f}{f_0}\right) \tag{2.6}$$

Hereby log is the common logarithm to basis 10. f_0 corresponds to the historically set zero point of the magnitude scale and depends on the chosen magnitude system. The definition is made such that brighter stars have lower (even negative) magnitudes and that a difference of five in m results in a factor of hundred in f.[1] The various magnitude systems applied in practice differ essentially in the choice of the flux f: For example, instead of the total flux f one can use the flux around wavelength $\lambda_{\text{V}} = 5400\,\text{Å}$ for the *visual magnitude* m_{V} or simply V whereas the *blue magnitude* m_{b}/B or the *ultraviolet magnitude* m_{u}/U are based on light around $\lambda_{\text{b}} = 4200\,\text{Å}$ and $\lambda_{\text{u}} = 3600\,\text{Å}$, respectively. According to Eq. 2.4 the flux F changes with distance d to the source and due to Eq. 2.6 so does m. To get rid of this dependence, an *absolute magnitude* M is introduced by inserting that flux in Eq. 2.6 that would be measured at a particular, fixed distance to the star, namely $10\,\text{pc}$ [2]. Substituting $d = 10\,\text{pc}$ in Eq. 2.4, solving for F and eventually plugging in the result in Eq. 2.6 gives:

$$M = -2.5 \log\left(\frac{L}{L_0}\right) \tag{2.7}$$

The factor $4\pi\,(10\,\text{pc})^2$ was absorbed into the constant L_0. Hence absolute magnitude M and luminosity L are principally the same.

[1] The naked, night adapted eye can recognize objects with $m \leq 6$.
[2] See Table A.1 for the numerical value.

2.2 Classification of Stars

Almost all the information that can be derived about stars stem from their spectra, i.e., the distribution of electromagnetic radiation with wavelength. Any classification scheme of stars will therefore be based on striking features in those spectra, for instance the strength of peculiar emission or absorption lines. The most common scheme is the Harvard classification, developed at Harvard observatory in the early 20th century. It is based on absorption lines mainly sensitive to the stellar temperature instead of gravity or luminosity. Among others, these lines come from hydrogen, neutral helium, iron, neutral calcium, ionized calcium doublet and some other metals[1]. According to the Harvard scheme, most stars can be divided into one of the seven groups labeled by the capital letters O, B, A, F, G, K, M, recently expanded by L and T, classifying the newly discovered coolest stars and brown dwarfs. As so often in astronomy, the notation has historic reasons. A further subdivision is made by adding the numbers 0...9 to the letters, e.g., B 0 or A 9. The effective stellar temperature decreases from O to M and from 0 to 9. The main characteristics of the spectral types are (see also Fig. 2.1):

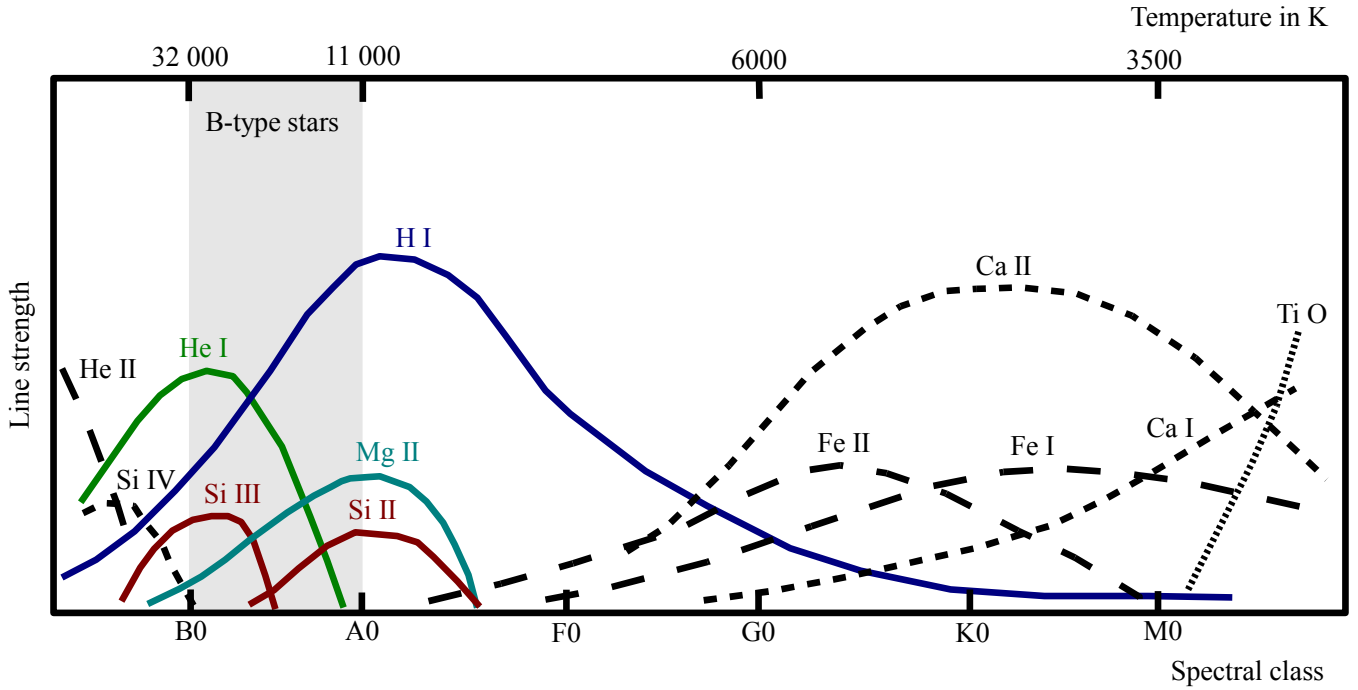

Figure 2.1: Spectral classification of stars via the strength of temperature dependent lines: B-type stars are characterized by strong He I and H I lines and visible lines of, e.g., O I, O II, Si II, Si III and Mg II (based on a figure in Karttunen et al. 1994).

Class O: Surface temperatures of 32 000 K and higher. Ionized helium is prominent, which is merely the case for such high temperatures due to its large first ionization energy. Other atoms in high degrees of ionization are observed, e.g., C III, N III, O III and Si IV[2]. H I lines are weak.
Class B: 32 000 to 11 000 K. He II lines have disappeared. He I lines get stronger for higher-numbered subdivisions, culminate between B 2 and B 5 and vanish at B 9. The Balmer lines of hydrogen increase throughout this group. O I, O II, Si II, Si III and Mg II lines visible.
Class A: 11 000 to 7500 K. Balmer lines strongest around type A 0, then getting weaker, but nevertheless dominating the whole class. He I and O II not visible any more. Slightly ionized metals strengthen and neutral metals begin to appear.

[1] Note that in astrophysics the term "metal" is used to refer to any element other than hydrogen or helium.
[2] The notation X I stands for the neutral element X, X II for the singly ionized atom, X III for the doubly ionized atom and so on.

Class F: 7500 to 6000 K. Ca II doublet as well as metallic lines such as Fe I, Fe II or Cr II getting stronger whereas H I lines weaken.
Class G: 6000 to 5000 K. Ca II doublet very strong. Neutral metals become important. First molecular transitions appear. Balmer lines continue to shrink. The Sun is a star of class G 2.
Class K: 5000 to 3500 K. H I and ionized metals are insignificant. Molecular bands and neutral metals dominate.
Class M: 3500 to 2200 K. Appearance of many complex molecular oxide bands, TiO bands being the most prominent.
Class L: 2200 to 1400 K. Strong lines of Li I, Na I and K I, CrH bands visible, lack of TiO bands.
Class T: $\leq$ 1400 K. Appearance of methane, emission peaks in the infrared.

Most stars can be assigned to one of these spectral classes. In order to categorize even more stellar objects, additional groups have been established, for instance classes S and C which parallel M in temperature but differ remarkably in spectral lines. Class WR contains extremely high-temperature, stellar wind-dominated objects, called Wolf-Rayet stars, with bright, broad emission lines of ionized helium and highly ionized carbon, oxygen and nitrogen. Subclasses, characterized by strong carbon and rather weak nitrogen lines or vice versa, are denoted by WC and WN, respectively. A typical feature of Wolf-Rayet stars are radiation driven stellar winds.

The overall tendency from helium over hydrogen, ionized metals, neutral metals to molecules to be visible is a consequence of their excitation and ionization energies. For example in class O the hydrogen Balmer lines are weak since the high temperature ionizes a large fraction of hydrogen atoms such that the Balmer transitions can no longer be excited. With decreasing temperature, the fraction of neutral hydrogen being in the first excited state grows, finally reaching a maximum value corresponding to apparent Balmer lines in the spectra around type A 0. However, a further reduction of temperature lowers this fraction therefore reducing the visibility again. The position of this peak value naturally depends on the particular excitation and ionization energies of the atom or molecule, respectively, hence resulting in the behavior outlined above. A quantitative description can be made by the combined application of the Boltzmann (Eq. 3.17) and Saha (Eq. 3.18) formulas, the former linking the occupation numbers of excited states within an atom of fixed ionization stage and the latter establishing a connection between different ionization stages by taking into account the available phase space of the released electron.

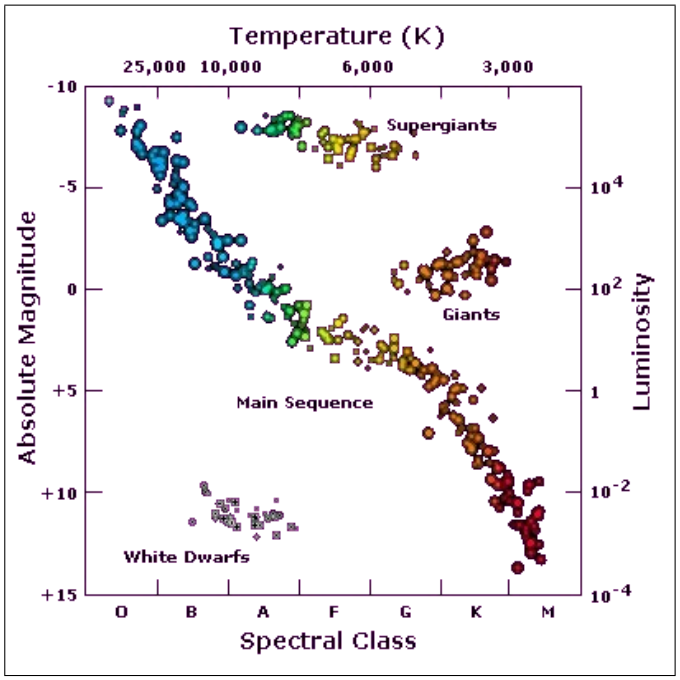

Figure 2.2: Simplified Hertzsprung-Russell diagram revealing fundamental correlations between observable stellar properties. The luminosity is given in terms of the solar luminosity (see Table A.1). The diagram is taken slightly modified from http://sci.esa.int/science-e-media/img/be/hr_diagram.jpg.

To gain further insight into the nature of stars and their evolution it is worthwhile to study the correlation between spectral class/temperature and absolute magnitude/luminosity. This was done at the beginning of the 20th century by the astronomers E. Hertzsprung and H. N. Russell, who empirically found one of the most fundamental relations of astrophysics: plotting the spectral class versus luminosity for a sufficient large number of stars, a clear pattern emerges, implying immediately that some profound principles governing stellar genesis and evolution must lie behind. An example of such a so-called Hertzsprung-Russell (HR)

diagram is shown in Fig. 2.2. One can see that the stellar population can be divided into different groups, namely, *main sequence*, white dwarfs, giants and supergiants. However, these are only the most important ones and there exist many more which are left out for the sake of clarity. Each of those groups represents a phase in the evolution of stars. The main sequence mainly comprises stars that burn hydrogen in their interiors as source of energy, an early step in stellar evolution and by far the longest lasting and important one. Hence approximately 80 to 90 percent of all observed stars lie on the main sequence. The Sun, having a temperature around 5800 K and an absolute magnitude near 4.7 mag, is situated about in the middle of it being a natural border between upper and lower part. In general, the main sequence is followed by the giant or supergiant phase, characterized by more advanced burning stages in the stellar core after exhaustion of hydrogen. Their huge luminosities are consequence of an extremely increased radius compared to that of the main sequence, caused by rearrangement of the stellar structure after the depletion of central hydrogen. The inevitable destiny of most stars is to become a white dwarf: a very compact and hence less luminous, high density object. As no energy is created in their interiors any longer, they are slowly cooling down, avoiding gravitational collapse due to electron degeneracy pressure. Yet, for stellar masses above a certain threshold – the Chandrasekhar limit – the gravitational force is so strong that it can compress the matter to such high densities that the electrons are forced into the nuclei of atoms forming neutrons out of protons. The resulting object is called a neutron star owing its stability to the neutron degeneracy pressure. For masses exceeding the larger Tolman-Oppenheimer-Volkoff limit, even the neutron pressure cannot stop the gravitational collapse any longer, leading to objects so dense and gravitationally strong that no light can escape from them: black holes.

Moreover, the HR diagram of Fig. 2.2 contains information about the masses $M_\star$ of main-sequence stars. Determining stellar masses is a difficult task since its influence on spectra is established merely via the *surface gravity* g, evidently sensitive to the generally unknown[1] radius $R_\star$, too. Nevertheless, some stellar masses can be deduced from binary systems making use of Kepler's third law, provided distance and period are observable. Otherwise one has to rely on numerical calculations of stellar evolution, so-called evolution tracks, where $M_\star$ is the parameter of foremost importance that can be varied in order to fit model to observation. Interestingly, those main-sequence stars enabling one to infer L and $M_\star$ reveal a striking relationship between luminosity and mass:

$$L \propto M_\star^\zeta \tag{2.8}$$

Eq. 2.8 is called *mass-luminosity relation* whereby ζ is 2.5 for $M_\star$ less than half solar mass $M_\odot$ (see Table A.1) and $\zeta = 3$ for $M_\star > 3M_\odot$. Note that this empirical law is roughly valid solely for main-sequence stars being strongly violated by white dwarfs or giants. Together with Fig. 2.2 this implies that main-sequence stars of type O and B belong to the most massive stellar objects. As being explained in the next but one section, they are also the most short-lived ones.

2.3 Stellar Structure

To get a feeling of how stellar evolution tracks are calculated, it is necessary to understand the principle laws describing the structure of stars. For the scope of this work, it is sufficient to do this for the simplest possible case, i.e., to neglect complications like rotation, magnetic fields, gravitational collapse or mass loss. The conditions inside a spherical symmetric star can then be expressed by the following system of four differential equations linking the distribution of mass, pressure, energy production and energy transport to

[1] As discussed in Sect. 2.1, $R_\star$ can be derived from $T_{\rm eff}$ and L. However, L requires knowledge of the distance d to the star which is usually not at hand. Instead the mass obtained by other means delivers via g and hence $R_\star$ the distance d (see Sect. 5.1).

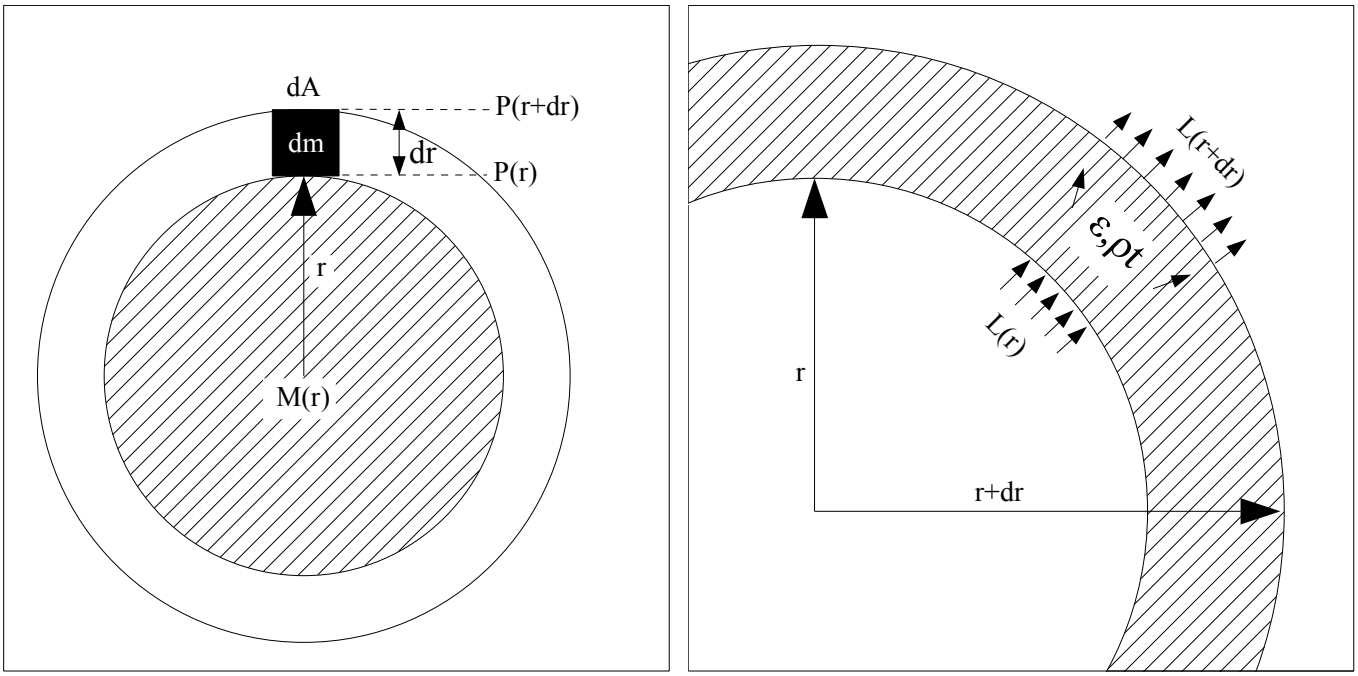

a: Hydrostatic equilibrium b: Conservation of energy

Figure 2.3: A static stellar structure demands the ingoing gravitational force F_g to be compensated by a pressure induced outgoing force F_P yielding the equation of hydrostatic equilibrium. Energy conservation states that the difference in luminosities of two close shells is caused either by nuclear reactions or changes in the heat energy between the shells.

each other:

$$\frac{\mathrm{d}M_\star(r)}{\mathrm{d}r} = 4\pi r^2 \rho(r) \tag{2.9a}$$

$$\frac{\mathrm{d}P(r)}{\mathrm{d}r} = -\frac{GM_\star(r)\rho(r)}{r^2} \tag{2.9b}$$

$$\frac{\mathrm{d}L(r)}{\mathrm{d}r} = 4\pi r^2 \rho(r) \left(\varepsilon - T\frac{\mathrm{d}S}{\mathrm{d}t}\right) \tag{2.9c}$$

$$\frac{\mathrm{d}T(r)}{\mathrm{d}r} = -\frac{3}{4ac}\frac{\alpha\rho(r)}{T^3}\frac{L(r)}{4\pi r^2} \qquad \text{or} \qquad \frac{\mathrm{d}T(r)}{\mathrm{d}r} = \frac{\Gamma_2 - 1}{\Gamma_2}\frac{T(r)}{P(r)}\frac{\mathrm{d}P(r)}{\mathrm{d}r} \tag{2.9d}$$

Eq. 2.9a is called *mass continuity equation* and is just another way to express the well known fact that for a spherical symmetric distribution of matter $M_\star(r) = \int_0^r 4\pi r'^2 \rho(r')\mathrm{d}r'$. Eq. 2.9b follows from application of Newton's second law to an infinitesimal mass element $\mathrm{d}m$. Denoting the radial position of this mass element by r_ρ and the pressure by P one has according to Newton and Fig. 2.3a:

$$\begin{aligned}
\mathrm{d}F &= \mathrm{d}m\frac{\mathrm{d}^2 r_\rho}{\mathrm{d}t^2} = \rho(r)\mathrm{d}A\mathrm{d}r\frac{\mathrm{d}^2 r_\rho}{\mathrm{d}t^2} \\
\mathrm{d}F &= \mathrm{d}F_\mathrm{g} + \mathrm{d}F_\mathrm{P} = -\frac{GM_\star(r)\mathrm{d}m}{r^2} + P(r)\mathrm{d}A - P\left(r+\mathrm{d}r\right)\mathrm{d}A = -\frac{GM_\star(r)\rho(r)\mathrm{d}A\mathrm{d}r}{r^2} - \mathrm{d}P(r)\mathrm{d}A \\
\Rightarrow\ & \frac{\mathrm{d}P(r)}{\mathrm{d}r} = -\frac{GM_\star(r)\rho(r)}{r^2} - \rho(r)\frac{\mathrm{d}^2 r_\rho}{\mathrm{d}t^2}
\end{aligned}$$

In equilibrium, the time derivative vanishes and the *equation of hydrostatic equilibrium* 2.9b is obtained. Eq. 2.9c ensures energy conservation. Hereby $\varepsilon = \varepsilon\left(\rho(r), T(r), \{X_Z\}\right)$ is the power liberated per unit mass of stellar matter by nuclear reactions. It is obviously a function of density $\rho(r)$, temperature $T(r)$ and of the set of elemental abundances $\{X_Z\}$, X_Z denoting the fraction by weight of element with atomic number Z[1].

[1]It is convention to use X and Y instead of X_1 and X_2 for the hydrogen respectively helium fraction.

With $S = S(\rho(r), T(r), \{X_Z\})$ being the entropy per unit mass of stellar matter, the second term reflects the fact that energy can be absorbed or released in form of heat $\mathrm{d}Q = T\mathrm{d}S$, too. From the definition of those quantities in combination with Fig. 2.3b one has $4\pi r^2\rho(r)\mathrm{d}r\varepsilon = L(r+\mathrm{d}r) - L(r) + 4\pi r^2\rho(r)\mathrm{d}rT\frac{\mathrm{d}S}{\mathrm{d}t}$ leading immediately to Eq. 2.9c.

Eq. 2.9d determines the temperature gradient within the star which is deeply connected to the way of how energy is transported in it. In principle, there are four possibilities: radiative transfer, convection, conduction and neutrino emission. Due to their weak interaction with matter, neutrinos merely remove energy from the star instead of rearranging it. Hence neutrino losses can be regarded as a negative ε in Eq. 2.9c and do not influence the temperature gradient. Calculations show that the effects of conduction are non-negligible solely for extremely high densities as encountered in, e.g., white dwarfs and are therefore not of interest for this work. For common main-sequence stars, energy transport is established either by radiative transport or convection. To decide which, consider a certain amount of gas enclosed in a perfectly elastic balloon that is displaced adiabatically, i.e., without exchange of heat, by a small distance in radial direction. Due to the negative pressure gradient (see Eq. 2.9b) inside the star, the balloon will expand to adopt the same pressure as its environment. Since the expansion is assumed to be adiabatic, the new density inside the balloon will in general differ from that outside of it. If the inner density exceeds the outer, the balloon will be drawn back by gravitation leading to a stable, non-convective configuration. According to the equation of state of a perfect gas, a higher density implies a lower temperature at constant pressure and consequently a larger change of T inside the balloon since temperature decreases with radius. Hence one can conclude that convection can solely take place if the radiative temperature gradient exceeds the adiabatic one given by the second formula in Eq. 2.9d, where $\Gamma_2 = \Gamma_2(\rho(r), T(r), \{X_Z\}) > 1$ is the second adiabatic exponent connecting T and P during adiabatic changes to each other. It can be computed from the density, temperature and composition of the gas. As already mentioned, the other mechanism of energy transport is radiation. According to the Stefan-Boltzmann law, the power emitted per unit area by a blackbody is σT^4. Consider two adjacent spherical shells of radius $r - \mathrm{d}r$, r and temperature $T - \mathrm{d}T$, T. Under the assumption that each shell absorbs all energy irradiated on it, the net energy gain at r per time is equal to the luminosity: $L(r) = 4\pi r^2\sigma((T-\mathrm{d}T)^4 - T^4) = -16\pi r^2\sigma T^3\mathrm{d}T + \mathcal{O}(\mathrm{d}T^2) \approx -16\pi r^2\sigma T^3\mathrm{d}T$. Further assuming that each photon travels a characteristic distance l before absorption, $\mathrm{d}T$ becomes $\frac{\mathrm{d}T}{\mathrm{d}r}l$. For later convenience, define the *mass absorption coefficient* α by $l = (\rho\alpha)^{-1}$ and introduce the radiation constant $a = 4\sigma\, c^{-1}$ with c being the speed of light in vacuum. Putting everything together yields $L(r) \approx -16\pi r^2 \frac{ca}{4}\frac{T^3}{\alpha\rho}\frac{\mathrm{d}T}{\mathrm{d}r}$. Apart from a factor $\frac{4}{3}$ this is identical to the first formula in Eq. 2.9d gained by solving the diffusion equation and a precise definition of the mass absorption coefficient $\alpha = \alpha(\rho(r), T(r), \{X_Z\})$ (see Clayton, 1983, pp. 172-183). In order to decide which formula of Eq. 2.9d has to be applied, one has to calculate both expressions: As shown above, as long as the radiative temperature gradient lies below the adiabatic one, the first formula has to be chosen. In all other cases convection occurs which is assumed to be adiabatic and therefore the second formula can be used.

A few words about α and its related quantity *opacity* $\kappa = \alpha\rho$, respectively, are appropriate at this point. As indicated by its name, the opacity is a measure for the ability of photons to transit through a medium: the higher κ the shorter the mean distance passed before absorption or scattering takes place and vice versa. Its four main contributions are bound-bound, bound-free and free-free absorption plus scattering off free electrons. The first three interactions are true absorption processes in the sense that the number of photons is decreased by one. They share the property that a photon is absorbed by an electron enhancing the energy of the latter. However, depending on the state – bound to an atom or free in the continuum – of initial and final electron the description of the interaction varies significantly. Scattering off free electrons or Compton scattering is not a true absorption process inasmuch as the photon number does not change. Yet, this interaction alters the kinematics of photons and can be thought of absorption of initial and subsequent emission of final photon hence also influencing the opacity of stellar matter. These interactions, especially bound-bound and bound-free absorption, evidently depend on the composition of the medium under investigation.

Temperature and density affect the state of the atoms as well as the number and distribution of electrons therefore being crucial for determination of κ, too[1]. Obtaining opacities is a complicated task as it requires the knowledge of various cross-sections most of them being calculated by means of atomic physics. Moreover, the composition and state of the matter has to be taken into consideration and finally, for application in Eq. 2.9d, a nontrivial average over frequencies has to be applied, the so-called *Rosseland mean* (see Clayton, 1983, p. 182). Being by far the most abundant elements within a star, hydrogen and by parts helium dominate κ. Computations reveal that hydrogen ionization zones, i.e., regions where a considerable part of hydrogen starts to get ionized and characterized by $T \approx 10^4\,\mathrm{K}$ for densities of main-sequence stars, have the largest opacities. This behavior is intuitively evident because lower temperatures neither provide enough photons with the necessary energy to induce bound-free transitions nor is the number of free electrons high enough for scattering to be important. On the contrary, larger temperatures reduce the fraction of atoms being in low excited states hence mitigating the effects of bound-bound and bound-free absorption on the opacity. For intermediate temperatures none of the four absorption processes substantially drops off resulting in a maximum value for κ. Apart from a higher temperature the same argumentation applies for helium ionization zones. This has meaningful consequences for the existence of surface convection zones. According to Eq. 2.9d the radiative temperature gradient is proportional to κ implying the steepest gradients and correspondingly possible convection to lie exactly at those ionization zones. What is more, Γ_2 happens to be closest to unity in a partially ionized state further enhancing this effect. However, as illustrated in Fig. 2.2, the effective surface temperature of O- and B-type stars exceeds $10^4\,\mathrm{K}$ so that there actually is no hydrogen ionization region within these stars leading to a lack of surface convection. But as the surface temperatures of stellar objects following B-stars in the Harvard classification are below this value one might expect surface convection in that case. In this reasoning, helium ionization zones are neglected as their opacities are in general not high enough to cause convection.

Having defined the system of differential equations 2.9 governing the structure of the simplest possible star, it is now to solve it for a given set of boundary conditions: $M_\star(0) = 0$, $L(0) = 0$, $P(R_\star) = P_{R_\star}$ and $T(R_\star) = T_{R_\star}$, whereby $P_{R_\star} = T_{R_\star} = 0$ is assumed[2]. Here the radius $R_\star$ of the star is an input parameter. Further having expressions for $\varepsilon\left(\rho(r), T(r), \{X_Z\}\right)$, $S\left(\rho(r), T(r), \{X_Z\}\right)$, $\alpha\left(\rho(r), T(r), \{X_Z\}\right)$, $\Gamma_2\left(\rho(r), T(r), \{X_Z\}\right)$ and making use of the equation of state of the stellar gas $P = P\left(\rho(r), T(r), \{X_Z\}\right)$ to eliminate the pressure, the system is completely determined and numerical integration methods yield the mass, temperature, density and luminosity as functions of the radius r provided the composition $\{X_Z\}$ of the star is given. In order to have the total stellar mass as input parameter and $R_\star$ as a result of the calculation, one can introduce $M_r = M_\star(r)$ instead of r as the independent variable by inverting Eq. 2.9a and using it to rewrite the other equations. The resulting functions are $r(M_r)$, $L(M_r)$, $T(M_r)$ and $\rho(M_r)$ with M_r ranging from zero to total mass $M_\star$. Once an initial stellar model is at hand, it can be used to compute evolution tracks of stars. What one has to do is to specify the new input parameters of the time evolved model by means of the old model, e.g., taking into account composition changes due to nuclear reactions and convection and updating the time derivative of the entropy S.

Although the numerical problem is extremely complex, the success of such stellar models is impressive. Apart from the model for the sun being successfully tested with neutrinos and helioseismology, the mass-luminosity relation of the preceding section can be confirmed, and what is more, stellar evolution – as outlined in the following section – can be reproduced.

[1] The occupation numbers of atomic states, ionization levels and the velocity distribution of electrons are sensitive to T whereas high densities can shift atomic energy levels and change the degree of ionization.

[2] At least for stars having no surface convection zone such as O- and B-type objects since in that case it can be shown (see Clayton, 1983, p. 440) that the interior structure is insensitive to the boundary conditions. Note that $T_{R_\star} = 0$ does not imply $T_{\mathrm{eff}} = 0$ as the latter is achieved via $L(R_\star)$, $R_\star$ and Eq. 2.5.

2.4 Stellar Evolution

A very important tool to understand the time evolution of stars is the well-known *virial theorem* from statistical physics linking the total kinetic energy K to the total gravitational potential Φ, provided the system is in hydrostatic equilibrium:

$$K = -\frac{\Phi}{2} \tag{2.10}$$

The most crucial statement that can be drawn from Eq. 2.10 is the fact that gravitational contraction, i.e., further lowering the negative Φ, from one stable state to another one leads to a rise in kinetic energy of half of the released gravitational potential associated with an increment in temperature T: a contracted mass is heated up. The remaining part of the liberated energy is transformed into radiation.

Star formation is induced by gravitational instabilities of the interstellar gas. If a sufficient amount of matter is somehow compressed to a small enough volume, gravitation can overcome the counteracting pressure prompting the gas to collapse and increasing both gravitational as well as pressure forces. Due to heat-up processes at the center of the instability in the gaseous cloud the internal pressure eventually stops the shrinkage resulting in a state close to hydrostatic equilibrium in the central region. However, mass is still accreted from the surrounding medium further enhancing temperature and pressure. This continues until the central temperature reaches the point where repulsive Coulomb interactions between hydrogen nuclei are overcome at adequately large rates so that a non-negligible amount of nuclear fusion reactions occur in the core. The additional release of energy raises the radiation pressure preventing the newly formed star from gaining even more mass and after some time to balance, an almost perfectly stable state is achieved. Since enormous masses – a lower limit is given by the Jeans mass – are needed to cause the interstellar gas to collapse, stars cannot be formed alone but in large groups of up to a few thousands members, so-called *open clusters*. The various stars in a cluster come from fragmentation of the initial cloud into smaller ones, being compact enough to go on contracting on their own.

The first nuclear burning stage creating energy in a permanently stable star is the conversion of hydrogen to helium, commonly denoted as hydrogen burning. As hydrogen is by far the most abundant element, there is so much fuel that stars will spend the main part of their lifetimes in this phase of stellar evolution, fittingly labeled main sequence. The burning of hydrogen does not occur in a single reaction but in two independent reaction networks, called proton-proton (PP) chain and CNO bi-cycle. Their contribution to the energy generation depends on the environmental temperature, the former dominating for smaller T and hence lower main-sequence objects like the Sun whereas the latter for upper main-sequence stars, in particular of type O and B. Figures 2.4 and 2.5 give an overview of what happens in these two mechanisms.

Investigations reveal (see Clayton, 1983, pp. 366-410) that the energy generation rate in the CNO bi-cycle is extremely sensitive to temperature when compared to the PP chains. This has far-reaching consequences on the stellar structure: Stars obtaining the largest part of their radiated energy by the CNO bi-cycle have steep temperature gradients in the vicinity of the center as T is maximal there and consequently the energy generation is strongly peaked. Therefore almost the entire stellar luminosity is created in a tiny central region, the core. In order to transport those overwhelming amounts of energy to outer layers, a gradient in temperature exceeding the adiabatic one is necessary inevitably leading to central convection zones. This is not the case for PP chains dominating nuclear reactions in the stellar core, as their T-dependence is comparatively modest. Together with the results about the existence of surface convection zones of Sect. 2.3 one can conclude that objects in the upper main sequence like B-type stars have convective cores but radiative surfaces, whereas the situation is just the other way round for lower main-sequence stars like the Sun.

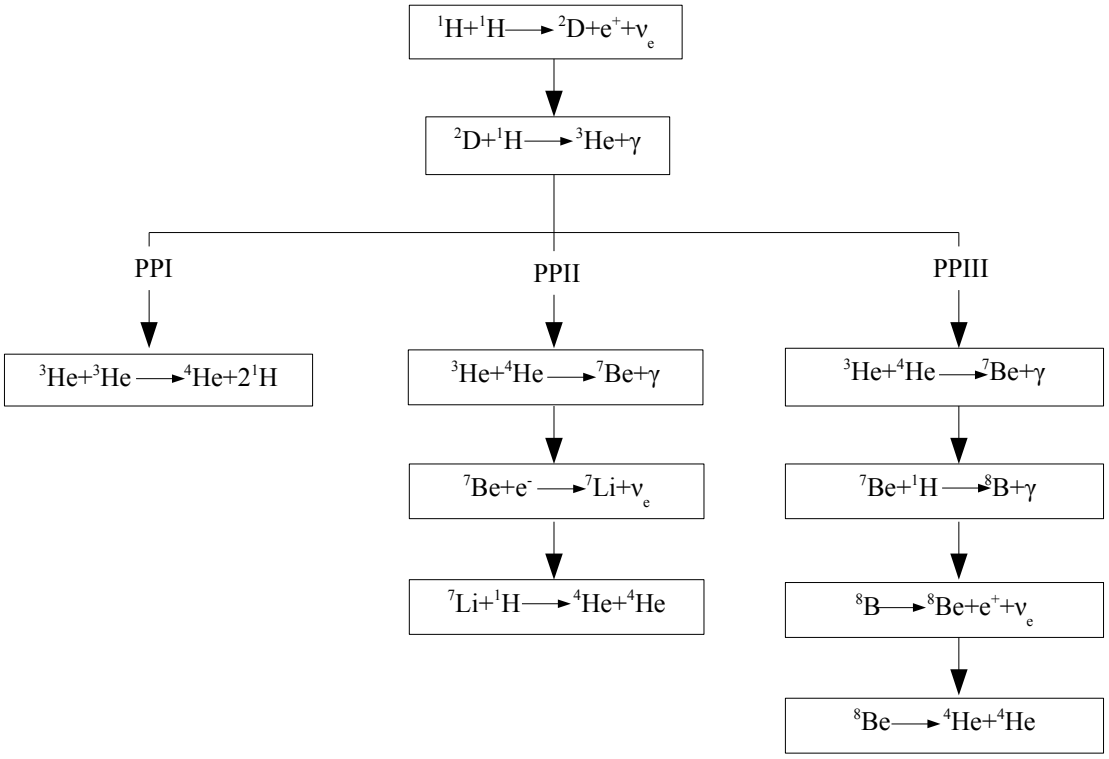

Figure 2.4: Reactions in the proton-proton (PP) chain of hydrogen burning: Three different reaction channels can be distinguished: PPI, PPII and PPIII. PPI is the only path that can occur in a pure hydrogen gas and is most effective for lowest temperatures. With increasing central T PPII, then PPIII and finally the CNO bi-cycle dominate the energy generation.

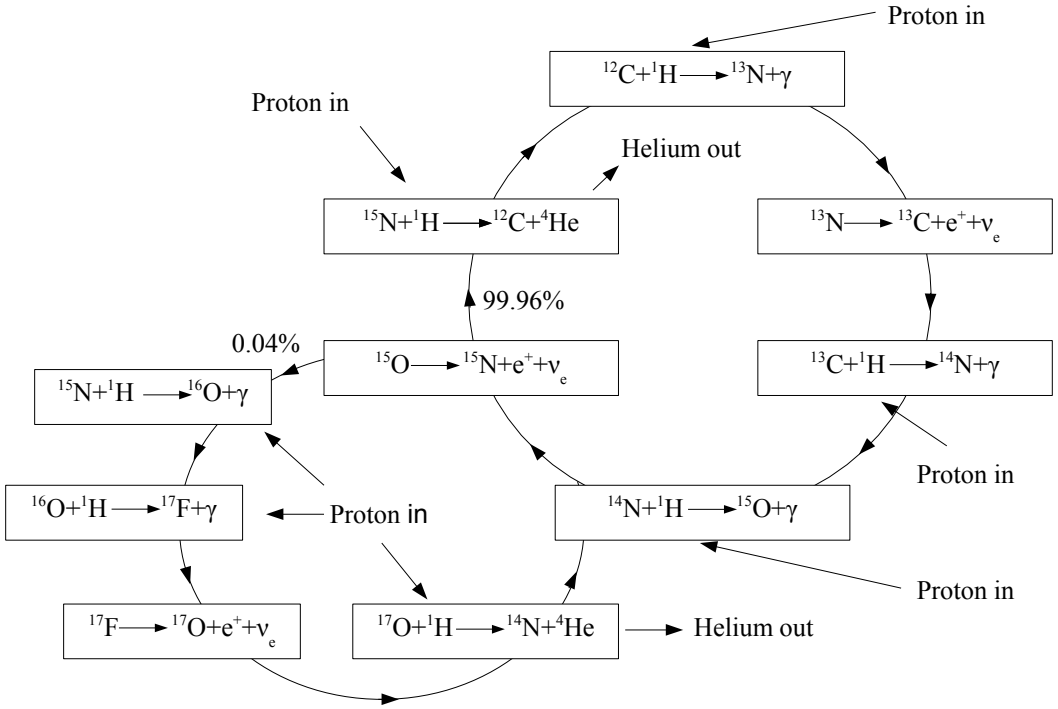

Figure 2.5: Reactions in the carbon-nitrogen-oxygen (CNO) bi-cycle of hydrogen burning: As illustrated C, N and O act as catalysts in the bi-cycle implying that at least one already has to be present at the star's formation time.

Another difference is given by the lifetimes of stars. As indicated by Eq. 2.8 and Fig. 2.2 the masses of upper main-sequence stars exceed that of the lower ones. Naively one could therefore assume that they live longer due to their greater supply of fuel. In reality the opposite is true. This can be seen again from Eq. 2.8: The luminosity is proportional to a rather high power of $M_\star$ demanding lots of additional energy to be produced from massive stars hence driving them to consume unburned material faster than their low-mass counterparts. From numerical evolution tracks or observations, respectively, stellar lifetimes can be deduced ranging from some billion years for the lower end of the main sequence down to several million years for extraordinarily massive O-type stars.

During hydrogen burning, the location of the star in the HR diagram is shifted somewhat to the upper right from its original position characterized by the ignition of hydrogen[1]. The reasons for this shift are structural rearrangements induced by composition changes caused by conversion of hydrogen to helium. One of those structural changes comes from the reduction of free particles due to fusion and associated drop of particle pressure leading to slow but steady contraction of the core. The resulting rise of central temperature on the one hand steepens the temperature gradient forcing the outer layers of the star to expand in order to reduce the gradient again such that energy balance is reestablished. On the other hand the temperature of the shell enclosing the core is also lifted to values capable of burning hydrogen leading to a further contraction of the central region. The development described so far is similar for stars of all masses and happens gradually, contrary to what follows when central hydrogen is exhausted. In a vastly simplified picture, the depletion of hydrogen leaves behind a non-reactive and therefore rapidly contracting helium core surrounded by a hydrogen burning shell. The central contraction is still accompanied by an expansion of the whole star, preluding its giant phase in the HR diagram.

In massive stellar objects ($M_\star > 8$–$10\,M_\odot$) the quick shrinkage is halted awhile by the ignition of helium burning via the *triple alpha reaction*[2] $3\,{}^4\mathrm{He} \rightarrow {}^{12}\mathrm{C} + \gamma$. Apart from a much shorter time span the evolution during central helium burning is quite analogous to that of hydrogen burning, meaning that there remains again a non-reactive, rapidly contracting core enclosed by an inner helium and outer hydrogen burning shell after loss of central helium fuel. Nevertheless, the composition of the core is not solely restricted to carbon: Due to alpha particle captures, e.g., oxygen, neon and magnesium are produced to some extent, too. With enhancing temperatures, the formerly Coulomb suppressed carbon and oxygen burning stages start creating mainly magnesium $\left({}^{12}\mathrm{C} + {}^{12}\mathrm{C} \rightarrow {}^{24}\mathrm{Mg} + \gamma\right)$, sulfur $\left({}^{16}\mathrm{O} + {}^{16}\mathrm{O} \rightarrow {}^{32}\mathrm{S} + \gamma\right)$ and silicon $\left({}^{16}\mathrm{O} + {}^{16}\mathrm{O} \rightarrow {}^{28}\mathrm{Si} + {}^{4}\mathrm{He}\right)$ subsequently followed by silicon burning comprehensively expressed by ${}^{28}\mathrm{Si} + {}^{28}\mathrm{Si} \rightarrow {}^{56}\mathrm{Ni} + \gamma$. Finally nickel decays to iron ${}^{56}\mathrm{Ni} \rightarrow {}^{56}\mathrm{Co} + \mathrm{e}^+ + \nu_\mathrm{e} \rightarrow {}^{56}\mathrm{Fe} + 2\mathrm{e}^+ + 2\nu_\mathrm{e}$ having the largest binding energies per nucleon of all elements. Further thermonuclear fusion reactions would require energy instead of releasing it, marking the natural end of energy generation due to nuclear fusion.

At this point in stellar evolution the massive star is supposed to have an onion-like structure as illustrated in Fig. 2.6: The originally centered hydrogen burning region has moved out because of exhaustion of fuel in the inner part and rise of temperature in outer layers enabling hydrogen to fuse there. The product of hydrogen burning, helium, and all the following burning phases have undergone the same development. However, at the onset of carbon and oxygen burning T is large enough for another effect to occur: *photodisintegration*, i.e., the disintegration of nuclei by the thermal photon bath. Since those fission reactions are endothermic, they reduce temperature and pressure of their environment. Being negligible for carbon and oxygen fusion, they play a decisive role in silicon burning (see Clayton, 1983, pp. 517-533) and especially for the final fate of massive stars: As mentioned above, iron is not capable to produce further energy by nuclear reactions. Instead the collapse of the already contracting iron core is tremendously accelerated by the removal of photons due to the photodisintegration of iron reducing temperature, particle as well as radiative pressure resulting in a runaway process. In this way, the gravitational energy gain converts back a considerable amount of iron to elements prior in the fusion chain. The almost free fall of the core raises the density to values sufficient to force free electrons to be captured by protons forming neutrons. The core contraction is then finally halted or at least sharply slowed down by the emerging degenerate neutron pressure being a consequence of

[1] The curve consisting of those points is referred to as ***z**ero **a**ge **m**ain **s**equence* (ZAMS).

[2] Actually it is ${}^4\mathrm{He} + {}^4\mathrm{He} \leftrightarrows {}^8\mathrm{Be}$ with ${}^8\mathrm{Be}$ being so unstable that an almost instantaneous catch of a third alpha particle ${}^8\mathrm{Be} + {}^4\mathrm{He} \rightarrow {}^{12}\mathrm{C} + \gamma$ is necessary for the triple alpha reaction to take place.

Pauli's exclusion principle for fermions. The abrupt deceleration leads to some rebound of matter sending away pressure waves into the outer, in-falling material. Although loosing significant amounts of energy via photodisintegration induced by the temperature increment after compression, the shock waves can leave the iron rich central region. In exterior shells they regain strength by igniting higher or by fostering existing nuclear burning stages, respectively, or by absorption of an adequate rate of neutrinos copiously released by, e.g., photodisintegration, electron-positron annihilation or neutron production via electron capture of a proton. The latter is possible since the densities in the waves reach values so high that not even so weakly interacting particles like neutrinos can penetrate without some absorption. The strengthening of the shock waves finally leads to an eruptive explosion during which the outer regions of the star are expelled. According to Fig. 2.6 the ejected envelope mainly consists of hydrogen, helium, carbon and the so-called *alpha elements* oxygen, neon, magnesium, silicon and sulfur. Depending on the mass of the remnant object it can either evolve to a neutron star in the case that neutron degenerate pressure can cope with the gravitational force or as a black hole if it cannot.

The events just outlined describe a *Type II supernova*, differing from Type I due to the existence of hydrogen absorption lines. Supernovae of Type I lack this peculiar feature and can further be distinguished into I a, I b and I c: The latter two resemble Type II supernovae as they also originate from the collapse of a massive star's iron core. Albeit, stars of Type I b must somehow have lost their hydrogen shell, Type I c even their helium envelope prior to the supernova explosion. Type I a supernova are believed to be produced by mass accretion of carbon-oxygen white dwarfs, e.g., in close binary systems. Accounting for mass loss during the stellar evolution, white dwarfs are the final fate of lower main-sequence stars with $M_\star < 8\,M_\odot$: In contrast to massive stars the central conditions prevent the star from igniting carbon or oxygen burning after helium depletion in the core. The reason for this are the huge densities of central carbon and oxygen resulting in an additional electron degeneracy pressure that halts the core contraction and associated T increment which would be essential for further nuclear fusion reactions. After getting rid of its outer layers forming a planetary nebula, the extremely compact and thus luminous, remaining core is slowly cooling down as a white dwarf. However, if by some means the mass of the compact object is lifted above a critical threshold, carbon burning via a mechanism denoted as *carbon flash* can begin after all: The release of nuclear energy increases the temperature, but by virtue of the matter's degeneracy does not significantly effect the pressure. Hence there will be no expansion counteracting the vastly growing T leading to ever more fusion reactions until the degeneracy is removed. Like a thermonuclear run-away, the front of carbon burning moves fast outwards liberating more and more energy eventually disrupting the entire star. In contrast to other supernovae, explosions of Type I a set free a considerable amount of iron fused during the sudden and enormous jump of temperature and leave no remnant behind.

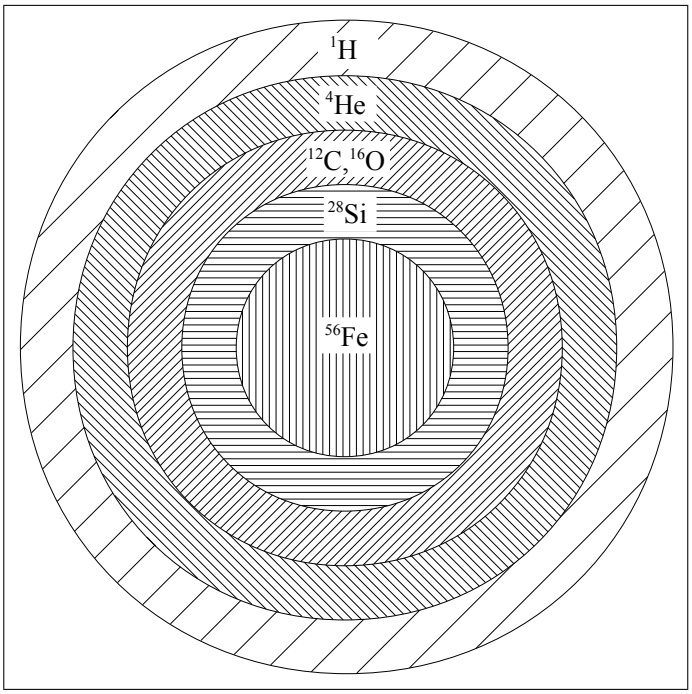

Figure 2.6: Onion-like shell structure of massive stars at the end of their evolution: Each shell represents a nuclear burning stage originally located at the center and after depletion of fuel displaced to heated up outer layers (The drawing is not to scale).

As just mentioned, the destiny of low-mass stars like the Sun is to become a white dwarf after main-sequence hydrogen and giant-phase helium burning. The boundary separating the evolution of massive from non-massive objects is not sharp and depends on the composition of the star, especially on its *metallicity*, i.e., abundances of elements other than hydrogen and helium. A possible end for intermediate stars ($8\,M_\odot < M_\star < 10\,M_\odot$) is a supernova-like explosion initiated by ignition of degenerate matter consisting of carbon or oxygen resulting in carbon or oxygen flashes.

Having some insights in the complicated issue of stellar evolution[1] one is now able to deal with the problem of stellar nucleosynthesis.

2.5 Origin of the Elements

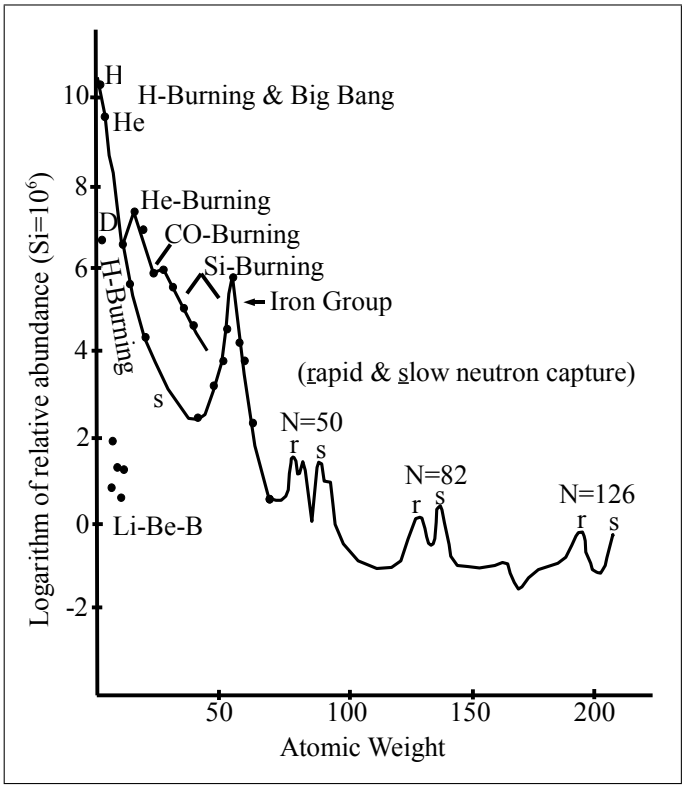

Figure 2.7: Schematic abundance curve for the solar system and similar main-sequence stars (taken slightly modified from Fowler, 1984): Abundances are given relative to Si = 10^6, i.e., number of particles per 10^6 silicon atoms. The particular shape of the graph can be explained well by principles of nuclear physics under conditions encountered in stars during their evolution.

The complex theory of elemental synthesis in stars has been developed for more than fifty years[2] now and is still far from being complete. For the scope of this work only the basic ideas are of importance and hence presented. Figure 2.7 illustrates schematically the elemental abundances as they are found in the solar system and similar main-sequence stars. Apart from an overall decline in number with larger atomic weights, striking peaks are evident being a direct consequence of the nuclear structure of atoms and the circumstances encountered during the evolution of stars. As indicated in Fig. 2.7, primordial hydrogen and helium, with the latter also mainly produced in the early phase of the universe right after the Big Bang, are most abundant. All heavier chemical elements have been produced from them by nuclear reactions in the interiors of stars, some of them already outlined in the previous section, and subsequently have been ejected into interstellar matter, e.g., by supernova explosions to form new generations of stellar objects. Because of this fact, the metallicity increases with time since ever more stars undergo the final stages of their evolution.

As mentioned in the foregoing section, the last nuclear burning stage capable to liberate significant amounts of energy is silicon burning which is accompanied by the counteracting process of photodisintegration. It is due to the existence of those non-negligible inverse disintegration reactions that a state of nuclear statistical equilibrium can be achieved after exhaust of silicon, obviously favoring those elements that have the tightest binding and hence the lowest energies – the iron-group elements. This principle, commonly denoted as *e(quilibrium)-process*, yields a good explanation for the iron peak in Fig. 2.7.

But what is the origin of those elements more massive than the iron group? The mechanisms described so far – e-process and nuclear fusion – have shown to underestimate their abundances vastly. The reasons for this are too small binding energies per nucleon respectively too high Coulomb repulsion forces that prevent those

[1] For much more detailed information the reader is referred, e.g., to Karttunen et al. (1994, Chap. 12) or Carroll & Ostlie (1996, Chap. 13).

[2] Starting with Burbidge et al. (1957) and Cameron (1957). A very comprising review article is given for instance by Wallerstein et al. (1997).

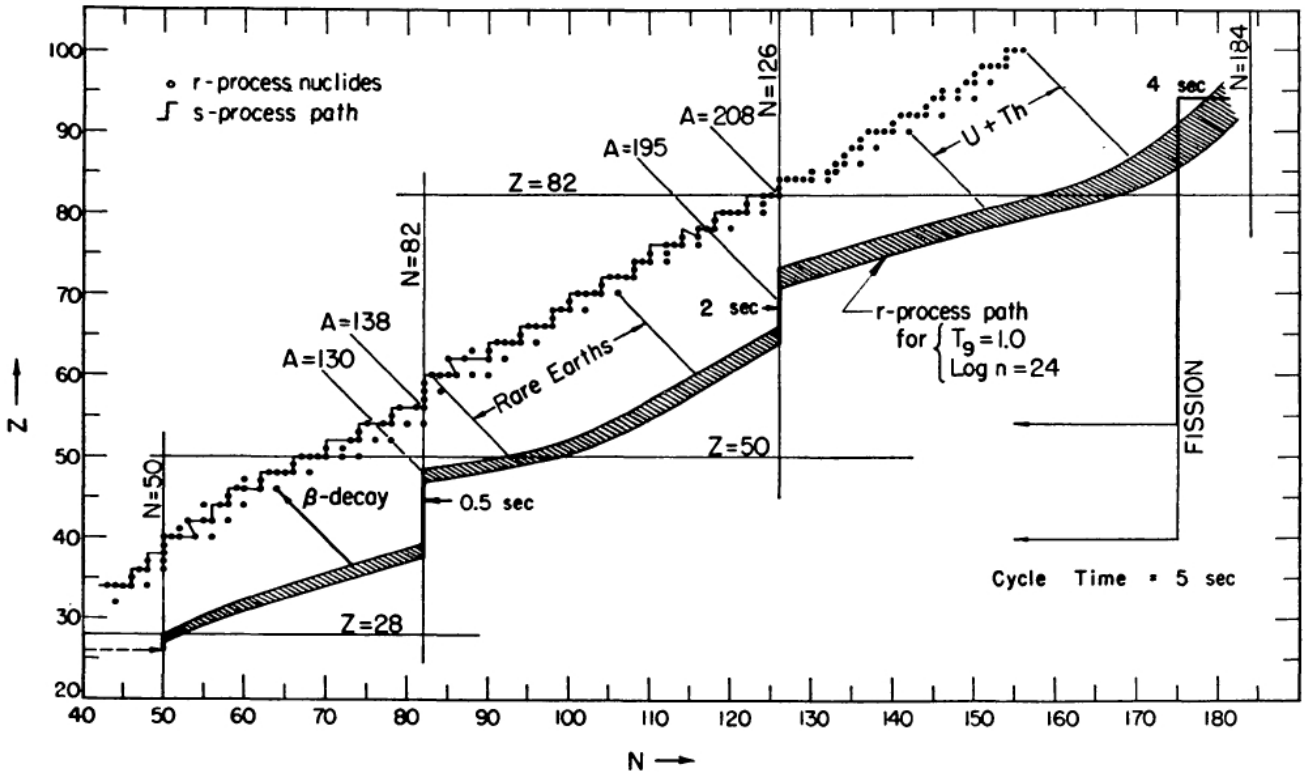

Figure 2.8: Neutron capture paths for the s- and r-process (adopted from Seeger, Fowler & Clayton, 1965): N denotes the neutron number, Z the proton number. The r-process path is calculated for a temperature $T = 10^9\,\mathrm{K}$ and a neutron density of $n = 10^{24}\,\mathrm{cm}^{-3}$. The decisive role of the "magic" neutron numbers $N = 50, 82, 126$ corresponding to closed neutron shells in the nuclear shell model for the abundance peaks in Fig. 2.7 is evident.

events from occurring at significant rates. These obstacles are avoided when considering neutron captures which are not affected by the Coulomb interaction. Hence, adding successively one neutron after the other can build up massive, neutron-rich atoms that are transformed into different chemical elements by β-decays. Depending on the available neutron flux, two kinds of neutron capture processes can be distinguished:

In the *s(low)-process* the neutron flux is so small that any β-decay has time to occur before the next neutron is captured. The resulting path in the neutron-proton plane is shown in Fig. 2.8. In order to explain the abundance peaks labeled with s in Fig. 2.7 one has to bear in mind that the neutron capture cross sections in the s-process path are not equal. In particular, a shell model of the nucleus[1] shows that atoms with neutron numbers $N = 50, 82, 126$ have comparatively tiny cross sections due to closed neutron shells implying a low probability and correspondingly a long time to catch further neutrons and hence lead to the observed accumulation in abundance. The neutron fluxes necessary for the s-process are obtained during hydrogen and helium shell burning since under such conditions protons, carried from hydrogen to helium shells, e.g., by convection, can initiate the following reaction chain: $^{12}\mathrm{C}+\mathrm{p} \rightarrow {}^{13}\mathrm{N}+\gamma \rightarrow {}^{13}\mathrm{C}+\mathrm{e}^+ + \nu_\mathrm{e} + \gamma$ and $^{13}\mathrm{C}+{}^4\mathrm{He} \rightarrow {}^{16}\mathrm{O}+\mathrm{n}$. Alternatively, neutrons can be produced in hotter environments via $^{14}\mathrm{N}+{}^4\mathrm{He} \rightarrow {}^{18}\mathrm{F}+\gamma$, $^{18}\mathrm{F} \rightarrow {}^{18}\mathrm{O} + \mathrm{e}^+ + \nu_\mathrm{e}$, $^{18}\mathrm{O} + {}^4\mathrm{He} \rightarrow {}^{22}\mathrm{Ne} + \gamma$ and $^{22}\mathrm{Ne} + {}^4\mathrm{He} \rightarrow {}^{25}\mathrm{Mg} + \mathrm{n}$.

The *r(apid)-process* is characterized by a neutron flux so large that there is no time for β-decays to happen in between two successive neutron capture events. Therefore atoms will acquire evermore neutrons, which

[1] Despite its conceptual simplicity the model has been so successful that its inventors were awarded with the Nobel Prize in physics 1963. For more details see the Nobel lecture of Goeppert Mayer (1964).

according to the shell model are less and less bound. This process is finally stopped when the photo-ejection rate of the least bound neutrons equals the neutron-capture rate. However, this kind of steady state is destroyed as soon as the neutron-rich atom β-decays, resulting in a new nuclear structure with tighter binding so that thermal photons are not able to remove neutrons any longer. In case of closed neutron shells with $N = 50, 82, 126$, an additionally added neutron generally has a very low binding energy compared to the one before. Consequently several β-decays are needed before the capture of neutrons can continue. Since waiting for β-decays takes the most part of the whole process, atoms will pile up at when having $N = 50, 82, 126$. The rapid capture is stopped when the neutron flux expires. Then, the neutron-rich atoms undergo subsequent β-decays until the first stable configuration is reached. According to Fig. 2.8 the resulting abundance maxima lie at smaller mass numbers A than their s-process equivalents just as empirically found, see Fig. 2.7. In contrast to the s-process a definite location with a sufficient neutron flux required for the r-process is not yet found. The most promising site is close to a neutron star forming in a supernova explosion with neutrons being liberated by weak interaction of matter with neutrinos. Unfortunately, observational evidence for this assumption is missing[1].

One may wonder whether neutron fluxes intermediate to the s- and r-process exist whose theoretical description would be much more complex. Luckily, it seems to be a fact that this is not the case and that a combination of the two processes is sufficient to explain the elemental abundances beyond the iron group.

2.6 Structure of the Milky Way

The Milky Way is a normal spiral galaxy that, as illustrated in Fig. 2.9a, can be divided into the three major parts central bulge, disk and halo:

Central bulge: The center of the Milky Way hosts a supermassive black hole ($\sim 10^6\, M_\odot$) that is surrounded by a spherical central bulge. The latter contains primarily relative old stars with ages of a couple of billion years while young (ages of a few million years), massive and luminous stars can be observed, e.g., in the Quintuplet and Arches clusters in the most central, complex region. Mass density and metal content are comparatively high. Sharing features of both, halo and disk, makes it a distinct Galactic component.
Disk: The Galactic bulge is enclosed by a rotating, dichotomous disk with a thick component being approximately 30 kpc in diameter and 2 kpc in height. The thin disk (height $\sim$ 100–200 pc) comprises a considerable fraction of the youngest and metal-rich stars in the Milky Way with ages of million years. Almost solely in its spiral arms there is enough dense interstellar matter for star formation to happen. Those young stars usually, but not solely belong to *open clusters* or *associations*, i.e., groups of up to a few hundred stars, much stronger gravitationally bound to each other than to nonmembers, missing any inherent regular structure. In contrast, the surrounding thick disk consists of relatively old, metal-poor stars similar to those of the halo.
Halo: Bulge and disk are embedded in a huge spherical halo with a radius possibly ranging from 50 to 100 kpc. Halo stars can have ages of about thirteen billion years, therefore being generally among the oldest and are typically found in *globular clusters*: stable, gravitationally bound, spherical arrangements of several ten thousand stars showing regular, radial structure. Due to the lack of dense interstellar material, star formation is really rare in the halo explaining the low metallicities as well as the huge ages of its constituents. Since the visible stellar mass in the halo is by far insufficient to account for the shape of the observed Galactic rotation curve, the halo is supposed to be dominated by dark matter.

In order to distinguish stellar objects according to their kinematics, age and chemical composition the concept of stellar populations is used. However, one should note before that in contrast to what comes next the sequence of populations actually is not discrete nor strict but rather continuous. Nevertheless the following crude classification has proven to be helpful:

[1] See for instance Wallerstein et al. (1995).

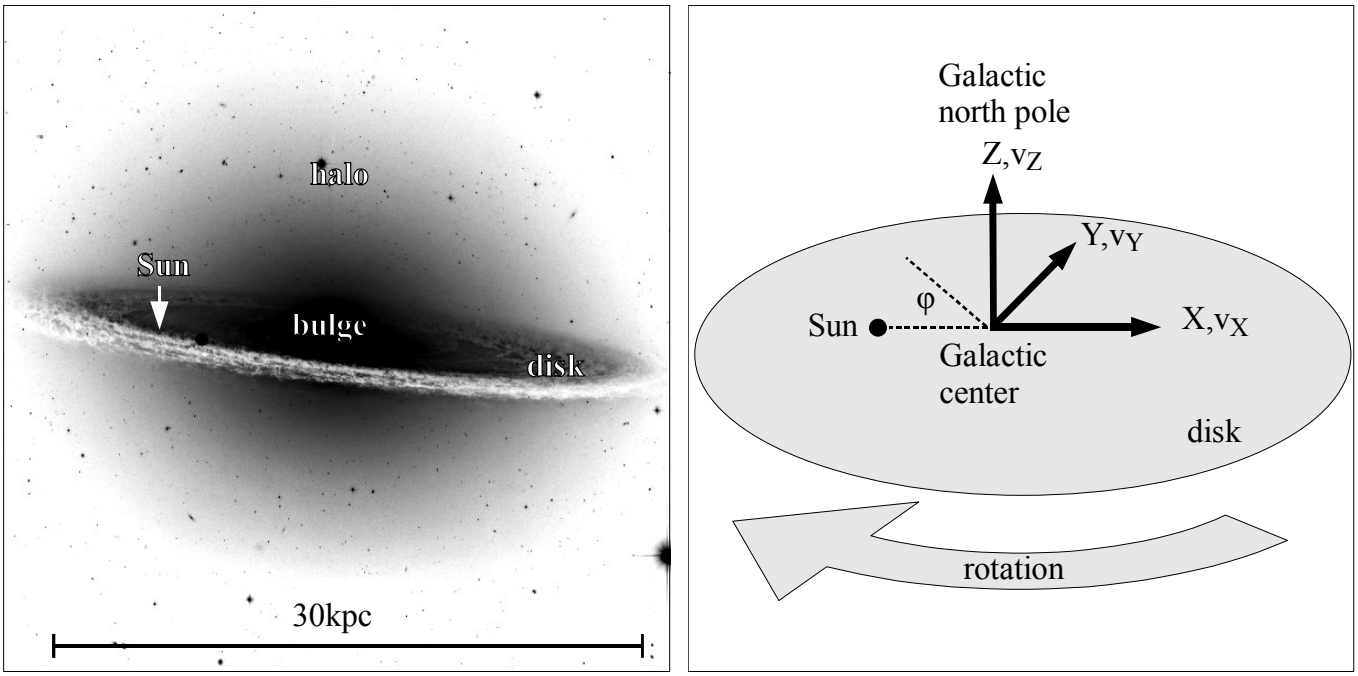

a: Schematic structure

b: Galactocentric coordinate system

Figure 2.9: Schematic structure of the Milky Way showing its three major components: central bulge, disk and halo. Galactocentric coordinate system as used in this work: a right-handed, non-rotating frame of reference with the Galactic center at the origin, Galactic north pole in Z-direction and the Sun's current position at $X = -8\,\mathrm{kpc}$, $Y = 0$ and $Z \approx 0 \pm 20\,\mathrm{pc}$. Due to disk rotation the coordinates of the Sun are not constant.

Population I: Stars with ages up to a few billion years, high metal fraction by weight of 0.01 to 0.04, almost circular orbit around the Galactic center, very low velocity component parallel to the disk's normal, often found in open clusters and hence in the thin disk, includes the Sun.
Population II: Old (more than 10 billion years), metal poor (< 0.01) objects on elliptical trajectories not aligned to the Galactic plane, largest vertical velocity components, usually found in globular clusters of the halo.

To study and describe the kinematics of stellar bodies, the choice of a proper coordinate system is indispensable. In this work a right-handed, non-rotating frame of reference with the Galactic center at the origin, Galactic north pole in positive Z-direction and the Sun's current position at $X = -8\,\mathrm{kpc}$ is used and referred to as *Galactocentric*. Note that the planar coordinates X, Y of the Sun will change with time as the disk is rotating[1], the direction being clockwise as seen from the Galactic north pole and illustrated in Fig. 2.9b. Velocity components in X, Y, Z-direction are labeled with v_X, v_Y, v_Z. Sometimes a cylindrical system with $r_{\mathrm{cyl}} = \sqrt{X^2 + Y^2}$ and $\varphi = \arctan(-Y/X)$ is considered, too.

Investigating orbits can be an important tool to gain valuable information about stars. In order to do so, one needs a reliable model of the Milky Way's gravitational potential, e.g., provided by Allen & Santillan (1991). Their potential, being the sum of a spherical central mass distribution simulating the bulge $\Phi_{\mathrm{B}}(R)$, a disk component $\Phi_{\mathrm{D}}(r_{\mathrm{cyl}}, Z)$ and a spherical halo $\Phi_{\mathrm{H}}(R)$ whereby $R = \sqrt{X^2 + Y^2 + Z^2}$, reproduces observed quantities like the Galactic rotation curve or visible mass distribution quite well. Further advantages are its closed analytic form, mathematical simplicity and lack of unphysical expressions such as negative mass densities.

[1]The rotation of the disk is differential and can be described by a Galactic rotation curve giving the orbital speed as a function of the distance to the center and having a value of $220\,\mathrm{km\,s^{-1}}$ at the Sun's position, see e.g. Allen & Santillan (1991).

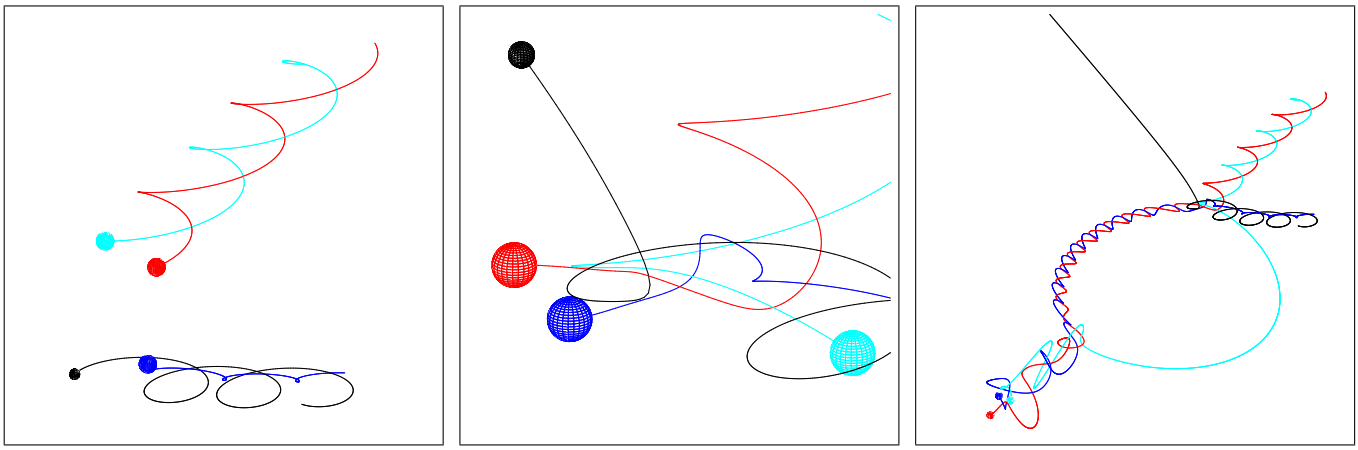

a: Situation before... b: ... during ... c: ... and after encounter

Figure 2.10: Dynamical binary-binary interaction producing a runaway star: Two initially separated binary systems interact via a spatially close encounter forming a triple system and a high-velocity runaway star (black). For details on this figure see Sect. A.3.

2.7 Runaway Stars

From the preceding section it should be clear that stars of type O or B are usually not expected to be observed outside the disk since due to their small lifetimes they are assumed to be found in the vicinity of star-formation regions normally situated in the Galactic plane. Yet, the location of such stellar objects in the halo can have two possible reasons: Firstly, but unlikely, they indeed have formed in the halo, e.g., by the collision of high-velocity H I clouds compressing the interstellar matter enough to cause gravitational collapse (see for instance Huang, Gies & McSwain, 2009). Secondly, they are original disk members prompted by some mechanism to run away from the environments at which they were born becoming so-called *runaway stars*.

Up to now, two viable scenarios describing their creation exist. I) They can be the result of dynamical interaction in star clusters – either initial dynamical relaxation (Poveda, Ruiz & Allen, 1967) or close many-body encounters such as binary-binary interactions in dense, compact and massive star clusters (Leonard & Duncan, 1988) – giving one component enough kinetic energy to escape from the cluster (see Fig. 2.10). A necessary but not sufficient condition for this to be true is that when tracing back the trajectory of the runaway star to the Galactic plane there has to have been a suitable open cluster or association, respectively, adjacent to the intersection point and corresponding in age and chemical composition.

II) According to Blaauw (1961) they can be the secondary component of a binary system whose primary and hence more evolved star explodes as a supernova enabling the other one to escape from the formerly bound system (see Fig. 2.11). In this case one would expect the runaway star to accrete some of the material ejected in the supernova explosion. According to Sect. 2.4 and Fig. 2.6 the most promising candidates are, among others, carbon, oxygen, neon, magnesium, silicon and sulfur. Detecting an overabundance in these chemical elements is a clear hint for the supernova scenario. However, since the pollution of the runaway star's atmosphere with supernova ejecta is small, it is evidently no simple task to observe their tiny traces, demanding high-quality stellar spectra and very good models of atmospheres so that apart from Przybilla et al. (2008) no successful analysis of that kind is known.

Observational hints for both of the suggested scenarios exist: According to Hoogerwerf, de Bruijne & de Zeeuw (2001) the two single stars AE Aur and μ Col together with the binary system ι Ori can be the result of a dynamical ejection event in the Trapezium cluster of the Orion nebula. Gualandris, Portegies

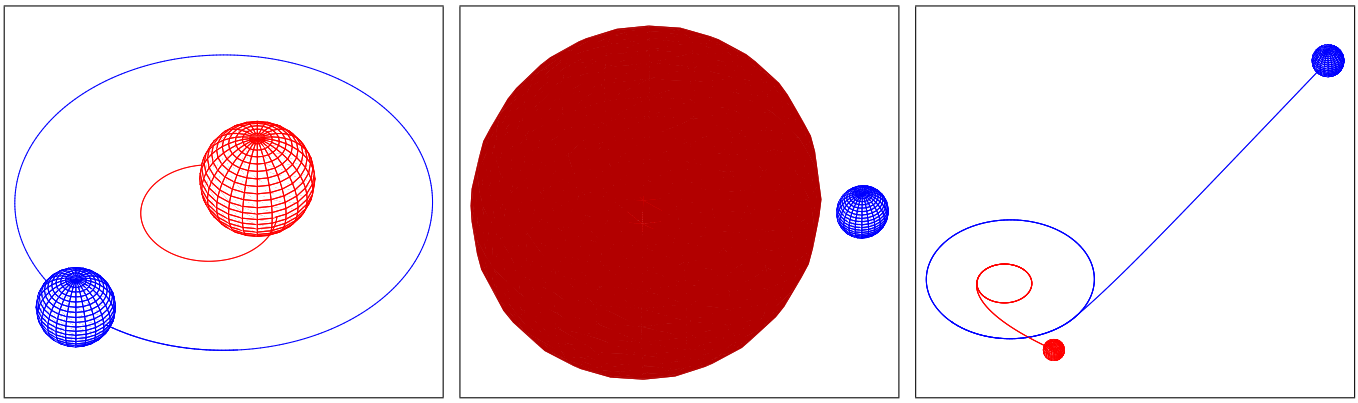

a: Initially bound binary system b: Supernova explosion c: Release of the runaway star

Figure 2.11: Disruption of a binary system by a supernova explosion: The primary component (red) of an initially bound system explodes in a (symmetric) supernova reducing its mass significantly. The secondary star (blue) is hence so weakly attracted by the supernova remnant that it is able to leave the binary as a runaway star. For details on this figure see Sect. A.3.

Zwart & Eggleton (2004) performed numerical calculations of binary-binary interactions to show that such an encounter could indeed account for the observation. What is more, they found conditions for which the initial binaries exchange partners and eject the other two objects. This would solve the enigma of different ages of ι Ori's components. Moreover, Hoogerwerf, de Bruijne & de Zeeuw assign the star ζ Oph and the pulsar PSR J1932+1059 to a common binary system disrupted by the supernova explosion of the pulsar's progenitor. In very few cases a supernova explosion may not disrupt the two bound components. For instance, this can be seen in the system GRO J1655-40 (Israelian et al., 1999) consisting of an F-type star and a black hole. Because of enhancement of α-elements in the former's atmosphere, the latter is supposed to be the result of a supernova. Conditions for not braking up the binary during the explosion might be an insufficient mass loss via the expelled shell or an asymmetry in the ejection event stabilizing the system (Tauris & Takens, 1998). The kick received due to the asymmetric event could even be strong enough to prompt the binary to become a runaway object.

What is usually done in literature to argue for or against one of the two scenarios is to study the kinematics of the runaway star. Since proper models for the gravitational potential of the Milky Way are at hand, it is no problem to calculate back the stellar orbits yielding disk intersection coordinates, ejection velocities v_{ej} and times of flight T_{flight} it takes to arrive at the plane if current velocities of the desired objects are known. Those quantities contain fruitful information: for instance having no appropriate open cluster or association at the intersection point is an argument for the supernova explosion. T_{flight} is an important indicator to figure out whether the star is a runaway star at all: If T_{flight} exceeds the evolution time of the star T_{evo} a runaway scenario from the Galactic plane can be fairly excluded. In case of a binary supernova scenario, the ejection velocity can be linked to the orbital velocity yielding additional constraints a possible progenitor system has to fulfill.

The purpose of this work is to perform a detailed spectroscopic as well as kinematic study of the star HIP 60350 to examine its origin. HIP 60350 is a young stellar body located in the Galactic halo ($X = -8.7\,\mathrm{kpc}$, $Y = -0.5\,\mathrm{kpc}$, $Z = 3.0\,\mathrm{kpc}$) with huge Galactic rest-frame velocity $v_{\mathrm{grf}} = \sqrt{{v_X}^2 + {v_Y}^2 + {v_Z}^2} \approx 530\,\mathrm{km\,s^{-1}}$ indicating a rather spectacular runaway ejection event in the past. Its B-type nature bears many advantages for the intended abundance analysis. First of all B-stars are luminous making it relatively easy to acquire high-quality spectra even if they are far away. Additionally, their youth allows valid information from orbit computation to be gained since the shorter the numerical calculation the smaller the errors caused by uncertainties in initial conditions. As outlined in Sect. 2.3 one does not expect surface convection to occur. This is crucial as otherwise the anyway small concentration of possible supernova ejecta at the surface could

be critically diminished by mixing it with layers lying below the photosphere. Therefore stars of type F to M in the Harvard classification would be less promising candidates although the extent and hence the mass of the convection zone decreases towards F consequently not excluding a successful search. The drawback of A-stars is the diffusion-driven mixing of heavy supernova products, a feature not present in type O and B. This is due to the fact that by means of their numerous line transitions heavy elements are strongly coupled to the radiation field which is growing with effective temperature. The momentum absorbed with the photons is sufficient to prevent those elements from diffusing in deeper layers and keeps them at the surface. This effect is also responsible for stellar winds observed in extremely hot objects such as Wolf-Rayet stars. Contrary to B-type stars, radiation pressure is non-negligible when modeling the atmospheres of O-type stars making it very complicated to analyze their spectra. In addition, the larger the masses the rarer the objects. Accordingly, it is unlikely to find a lot of O stars in general and in particular among the runaway stars as the supernova-ejected component is always the less evolved and hence less massive one. B-type stars are not significantly affected by these problems making them perfect targets when investigating runaway stars.

Due to their eruptive ejection, runaway stars typically have speeds larger than the average yet being – apart from the exceptions HD 271791 and the recently discovered J0136+2425 (Tillich et al., 2009) – far below the local Galactic escape speed. In this sense they are sometimes referred to as high-velocity stars. Consequently there is a close relation to *hyper-velocity stars*, i.e., stellar bodies stemming from the central region of the Milky Way and having velocities larger than the Galactic escape speed, therefore being unbound. They are assumed to be produced by the supermassive black hole in the Galactic center whose tidal forces disrupt a closely passing binary system and accelerate one member to sufficient large velocities (Hills, 1988). Until the discovery of HD 271791 by Heber et al. (2008), already mentioned in the introduction, this was the only known mechanism capable to produce such enormous speeds. Due to HD 271791 there was need to introduce the term *hyper-runaway star* classifying unbound objects not originating from the interaction with the central supermassive black hole.

Investigating runaway stars can bring new insights into several distinct fields of astronomy. Once a sufficient large sample of runaways is analyzed, their distribution in space as well as velocity may be used to constrain the structure and gravitational potential of the Milky Way or the dynamics occurring during many-body interaction and supernova explosions, respectively. They are valuable for gaining information about the frequency of *in situ* star formation in the Galactic halo or even might exclude this possibility at all. Furthermore models of stellar and binary evolution must account for their characteristics. Chemical elemental abundance analyses of supernova runaway stars can give hints about the complex processes such as envelope ejection and nucleosynthesis in those explosions. Detecting enhanced concentrations of r-process elements would be the first observational evidence for the assumption that rapid neutron capture is situated in supernovae. The latter, however, is a very ambitious task and would require high-quality ultra-violet (UV) spectra which are not easy to obtain.

3 Quantitative Spectroscopy

Spectroscopy, i.e., the practice of obtaining and studying the distribution of electromagnetic radiation with wavelength, is one of the most powerful tools in astronomy. It provides access to a wide range of parameters describing the physical state of stellar objects. The development of ever larger telescopes and more accurate spectrographs enables astronomers to take spectra of extremely good quality. Together with highly advanced theoretical models, they allow for quantitative analyses with astonishingly high precision.

The goal of this chapter is to present all details of such an analysis. In order to do so, the necessary theoretical background of radiation transfer and its numerical solution is explained. Atmospheric parameters and their effects on the emitted spectrum are introduced and their determination by comparison with synthetic models is demonstrated. But first of all some practical aspects of spectrum preparation are discussed.

3.1 Data Reduction

The raw data obtained from a spectrograph cannot be used for any quantitative investigation. In order to do so, they have to be processed into a useful form by a procedure called data reduction. Depending on the spectrograph in use, the steps applied during this process vary a little bit. The principal ideas are nevertheless the same for all the existing devices. Hence the conversion from raw to final data can be illustrated by means of a particular device, e.g., an Echelle spectrograph.

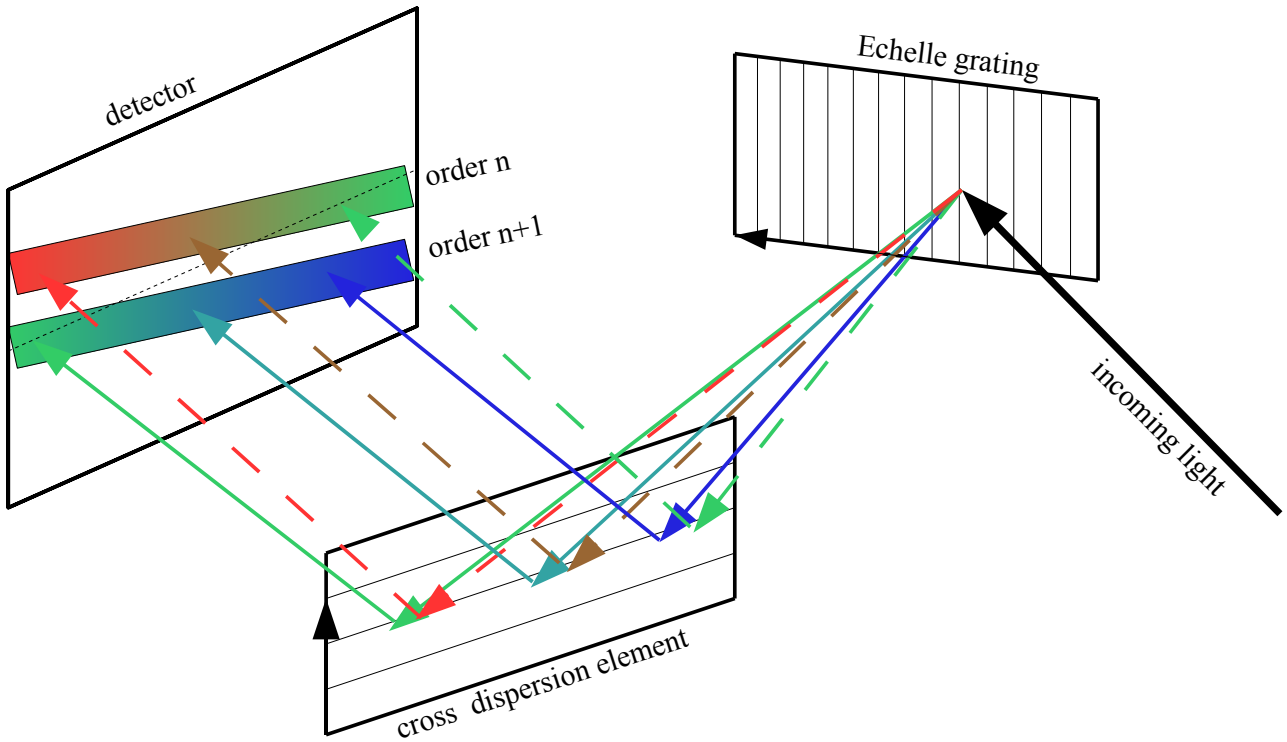

Figure 3.1: Schematic construction of an Echelle spectrograph: Light is diffracted by an Echelle grating creating overlapping orders of diffraction. Each order is covering an almost unique range of the visible spectrum and is finally separated from the others by a second dispersion element perpendicular to the first one.

In contrast to other spectrographs the Echelle spectrograph creates high-resolution spectra on comparatively small CCD chips (Charged coupled devices) and therefore saves space. Basically, it consists of two parts (see Fig. 3.1 for the schematic construction): The first one is an Echelle grating that is normally a blaze grating with a blaze angle around 65° and matching angle of incidence so that the main intensity occurs at very large diffraction orders, say order of 100 for the optical range. Due to these settings, light of slightly different wavelengths is separated over a relatively large angular distance resulting in a very high spectral resolution $\lambda/\Delta\lambda$, whereby $\Delta\lambda$ is the minimum wavelength difference that can be resolved. However, there are two problems: A large angular separation implies need for lengthy CCD chips in order to cover a considerable range of the optical spectrum and, what is more, the different diffraction orders are strongly overlapping. Both are solved by the second component of the Echelle spectrograph: A dispersion element in perpendicular direction, for instance a prism or a low dispersion grating, which separates the overlapping orders into oblique stripes vertically distributed over the detector respectively CCD chip. With a clever choice of parameters (blaze angle, incident angle, groove spacing, ...) it can be achieved that the range of intersection of neighboring orders is small so that each single order covers a unique part of the visible light. Finally combining all orders of diffraction yields a wide range high-resolution spectrum obtained with the help of a common CCD chip. The name of the spectrograph – "echelle" is the French word for ladder or stairs – either originated from the resulting pattern on the detector that resembles a ladder or from the stair-like form of the Echelle grating.

An example of a raw stellar spectrum obtained with the help of an Echelle spectrograph is shown in Fig. 3.2a. Colors are not included as they would just increase the complexity of the detector and bring no benefit. Instead, the wavelength information is given by a Thorium-Argon reference lamp shown in Fig. 3.2b. Knowledge about the wavelengths of the emission lines enables one to precisely assign a wavelength scale to the corresponding spectrum.

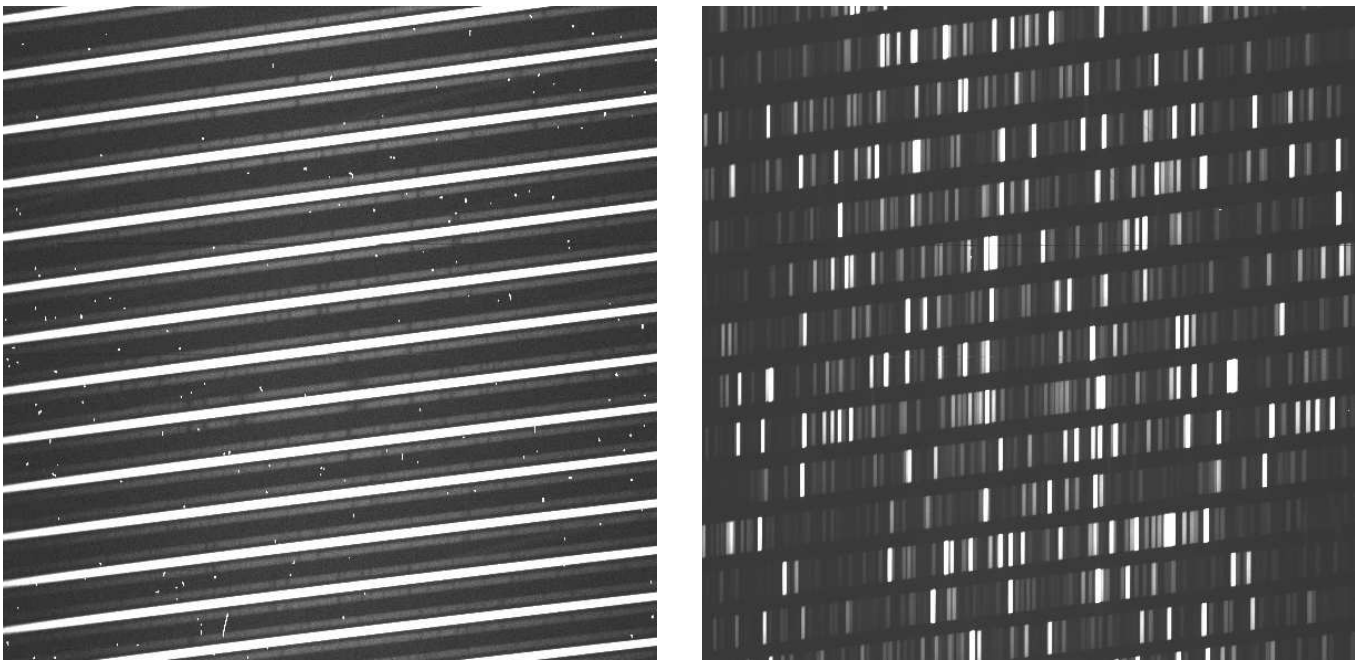

a: Untreated stellar spectrum

b: Thorium-Argon reference spectrum

Figure 3.2: Untreated stellar and Thorium-Argon reference spectrum gained from an Echelle spectrograph: The latter one contains the wavelength information for the first one provided that the setting of recording is equal.

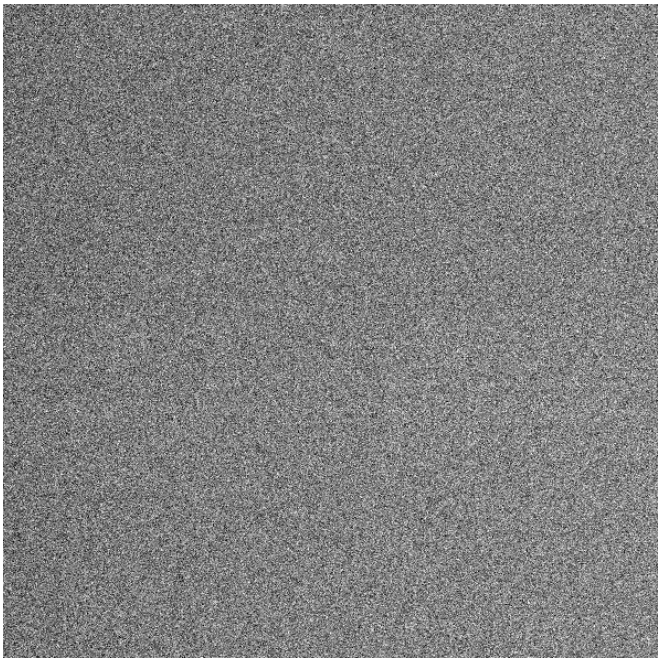

a: Averaged bias frame

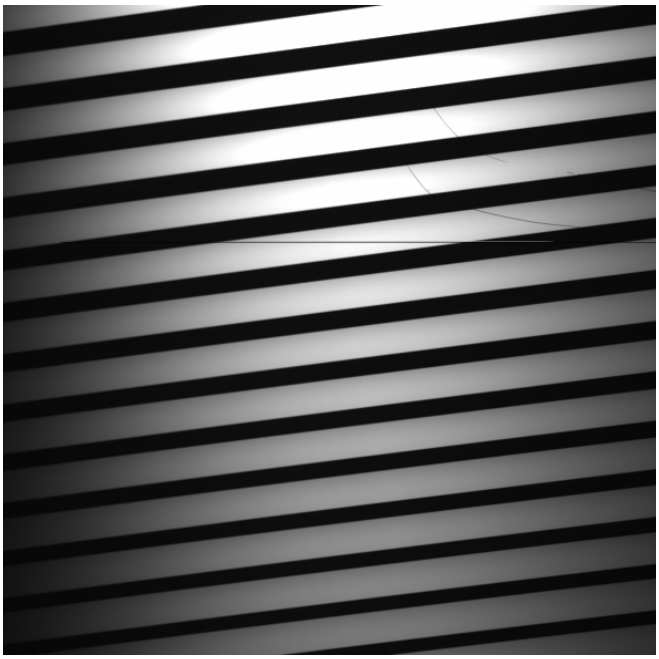

b: Averaged flat-field frame

Figure 3.3: Averaged bias and flat-field frames: The bias frame has to be subtracted from the object frame to correct the readout offset. In addition to that, the latter has to be divided by the flat-field frame to take into consideration spatially varying sensitivities. Note that the contrast is drastically increased in the left panel to account for the smallness of the signal noise.

The raw stellar spectrum of Fig. 3.2a is the starting point for data reduction, consisting mainly of six major steps[1]:

1. **Removal of high-energetic cosmic particles:** A look at the raw spectrum of Fig. 3.2a reveals a number of white dots randomly distributed over the CCD chip. Those events stem from high-energetic cosmic particles that create signals generally much larger than photons do. Furthermore the number of these events naturally rises with increasing exposure time. To remove them, one applies a filter that substitutes values above a certain local threshold by the averaged value of the near vicinity also defining the threshold.

2. **Subtraction of bias:** Due to noise, very weak signals could be shifted to negative values during the readout process of the CCD. To avoid this unwanted effect, a constant offset is automatically added to each image before readout. This artificial signal can be removed by so-called bias frames, i.e., images taken with (almost) zero exposure time and closed shutter. In practice, several bias frames are taken, averaged to reduce noise and finally subtracted from all of the following images. Figure 3.3a shows the average of ten bias frames.

3. **Flat-fielding:** The intensity profile of a star usually is deformed by the spectrograph due to the frequency dependent sensitivity of the latter. Furthermore there might be some damaged pixels on the CCD chip like in the tiny dark horizontal line in the fifth row counting from above of Figs. 3.2a and 3.2b ending in an unwanted drop of the photon flux. In order to account for those effects one images a source that emits light as independent of frequency as possible. The resulting frame is denoted as flat-field and an example is

[1] In the following, data reduction is illustrated by means of an Echelle spectrum taken with the *Hobby-Eberly Telescope* (HET, see Sect. 3.2 for more information). The software used is the *Munich Image Data Analysis System* (MIDAS, `http://www.eso.org/sci/data-processing/software/esomidas//`).

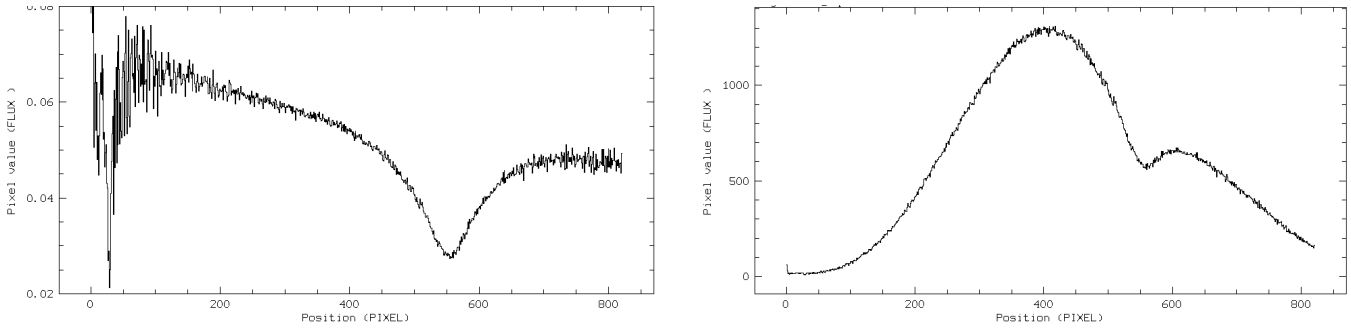

a: Divided by smoothed flat-field

b: Not divided by smoothed flat-field

Figure 3.4: Single-order Echelle spectra obtained via division by normalized two-dimensional flat-field and subsequent summing over opaque lines of a particular stripe. The left image is additionally divided by the smoothed one-dimensional flat-field.

given in Fig. 3.3b. Two major features are striking: Firstly, there are more regions of weakened sensitivity than the horizontal line just mentioned. Secondly, the intensity tends to decrease with increasing row when counted from above. Reasons for the latter are: general loss of intensity for higher orders of diffraction and decreasing sensitivity of the CCD chip in combination with a declining strength of emission of the source towards corresponding wavelengths. To get rid of those influences of measurement one has to divide the object frame by the flat-field frame (corrected for the readout bias), hence replacing the relative strong frequency dependence of the spectrograph by the smooth one of the flat-field source. However, spectra from HET like that of Fig. 3.2a require special treatment[1] due to the fact that objects and flat-fields are not imaged the same way. Dividing the two-dimensional frames of object and flat-field lamp by each other would then lead to an incorrect weighting of single pixels of the former one. The procedure described in the following mainly avoids this: The final goal of the whole data-reduction process is a one-dimensional spectrum that is generally achieved by summing up all the opaque lines within one stripe of the flat-field-corrected object frame whereby each line already represents a one-dimensional spectrum. Obvious reason for adding them up is enhancement of the signal strength and reduction of noise. Working with HET spectra, it is advisable to generate first a normalized two-dimensional flat-field frame out of the original one by dividing the latter by the smoothed version of itself. Applying this to the object frame should remove pixel-to-pixel variations solely caused by the CCD chip and therefore not correlated with the way of imaging. Subsequent summing over opaque lines of the object or smoothed flat-field image, respectively, yields one-dimensional curves whose ratio is a flat-field corrected flux profile of the object. The problem of improper weighting of pixels should be mitigated in this way since adding up pixels before division makes much less use of local information – right which is not given accurately in flat-fields from HET – than the standard method. Figure 3.4a shows the result of such a procedure: Apart from the effects of the huge absorption line the intensity is only slightly falling as expected for a stellar spectrum mixed with the smooth profile of the flat-field lamp. Figure 3.4b illustrates what happens when the final division by the smoothed one-dimensional flat-field is left out: a comparatively rapidly varying curve appears, dominated by the so-called Echelle blaze function. According to the theory of Echelle spectrography, the intensity profile of one order varies as $\sin^2(x)/x^2$ with x being a measure for the wavelength difference to the central wavelength in this order. Hence, the noise level increases towards the ends of each order being responsible for the large noise at the margins in Fig. 3.4a.

4. **Subtraction of background and dark current:** Each bright stripe in Fig. 3.2a, which is the signal coming from the object under investigation, is accompanied by two adjacent faint ones. Their origin is a region of the sky close to the object but not including it nor any other compact source. Therefore they

[1] According to HET's official website (`http://hydra.as.utexas.edu/?a=help&h=29#HRS`) it is "difficult and confusing" to apply flat-fielding for its spectra.

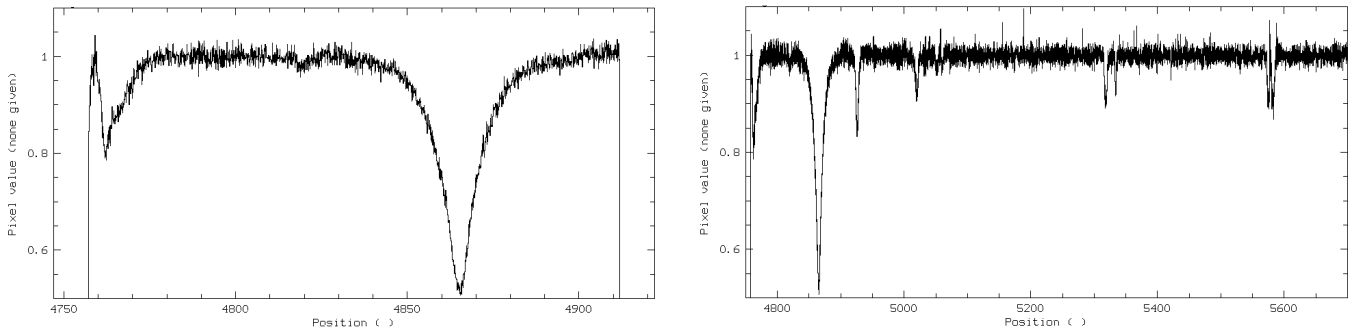

a: Normalized single-order Echelle spectrum

b: Normalized multi-order Echelle spectrum

Figure 3.5: Normalized single-order Echelle spectrum obtained via division of an object's flux curve by the continuum profile. Merging several orders yields the spectrum on the right-hand side.

contain information of a so-called background signal that is also inherent in the object image and correspondingly has to be subtracted from it. Background consists primarily of ground based light scattered in Earth's atmosphere or of photons stemming from widespread sources in the direction of observation. This subtraction automatically removes the dark current, an additional signal caused by thermal excitations inside of the detector during the recording which is anyway hold tiny by cooling down the detecting device to very low temperatures

5. **Normalization:** For the purposes of this work – and often in astronomical research – only the relative fluxes are of interest. So what one usually does is to normalize the spectrum, i.e., setting the continuum emission to unity. This can be done either with Fig. 3.4a or 3.4b because the only difference is the multiplication with a smooth function that is normalized out anyway. As the margins of the absorption lines and the continuum behavior are easier to detect in Fig. 3.4a it seems preferable to perform normalization there. Nevertheless, due to a special property of Echelle spectra this is not an argument excluding the method leading to Fig. 3.4b: The wavelength interval comprised by one diffraction order is so small that the influence of the slowly varying stellar radiation curve is almost negligible compared to effects caused by the spectrograph. Consequently the profile of Fig. 3.4b is essentially due to the spectrograph – apart from the absorption line of course. Moreover, experience shows that the form of the profile in adjacent orders changes not significantly. It is therefore possible to gain the continuum behavior, i.e., the flux profile, as if there were no absorption or emission lines, of an order of diffraction just by averaging, e.g., the continuum profiles of the orders above and below provided they are known. In case that the smoothed one-dimensional flat-field and the object's curve do not vary much from order to order, the same method can be applied for Fig. 3.4a, too. However, for extreme faint flat-field signals, e.g., encountered in the far blue regime of the optical spectrum, noise is dominating the smoothed one-dimensional flat-field making it different from one order to the other and, what is more, damaging the intended correction effect. Under such circumstances, normalizing the flat-fielded spectrum is impossible and one has to resort to Fig. 3.4b and perform the necessary steps there. Under normal conditions it makes no difference which way is chosen. Division of the object curve by the continuum profile finally leads to a normalized spectrum as illustrated in Fig. 3.5a.

6. **Wavelength calibration and merging:** Last but not least wavelength calibration has to be accomplished with the help of the known emission lines of the Thorium-Argon lamp shown in Fig. 3.2b. Assigning the true wavelength to each discrete line of the reference lamp enables one to interpolate between them in order to gain a continuous scale[1]. Eventually merging several orders of diffraction delivers a high-resolution and completely reduced stellar spectrum as shown in Fig. 3.5b. The noisy ends of the individual orders vanish as they are not used due to sufficient overlap of the orders.

[1] Actually, MIDAS fits a polynomial to derive the dispersion relation.

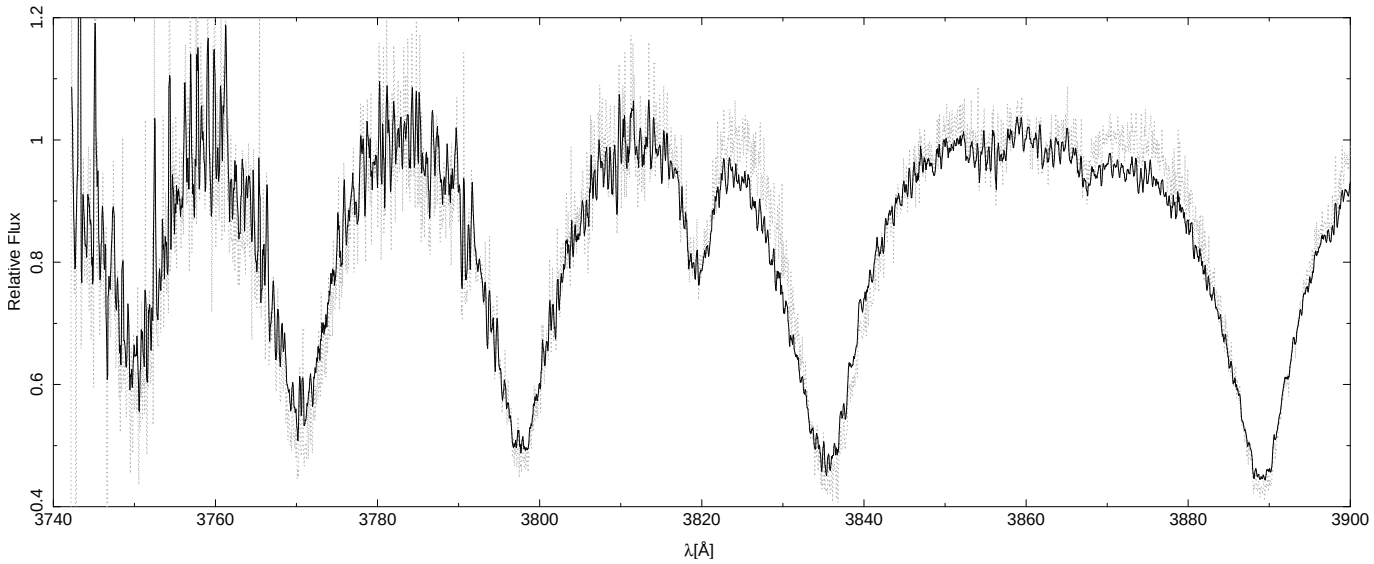

Figure 3.6: Final high-resolution Echelle spectrum of HIP 60350: Several high-order Balmer lines are visible. The black solid line is the fully optimized HET spectrum analyzed in this work. The gray dotted line is the corresponding co-added but untreated spectrum showing a worse S/N and a slightly incorrect continuum behavior.

For a conventional grating spectrograph data reduction does not differ considerably. In principle, it is analogously to the reduction of one Echelle order with the exceptions that there is no Echelle blaze function implying much less variations of sensitivity with wavelength and that you cannot normalize it by averaging adjacent orders. In this case, one has to use other methods of finding the continuum behavior, for instance comparison with a reference star or "by eye".

3.2 Observations and Optimization

HIP 60350 was observed in December 2008 with the high-resolution Echelle spectrograph of the 9.2 meter Hobby-Eberly Telescope[1] at McDonald Observatory resulting in three individual spectra with resolving power $\lambda/\Delta\lambda = 15\,000$ and wavelength range [3740 Å, 7870 Å]. Additionally, three low-resolution spectra ($1500 < \lambda/\Delta\lambda < 2500$) collected in May and July 2009 with the 3.5 meter telescope at Calar Alto[2] and its long-slit TWIN spectrograph are available enlarging the spectral coverage down to 3500 Å.

Apart from the spectral resolution $\lambda/\Delta\lambda$ there is a second important quantity characterizing the quality of a spectrum: the signal-to-noise ratio S/N. Noise, i.e., fluctuations in the detected signal, can result from temporal variations in the photon flux of the star and the sky background as well as from the equipment. According to Gray (2005, pp. 96-97) the noise level N can be roughly approximated by the square root of the signal S (Poisson statistics): $N \approx \sqrt{S}$. Hence the signal-to-noise goes more or less with $\sqrt{S}$ and can be improved by increasing the exposure time to catch more photons or by co-adding several spectra. Doing the latter for the three HET spectra leads to a S/N of about 100 in the blue visual range. This ratio can

[1]The Hobby-Eberly Telescope is a joint project of the University of Texas at Austin, the Pennsylvania State University, Stanford University, Ludwig-Maximilians-Universität München, and Georg-August-Universität Göttingen. The HET is named in honor of its principal benefactors, William P. Hobby and Robert E. Eberly (http://www.as.utexas.edu/mcdonald/het/het.html).

[2]The Centro Astronómico Hispano Alemán (CAHA) at Calar Alto is jointly operated by the Max-Planck Institut für Astronomie (MPIA) in Heidelberg, Germany, and the Instituto de Astrofísica de Andalucía (CSIC) in Granada, Spain (http://www.caha.es/).

be further increased by noting that the HET spectrum was oversampled, meaning that the resolution of the detector was better than the spectral one. According to the Nyquist criterion, it is sufficient to image a spectral element $\Delta\lambda$ on two pixels of the CCD. More than two pixels covered by $\Delta\lambda$, as being the case for the HET spectrum, contain no separate information and can be averaged. Applying a Gaussian filter with standard deviation $\sigma(\lambda) = \Delta\lambda = 15\,000\,\lambda$ to smooth the co-added spectrum leads to $S/N \approx 140$ in the blue.

Although being of insufficient resolving power to be useful for a precise spectroscopic investigation, the TWIN spectra provide valuable supplementary information. For instance, spectra of long-slit spectrographs have the advantage of being taken as one complete piece allowing the continuum behavior to be determined relatively easily, even by means of the eye. In cases where several adjacent diffraction orders of the Echelle spectrum are affected by lines and consequently the continuum is hardly accessible, the normalized low-resolution spectrum can be used as a reference. To do so, the high-resolution spectrum has to be convolved with the instrumental profile of the low-resolution one to make both comparable. Dividing the low-resolution spectrum by the blurred high-resolution one yields in good approximation the normalizing factor for the original Echelle spectrum. For HIP 60350 this method was utilized in the (most problematic) range from 3740 Å to 3900 Å.

Figure 3.6 depicts the blue region of the fully optimized HET spectrum that is analyzed in the remaining part of this work.

3.3 Model Atmospheres

3.3.1 Radiative Transfer

In atmospheres of B-type stars, the energy is carried outwards by means of radiative transport (see Sect. 2.3). The fundamental equation describing this process is denoted as *radiative transfer equation* and reads[1]:

$$\mathrm{d}I_\nu = -\kappa_\nu I_\nu \mathrm{d}s + \eta_\nu \mathrm{d}s \tag{3.1}$$

I_ν is the specific intensity mentioned in Sect. 2.1, κ_ν is the (macroscopic) absorption coefficient also called opacity, η_ν is the (macroscopic) emission coefficient and ds is an infinitesimal distance in direction of solid angle dΩ. The radiative transfer equation hence accounts for the changes of the macroscopic radiation field caused by absorption or emission of photons by the traversed matter. In general, the quantities κ_ν and η_ν are extremely complicated functions of the variables defining the state of the matter, for instance density ρ, temperature T or composition $\{X_Z\}$. They can be derived from microscopic physics according to

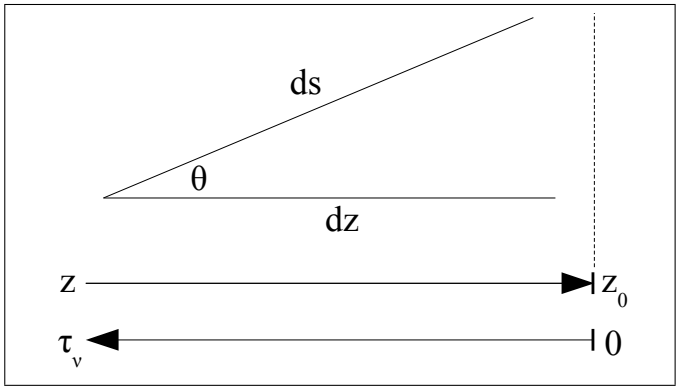

Figure 3.7: Plane-parallel coordinates z, $\cos(\theta) \equiv \mu$ and $\tau_\nu = -\int_{z_0}^{z} \kappa_\nu \mathrm{d}\tilde{z}$.

$$\kappa_\nu = \text{number of absorbers} \times \text{atomic cross-section}(\nu) \tag{3.2}$$

$$\eta_\nu \propto \text{number of emitters} \times \text{transition probability}(\nu) \tag{3.3}$$

whereby the latter are given by atomic physics. The dimension of κ_ν is length^{-1} therefore κ_ν^{-1} being the characteristic distance a photon can travel before getting absorbed. As outlined in Sect. 2.3, four different absorption cross-sections are distinguished: bound-bound, bound-free, free-free and scattering whereas the

[1] This is very different from the treatment of radiation transport in the stellar interior, where it can be approximated as a simple diffusion process due to the short mean free path of the photons.

last one is not a true absorption process. Bound-bound transitions are responsible for the absorption lines that occur in spectra while the other three processes contribute to the continuum behavior.

For later convenience, consider a plane-parallel geometry with distances $\mathrm{d}s$ being expressed by $\mathrm{d}z$ (direction of normal of the plane) and $\cos(\theta) \equiv \mu$ (θ: angle to normal) via $\mathrm{d}s = \mathrm{d}z\,\mu^{-1}$ (see Fig. 3.7). Further substitute $\mathrm{d}z = -\mathrm{d}\tau_\nu\,{\kappa_\nu}^{-1}$, whereby τ_ν is the *optical depth* and defined by $\tau_\nu = -\int_{z_0}^{z} \kappa_\nu \mathrm{d}\tilde{z}$:

$$\mu \mathrm{d}I_\nu = I_\nu \mathrm{d}\tau_\nu - \frac{\eta_\nu}{\kappa_\nu}\mathrm{d}\tau_\nu \tag{3.4}$$

Eq. 3.4 can be rewritten when introducing the *source function* $S_\nu = \frac{\eta_\nu}{\kappa_\nu}$:

$$\mu \frac{\mathrm{d}I_\nu}{\mathrm{d}\tau_\nu} = I_\nu - S_\nu \tag{3.5}$$

Once the source function is given, the radiative transfer equation reduces to a first-order differential equation with constant coefficients solved by an integrating factor $\exp(\frac{-\tau_\nu}{\mu})$:

$$\begin{aligned}
\mu \exp\left(\frac{-\tau_\nu}{\mu}\right)\frac{\mathrm{d}I_\nu}{\mathrm{d}\tau_\nu} &= \mu\frac{\mathrm{d}}{\mathrm{d}\tau_\nu}\left(I_\nu \exp\left(\frac{-\tau_\nu}{\mu}\right)\right) + I_\nu \exp\left(\frac{-\tau_\nu}{\mu}\right) = I_\nu \exp\left(\frac{-\tau_\nu}{\mu}\right) - S_\nu \exp\left(\frac{-\tau_\nu}{\mu}\right) \\
&\Rightarrow \quad \mu\frac{\mathrm{d}}{\mathrm{d}\tau_\nu}\left(I_\nu \exp\left(\frac{-\tau_\nu}{\mu}\right)\right) = -S_\nu \exp\left(\frac{-\tau_\nu}{\mu}\right) \\
&\Rightarrow \quad I_\nu(\tau_1,\mu) = I_\nu(\tau_2,\mu)\exp\left(-\frac{\tau_2-\tau_1}{\mu}\right) + \int_{\tau_1}^{\tau_2} S_\nu(\tilde{\tau_\nu})\exp\left(-\frac{\tau_2-\tilde{\tau_\nu}}{\mu}\right)\frac{\mathrm{d}\tilde{\tau_\nu}}{\mu}
\end{aligned} \tag{3.6}$$

Obviously, the emitted intensity I_ν in direction of positive μ at high optical depth τ_2 is exponentially weakened by absorption on its way to low optical depth τ_1. However, I_ν is continuously revived by emission, which again is attenuated.

Note that Eq. 3.6 is just a *formal solution* and in general not applicable because the source function S_ν is usually also a function of the specific intensity I_ν. This is due to the fact that by interaction with matter the radiation field influences the material's state and properties which in turn determine κ_ν and η_ν and thus S_ν.

3.3.2 Setting up a Model Atmosphere

In principle, the structure of stellar atmospheres, i.e., the region of the star from where the observed light is radiated, can be deduced from the same set of equations that defines the whole stellar structure (Eqs. 2.9). However, several assumptions can be made to simplify things:

1. **Plane-parallel geometry:** Typically, the thickness $\Delta R_\star$ of stellar atmospheres is small compared to the radius $R_\star$ of the star: $\Delta R_\star / R_\star \ll 1$. Hence, on length scales of interactions occurring in atmospheres the curvature of the star is negligible and a plane-parallel geometry is a good approximation.

2. **Homogeneity:** The atmosphere is supposed to be homogeneous in each layer, i.e., there are no variations perpendicular to its normal. Consequently, one single coordinate is sufficient to specify the location within the atmosphere. Coordinates in use are either z or τ_ν (see Fig. 3.7): z is increasing towards the outer part of the atmosphere with maximum $z_{\max} = z_0 = R_\star$, while the optical depth τ_ν increases towards the inner region and vanishes at the surface. Note that in contrast to z the optical depth is dimensionless and as seen in Eq. 3.6 a measure of extinction when considering fluxes emanating from the surface ($\tau_1 = 0$, $\mu > 0$). Due

to its frequency dependence, the same value of τ_ν does not correspond to the same geometrical position z for different wavelengths. In order to avoid this complication, a mean optical depth can be defined by virtue of the Rosseland mean opacity $\kappa_{\text{Rosseland}}$ which averages opacities over frequency with a particular weighting function: $\tau = -\int_{z_0}^{z} \kappa_{\text{Rosseland}} \mathrm{d}\tilde{z}$. τ is a wavelength-independent indicator for extinction.

3. **Stationarity:** Atmospheres are thought to be constant in time. Time-dependent effects such as pulsations are neglected. Accordingly, e.g., Cepheid stars are not well modeled in this way.

4. **Hydrostatic equilibrium:** Due to stationarity, the equation of hydrostatic equilibrium Eq. 2.9b is still valid and can even be simplified. Noting that the atmosphere is only a small layer at the outer rim of the star, hydrostatic equilibrium can be approximated by:

$$\frac{\mathrm{d}P(r)}{\mathrm{d}r} = -\frac{GM_\star(r)\rho(r)}{r^2} \approx -\frac{GM_\star}{R_\star^2}\rho(r) \equiv -g\rho(r) \quad \Rightarrow \quad \frac{\mathrm{d}P(z)}{\mathrm{d}z} = -g\rho(z) \tag{3.7}$$

The (constant) *surface gravity* $g = GM_\star R_\star^{-2}$ is an important parameter when characterizing stellar atmospheres and numerical values are usually given in $\log(g\,[\mathrm{cm\,s^{-2}}])$. Because of the approximations made, the mass continuity equation Eq. 2.9a has become superfluous.

Note that P is a combination of the pressure caused by the plasma, i.e., the electrons and ionized atoms, and of the radiation: $P = P_{\text{plasma}} + P_{\text{rad}}$. While P_{plasma} is calculated from the equation of state of the plasma, e.g., ideal gas law, an explicit expression for P_{rad} is given by the following (see Clayton, 1983, p. 108) where c is the speed of light:

$$P_{\text{rad}}(\nu) = \int_{4\pi} \frac{I_\nu}{c} \cos^2(\theta)\,\mathrm{d}\Omega \tag{3.8}$$

Eq. 3.8 can be used to estimate the effects of photon pressure on the atmospheric structure. Reasonably assuming κ_ν and η_ν to be isotropic and applying Eqs. 3.1, 2.3 in connection with $\mathrm{d}s = \mathrm{d}z\,\mu^{-1}$ yields:

$$\frac{\mathrm{d}P_{\text{rad}}(\nu)}{\mathrm{d}z} = \frac{1}{c}\int_{4\pi} \frac{\mathrm{d}I_\nu}{\mathrm{d}z} \cos^2(\theta)\,\mathrm{d}\Omega \overset{3.1}{=} -\frac{\kappa_\nu}{c}\int_{4\pi} I_\nu \cos(\theta)\,\mathrm{d}\Omega \overset{2.3}{=} -\frac{\kappa_\nu}{c}F_\nu \tag{3.9}$$

Integration over frequencies results in

$$\frac{\mathrm{d}P_{\text{rad}}}{\mathrm{d}z} = \int_0^\infty \frac{\mathrm{d}P_{\text{rad}}(\nu)}{\mathrm{d}z}\mathrm{d}\nu = -\frac{1}{c}\int_0^\infty \kappa_\nu F_\nu \mathrm{d}\nu = -\frac{1}{c\rho(z)}\int_0^\infty \kappa_\nu F_\nu \mathrm{d}\nu\rho(z) \equiv -g_{\text{rad}}\rho(z) \tag{3.10}$$

finally leading to:

$$\frac{\mathrm{d}P_{\text{plasma}}(z)}{\mathrm{d}z} = -g\rho(z) - \frac{\mathrm{d}P_{\text{rad}}}{\mathrm{d}z} = -\rho(z)\,(g - g_{\text{rad}}) \tag{3.11}$$

Here, the radiative acceleration $g_{\text{rad}} = \frac{1}{c\rho(z)}\int_0^\infty \kappa_\nu F_\nu \mathrm{d}\nu$ was introduced. For main-sequence B-type stars it is weak compared to the surface gravity g. On the other hand, the already mentioned stellar winds of massive O-type or Wolf-Rayet stars are a direct consequence of $g_{\text{rad}} > g$ resulting in a break-down of hydrostatic equilibrium and dynamic outflow of stellar matter into space. Obviously, such atmospheres are much harder to handle since hydrodynamic effects and as a consequence mass loss have to be taken into account.

5. **Radiative equilibrium:** A static atmosphere implies energy conservation for each point separately. Therefore the amount of energy per unit volume absorbed by the matter must compensate for the loss caused by emission:

$$\int_0^\infty \int_{4\pi} \kappa_\nu I_\nu \mathrm{d}\Omega\mathrm{d}\nu \overset{!}{=} \int_0^\infty \int_{4\pi} \eta_\nu \mathrm{d}\Omega\mathrm{d}\nu \tag{3.12}$$

Substituting $\mathrm{d}s = \frac{\mathrm{d}z}{\mu} = \frac{\mathrm{d}z}{\cos(\theta)}$ in Eq. 3.1, integrating over solid angle and frequency and applying Eq. 3.12:

$$\int_0^\infty \int_{4\pi} \cos(\theta) \frac{\mathrm{d}I_\nu}{\mathrm{d}z} \mathrm{d}\Omega \mathrm{d}\nu = \int_0^\infty \int_{4\pi} (-\kappa_\nu I_\nu + \eta_\nu) \mathrm{d}\Omega \mathrm{d}\nu = 0 \tag{3.13}$$

Switching integration and differentiation together with Eq. 2.3 yields:

$$\frac{\mathrm{d}}{\mathrm{d}z} \int_0^\infty \int_{4\pi} \cos(\theta) I_\nu \mathrm{d}\Omega \mathrm{d}\nu = \frac{\mathrm{d}}{\mathrm{d}z} \int_0^\infty F_\nu \mathrm{d}\nu = \frac{\mathrm{d}F}{\mathrm{d}z} = 0 \quad \Rightarrow \quad F = \text{constant} \tag{3.14}$$

Thus, in plane-parallel geometry local energy conservation directly leads to flux conservation. According to the Stefan-Boltzmann law, the constant flux can be linked to the effective temperature: $F = \sigma T_{\mathrm{eff}}^4$. T_{eff} is the second important parameter describing the state of an atmosphere. Note that Eq. 3.14 is just the plane parallel version of Eq. 2.9c since in case of stellar atmospheres the right-hand side of the latter vanishes due to stationarity and too low temperatures to allow energy generation by nuclear reactions.

In summary, the basic system of integro-differential equations dictating the atmospheric structure depending on the input parameters g and T_{eff} reads:

$$\frac{\mathrm{d}P_{\mathrm{plasma}}(z)}{\mathrm{d}z} = -\rho(z) \left(g - \frac{1}{c\rho(z)} \int_0^\infty \kappa_\nu \int_{4\pi} I_\nu \cos(\theta) \, \mathrm{d}\Omega \mathrm{d}\nu \right) \tag{3.15a}$$

$$\int_0^\infty \int_{4\pi} \cos(\theta) I_\nu \mathrm{d}\Omega \mathrm{d}\nu = \sigma T_{\mathrm{eff}}^4 \tag{3.15b}$$

$$\mu \frac{\mathrm{d}I_\nu}{\mathrm{d}\tau_\nu} = I_\nu - S_\nu \tag{3.15c}$$

The system 3.15, which couples all frequencies, depths and angles to each other, is numerically treated in a standard way, namely, by discretization and linearization. Of course, there are several additional equations which contain further constraints such as charge conservation or the equation of state of an ideal gas which have to be fulfilled, too. Further note that Eq. 2.9d is left out in favor of Eq. 3.15c. As will be explained in the next section, the former is just a special case of the latter provided the atmosphere is not convective.

As already indicated at the end of Sect. 3.3.1, the most serious problem one is faced with when trying to solve the coupled system 3.15 is the source function. The specific form of S_ν is by no means trivial and combines macroscopic (temperature, density, composition, ... of the plasma) as well as microscopic (atomic cross-sections, transition probabilities) quantities. Therefore, solving this highly complex system is no simple task. The typical way to do so is an iterative approach. First, one has to choose a trial atmosphere as starting point. That initial guess could be either the result of a previous calculation for similar surface gravity and effective temperature or an analytical expression obtained by making far-reaching simplifications that allow the system of differential equations to be solved exactly (for instance the gray approximation). The trial structure certainly will not fulfill Eqs. 3.15, but its application to the system provides hints of how to change it to make it work. This is done iteratively, meaning that one varies for instance the temperature profile implicitly present in Eq. 3.15c in S_ν while keeping the remaining part fixed. The improved temperatures can in turn be inserted into equation Eq. 3.15a via the ideal gas law to derive a new guess for density or pressure, respectively. These new functions can again be substituted in Eq. 3.15c to gain a new photon flux I_ν which has to be further altered in order to satisfy Eq. 3.15b. Once the trial functions for all physical quantities are updated, the procedure can start anew. The iterations are continued until a certain convergence criterion is

reached, i.e., the differences between new and old structure are below a given threshold. The final atmosphere can eventually be used to compute a synthetic, normalized model spectrum.

The predictive power and physical correctness of synthetic spectra naturally depend on the assumptions made. In particular, the question of how to treat the source function is crucial. In the next section, the concepts of *local thermodynamic equilibrium* (LTE) and *non-local thermodynamic equilibrium* (NLTE) will be introduced which deeply impact the form of S_ν and accordingly the outcome of the calculations.

3.3.3 Local versus Non-Local Thermodynamic Equilibrium

Apart from a precise description of the atomic structure (energy and ionization levels, statistical weights, cross sections, transition probabilities, ...) of the different chemical species via so-called *model atoms* – which can consume a whole Ph.D. thesis to be build up – computing the source function requires detailed knowledge of the statistical properties of the plasma: What percentage of atoms of a certain chemical element is found in a specific excitation/ionization level? How many particles per volume are there at all? What is their velocity distribution? Nowadays, there are two approaches in use trying to answer these questions.

LTE: The principle of thermodynamic equilibrium of statistical physics has proven to be extremely powerful and is applied in many distinct fields of physics. However, it cannot be valid for stars in a global manner since regional conditions such as gravity strongly differ within them and additionally they generate energy preventing them from getting into equilibrium with their environment. Nevertheless, thermodynamic equilibrium can be assumed locally, meaning that each individual volume element or each layer in a plane-parallel geometry, respectively, is in thermodynamic equilibrium and therefore can be described by a local temperature T. Note that this concept is solely used to obtain the source function and therefore applies to the plasma, i.e., massive particles, but not to the radiation field which is still determined by the radiative transfer equation and not via Planck's function. According to statistical physics, LTE implies:

- A Maxwellian velocity distribution with Boltzmann constant k, particle mass m and velocity v:

$$p(v)\mathrm{d}v = \left(\frac{m}{2\pi kT}\right)^{\frac{3}{2}} \exp\left(-\frac{mv^2}{2kT}\right) 4\pi v^2 \mathrm{d}v \tag{3.16}$$

- A Boltzmann excitation formula with occupation number density n_i, statistical weight g_i and energy E_i of the ith excitation level referred to the ground state of the ion:

$$\frac{n_j}{n_i} = \frac{g_j}{g_i} \exp\left(-\frac{E_j - E_i}{kT}\right) \tag{3.17}$$

- A Saha ionization equation with total number density N_I of the ionization stage I, electron mass m_e, electron number density n_e, Planck constant h, partition function $G_I = \sum_{i=0}^{i_\mathrm{max}} g_i \exp(-\frac{E_i}{kT})$ and ionization potential χ_I of the respective ion:

$$\frac{N_{I+1}}{N_I} = \frac{2}{n_\mathrm{e}} \frac{G_{I+1}}{G_I} \frac{(2\pi m_\mathrm{e} kT)^{\frac{3}{2}}}{h^3} \exp\left(\frac{-\chi_I}{kT}\right) \tag{3.18}$$

Equations 3.17 and 3.18 in combination with charge conservation $\sum_i n_i Z_i - n_\mathrm{e} = 0$ for fixing n_e yield all occupation number densities. Z_i is hereby the charge associated with level i. Together with the information contained in the model atoms, this set of equations allows for the calculation of the local source function.

The typical mean-free paths of photons tremendously exceed the small distances traveled by massive particles before being scattered. Hence it is the interaction with the radiation field that causes departure from local

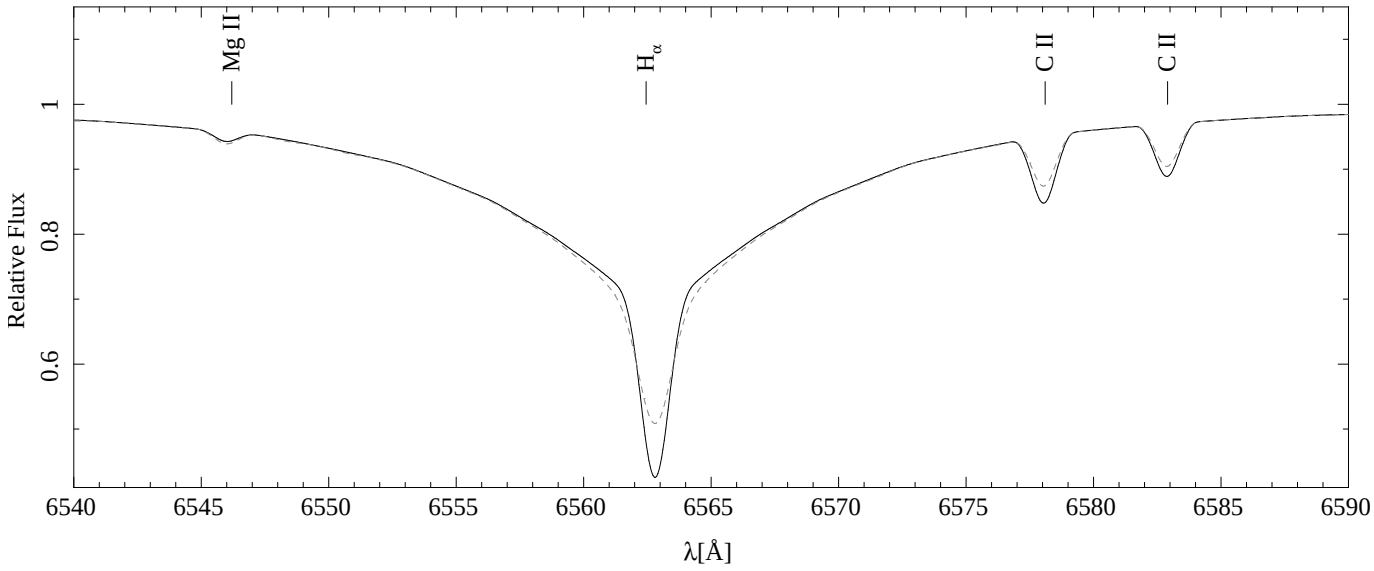

Figure 3.8: Comparison of NLTE (solid black line) and LTE (dashed gray line) model with equal $T_{\rm eff} = 16\,100\,\mathrm{K}$ and $\log(g\,[\mathrm{cm\,s^{-2}}]) = 4.1$. Evidently, accounting for non local effects is absolutely necessary when studying B-type stars.

thermodynamic behavior. If the photon flux is weak or the particle density high, particle-particle interactions such as collisions dominate over particle-photon interactions and LTE is an excellent approximation. For instance, this is the case in the stellar interior. As shown by Clayton (1983, Chap. 3.2), adopting LTE Eq. 3.15c can be transformed to Eq. 2.9d finally proving the complete analogy of Eqs. 2.9 and 3.15.

The huge advantages of LTE is the fact that analytical expressions exist to determine the population number densities. Thus numerical computations are much faster than those of NLTE models.

NLTE: If the radiation field influences the excitation/de-excitation of atomic levels, deviations from LTE will occur. The corresponding state is said to be in NLTE. To account for this, Eqs. 3.17 and 3.18 have to be replaced by more general equations, the so-called statistical equilibrium or rate equations:

$$n_i \sum_{j\neq i} (R_{ij} + C_{ij}) + n_i(R_{ik} + C_{ik}) = \sum_{j\neq i} n_j(R_{ji} + C_{ji}) + n_k(R_{ki} + C_{ki}) \tag{3.19}$$

Here, R_{ij} and C_{ij} are the radiative and collisional rates for transitions from the level i to level j whereas R_{ik} and C_{ik} label the respective ionization rates. The rate equations consequently demand that the sum of rates depopulating the state i (left-hand side) must exactly cancel those populating it (right-hand side). The rates are functions of the radiation field, particle velocity distribution and atomic cross-sections. Thus, the set of statistical equations for all levels together with the *total number conservation equation* $\sum_{\rm levels} n_i = N_{\rm element}$ form an extremely complex, non-linear system of coupled equations that has to be solved in order to obtain the occupation number densities and in this way S_ν. Moreover, Eqs. 3.19 are coupled to the system 3.15 and have to be solved simultaneously with that. The numerical effort is thus increased so much that calculations of synthetic NLTE spectra can take days on a fast PC's CPU instead of minutes as for LTE. Eventually note that speaking of NLTE does not imply a complete renunciation from LTE principles as, e.g., the velocity distribution is still assumed to be Maxwellian.

Statistical equilibrium is a generalization of local thermodynamic equilibrium and the latter is restored when the radiation field equals Planck's function or in the limit of $C_{ij} \gg R_{ij}$. Due to large effective temperatures and modest surface gravities, the analysis of B-type stars is crucially affected by NLTE effects as demonstrated in Fig. 3.8.

3.3.4 Hybrid LTE/NLTE Models with ATLAS, DETAIL and SURFACE

Constructing a single synthetic model completely in NLTE is an expensive numerical task and costs a lot of time. Unfortunately, the determination of spectroscopic parameters is based on a whole grid of models in a multi-dimensional parameter space ($T_{\rm eff}$, g, $\{X_Z\}$, ...) demanding hundreds of models to be calculated. In order to do this in reasonable time, some simplifications can be applied which save plenty of time while preserving the NLTE features of the spectrum. The hybrid LTE/NLTE approach used in this work is discussed by Nieva & Przybilla (2006, 2007, 2008) and Przybilla et al. (2006) who also show the reliability of the method for stars like the one investigated in the following. The principle idea is to split up the problem in three parts:

1. **ATLAS:** Calculate an LTE model atmosphere with the program ATLAS9 (Kurucz, 1993).

2. **DETAIL:** The resulting ATLAS9 atmosphere is the starting point of a NLTE computation with DETAIL (Giddings, 1981; Butler & Giddings, 1985). Hereby, the ATLAS9 structure of the plasma remains fixed, i.e., temperatures and densities are not altered any more. On the other hand, by solving the coupled rate and radiative transfer equations the population number densities as well as the photon flux are recomputed in NLTE.

3. **SURFACE:** Basically, the problem is solved at this point. To speed up calculations, however, the frequency grid in DETAIL is relatively large and approximate line-broadening is used. Thus the DETAIL flux is insufficient to reproduce the specific shape of spectral lines in a comprehensive way. Nevertheless, knowledge of the NLTE occupation number densities determines the source function S_ν. Using a considerably finer frequency grid and refined line-formation data – for instance including detailed line profiles and fine-structure – than possible in DETAIL, the program SURFACE (Giddings, 1981; Butler & Giddings, 1985) allows the final radiation field to be determined precisely. By means of the formal solution Eq. 3.6, the flux emerging at the stellar surface ($\tau_\nu = 0$) is then:

$$I_\nu(0,\mu) = I_\nu(\tau_0,\mu)\exp\left(-\frac{\tau_0}{\mu}\right) + \int_0^{\tau_0} S_\nu(\tilde{\tau_\nu})\exp\left(-\frac{\tau_0-\tilde{\tau_\nu}}{\mu}\right)\frac{\mathrm{d}\tilde{\tau_\nu}}{\mu} \tag{3.20}$$

   Here, τ_0 denotes the optical depth at the inner rim of the photosphere. It has to be chosen such that the inner boundary condition of LTE is established. In practice, values of $\tau_0 \approx$ 100-200 are a reasonable choice.

   Assuming a spherical star, the radiated flux seen by an observer is the sum of all fluxes that are directed to the (infinite) distant observer. Approximating the atmosphere at each stellar surface point by a plane-parallel geometry, the observed spectrum $F_\nu(0)$ is given by integration of $I_\nu(0,\mu)$ over a hemisphere[1] (see Fig. 3.9a):

$$F_\nu(0) = 2\pi\int_0^1 \left(I_\nu(\tau_0,\mu)\exp\left(-\frac{\tau_0}{\mu}\right) + \int_0^{\tau_0} S_\nu(\tilde{\tau_\nu})\exp\left(-\frac{\tau_0-\tilde{\tau_\nu}}{\mu}\right)\frac{\mathrm{d}\tilde{\tau_\nu}}{\mu}\right)\mathrm{d}\mu \tag{3.21}$$

   In order to obtain a normalized synthetic spectrum, one has to calculate the continuum flux $F_\nu^{\rm cont}(0)$ as well, i.e., considering solely continuous absorption and emission coefficients while completely omitting discrete line transitions in S_ν. The final model spectrum is hence given by:

$$F_\nu^{\rm norm} = \frac{F_\nu(0)}{F_\nu^{\rm cont}(0)} \tag{3.22}$$

[1] Note that using the notation F_ν is consistent with Eq. 2.3 as the solid angle integration in Eq. 3.21 can be expanded over the whole sphere without consequences as $I_\nu(0,\mu<0)=0$. The latter is an imposed boundary condition when solving Eqs. 3.15 and states that no light enters the star from outside.

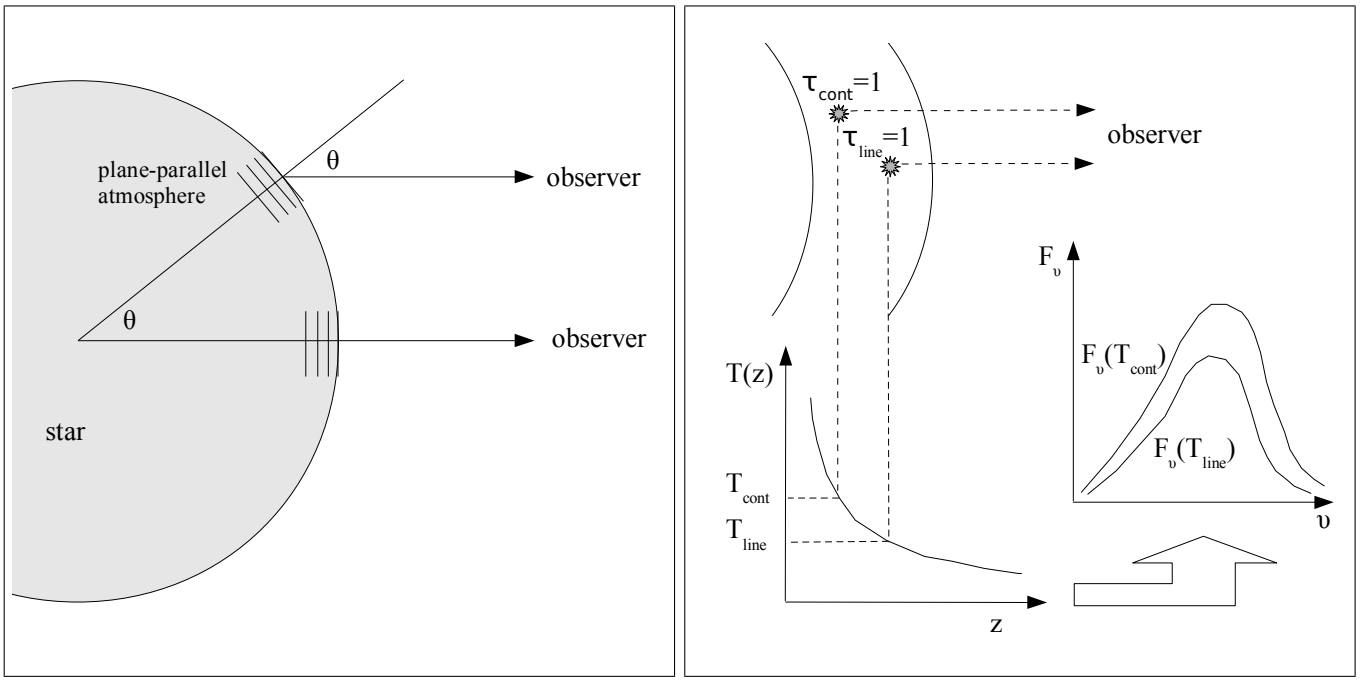

a: Radiated stellar flux seen by an observer

b: Formation of absorption lines

Figure 3.9: The spectrum emitted by a star can be calculated from integrating the specific intensity $I_\nu(0,\mu)$ from a plane-parallel geometry over a hemisphere. The observation of absorption lines results from the larger opacity at wavelengths that correspond to atomic transitions. Due to their larger $\kappa_{\rm line}$, the emanating flux stems from outer, cooler layers of the atmosphere implying a smaller intensity.

This can be rewritten in wavelength space using $|F_\nu \mathrm{d}\nu| = |F_\lambda \mathrm{d}\lambda|$ and $\lambda\nu = c$:

$$F_\lambda = \frac{c}{\lambda^2} F_\nu(c\,\lambda^{-1}) \quad \Rightarrow \quad F_\lambda^{\rm norm} = F_\nu^{\rm norm}(c\,\lambda^{-1}) \tag{3.23}$$

Another simplification made with respect to full NLTE models is that population number densities for different chemical species are computed separately. This approach is justified as the coupling between the various elements in the stars under consideration has at most tiny effects on their level distribution but largely reduces computational efforts. With hydrogen and helium being by far the most abundant elements, this does not apply for them of course. Therefore, the DETAIL calculations for metals are always performed accounting for hydrogen and helium populations in NLTE as background opacities. In the end, the individual NLTE populations are used altogether to perform a final SURFACE run taking all elements into consideration. The contributions of the omitted species to the source function are included either via so-called *opacity distribution functions* (ODFs) or the method of *opacity sampling* (OS), both of which are based on simplified LTE principles. In the OS approach, the spectrum is sampled by a large number of frequency points, for each of which the opacity of the discarded elements is approximated by LTE statistics. The opacities are always calculated anew depending on the state of the atmosphere. In contrast, ODFs are tabulated opacities, e.g., as a function of temperature and pressure. They are calculated once for a certain chemical composition and a fine frequency grid. From this detailed computation, a monotonic function of frequency is formed and listed. ODFs have the advantage of providing quick access to the source function as one only has to interpolate pre-tabulated values. On the other hand, they have the drawback that they are not suited to handle stars with non-standard chemical composition. The inclusion of OS/ODFs is especially important to allow for *line blanketing*, that is the redistribution of the photon flux by several hundred thousands of densely packed lines in particular in the ultra-violet spectral region. These lines form a kind of background opacity blocking the flux in the UV and by virtue of flux conservation Eq. 3.15b shift it to longer wavelengths.

The LTE/NLTE hybrid method described so far has proven to yield results as good as or superior than the so-called self-consistent NLTE codes but in a considerably shorter time – roughly an hour instead of a day.

3.3.5 Principles of Line Formation

The formation of spectral lines is caused by discrete atomic transitions either absorbing or emitting light of particular wavelength. Here, the energy of the photons is identical to the difference in energy of the involved levels. As the structure of atomic levels and hence possible line transitions are unique for each element, spectral lines are the fingerprints of chemical species.

The presence of absorption lines stems from the fact that the line opacity κ_{line} exceeds the surrounding continuous opacity κ_{cont} due to additional absorption via bound-bound transitions. By virtue of the definition of $\tau_\nu = -\int_{z_0}^{z} \kappa_\nu \mathrm{d}\tilde{z}$, the same optical depth $\tau_\nu = 1$ is then reached for a lower geometrical distance $z_0 - z$. As already mentioned, the optical depth is a measure of extinction and $\tau_\nu = 1$ can be interpreted as typical distance at which it is possible to look into a medium. Therefore, the continuous flux arriving at the observer originates at deeper stellar layers than the one associated with the spectral line (see Fig. 3.9b). According to Eq. 2.9d, which holds qualitatively also in NLTE atmospheres, the temperature is increasing towards the star's center. Consequently, the continuum is radiated from hotter regions implying also a higher intensity than the line flux that was produced in cooler outer layers.

The specific form of spectral lines depends on the one hand on atomic properties of the chemical element, on the other hand on the state of the surrounding plasma. In the following, the basic ideas behind the most important features are introduced:

- **Natural line width:** Excited atomic states are not stable and decay after a characteristic lifetime Δt. Heisenberg's uncertainty principle $\Delta E \Delta t \geq h$ states that the energy difference E_0 of excited and de-excited level is not sharp but has an intrinsic spread ΔE that translates into a range of energies for the emitted photon. The corresponding distribution over frequency Φ_ν can be derived from a classical damped oscillator to give a Lorentz profile:

$$\Phi_\nu^{\mathrm{natural}} = \frac{\gamma_{\mathrm{rad}}/4\pi^2}{(\nu - \nu_0)^2 + (\gamma_{\mathrm{rad}}/4\pi)^2} \tag{3.24}$$

  The damping constant γ_{rad} can be measured experimentally or obtained theoretically from quantum mechanical calculations of transition probabilities. The central frequency ν_0 is derived from $E_0 = h\nu_0$.

- **Pressure broadening:** The ions of the plasma are not isolated but interact with each other via Coulomb forces. These perturbations influence the atomic structure of the particles and lead to shifts of the energy levels. Their effects grow with increasing pressure since the latter implies closer distances and hence stronger Coulomb forces. In hot stars, such as type B ones, where the number of charged particles is high, the relevant interactions are the linear and quadratic Stark effect. The former affects atoms with intrinsic dipole moments such as neutral hydrogen or singly ionized helium while all others are subject to the latter. Depending on whether the interaction duration is short (impact approximation) or long (quasi-static approximation) compared to the lifetimes of the energy levels, the energetic shifts are different. For densities not too large, the short-term perturbations of the impact approximation dominate pressure broadening and can again be described in frequency space by a Lorentz profile $\Phi_\nu^{\mathrm{pressure}}$ according to Gray (2005, pp. 240-253).

- **Thermal Doppler broadening:** By virtue of the well-known Doppler effect, the frequency ν of absorbed and emitted photons is shifted by an amount $\Delta\nu$ due to the particle's line-of-sight velocity v:

$$\frac{\Delta\nu}{\nu} = \frac{v}{c} \tag{3.25}$$

In thermodynamic equilibrium, the thermal velocity distribution $p(v)$ in an arbitrary spatial direction is Gaussian:

$$p(v) = \frac{1}{\sqrt{\pi} v_0} \exp\left(-\frac{v^2}{v_0^2}\right) \tag{3.26}$$

Here, $v_0 = \sqrt{2kT/m}$ is the most probable velocity for particles of mass m at temperature T. The thermal Doppler profile in frequency space $\Phi_\nu^{\mathrm{th}}(\Delta\nu)$ results from the combination of the two preceding equations together with the requirement $\Phi_\nu^{\mathrm{th}}(\Delta\nu)\mathrm{d}\Delta\nu = p(v)\mathrm{d}v$:

$$\Phi_\nu^{\mathrm{th}}(\Delta\nu) = p(v)\frac{\mathrm{d}v}{\mathrm{d}\Delta\nu} = \frac{c}{\sqrt{\pi} v_0 \nu} \exp\left(-\frac{\Delta\nu^2 c^2}{v_0^2 \nu^2}\right) = \frac{1}{\sqrt{\pi}\Delta\nu_{\mathrm{D}}^{\mathrm{th}}} \exp\left(-\frac{\Delta\nu^2}{\Delta\nu_{\mathrm{D}}^{\mathrm{th}\,2}}\right) \tag{3.27}$$

The last step defines the Doppler width $\Delta\nu_{\mathrm{D}}^{\mathrm{th}} = \nu v_0/c$.

- **Non-thermal Doppler broadening or microturbulence:** In order to match synthetic, hydrostatic model spectra to observations, an additional non-thermal velocity component has to be postulated: *microturbulence*. One can think of it as small-scale motions well below the photon mean-free-path which are erroneously neglected in hydrostatic models. For simplicity, it is a standard practice to incorporate the effects of microturbulence by assuming its distribution to be Gaussian with dispersion ξ:

$$p(v) = \frac{1}{\sqrt{\pi}\xi} \exp\left(-\frac{v^2}{\xi^2}\right) \tag{3.28}$$

Defining $\Delta\nu_{\mathrm{D}}^{\mathrm{nth}} = \nu\xi/c$ and performing the same argumentation as for thermal motions, the corresponding frequency profile is:

$$\Phi_\nu^{\mathrm{nth}}(\Delta\nu) = \frac{1}{\sqrt{\pi}\Delta\nu_{\mathrm{D}}^{\mathrm{nth}}} \exp\left(-\frac{\Delta\nu^2}{\Delta\nu_{\mathrm{D}}^{\mathrm{nth}\,2}}\right) \tag{3.29}$$

Note that the implementation of microturbulence is rather artificial and thus controversial especially as recent hydrodynamical models have delivered good results without relying on this concept. However, it is a necessary part of the synthetic atmospheres used in this work. Typical values for ξ are of the order of $1\,\mathrm{km\,s^{-1}}$ whereas $v_0 \approx 16\,\mathrm{km\,s^{-1}}$ for hydrogen and $v_0 \approx 2\,\mathrm{km\,s^{-1}}$ for iron at $T = 16\,100\,K$.

The previous processes are all uncorrelated and hence can be combined via multiple convolutions of the individual line profiles to give the total profile. Using the fact that convolutions are associative and commutative and that the convolution of two Gaussian/Lorentz functions is again a Gaussian/Lorentz function yields:

$$\Phi_\nu^{\mathrm{total}} = \Phi_\nu^{\mathrm{natural}} * \Phi_\nu^{\mathrm{pressure}} * \Phi_\nu^{\mathrm{th}} * \Phi_\nu^{\mathrm{nth}} = \Phi_\nu^{\mathrm{Lorentz}} * \Phi_\nu^{\mathrm{Gauss}} \equiv \Phi_\nu^{\mathrm{Voigt}} \tag{3.30}$$

So the total line profile is a *Voigt* function, which is by definition the convolution of a Gaussian and a Lorentz function. An example is depicted in Fig. 3.10a and reveals that the wings of the Voigt function are still represented quite well by a Lorentz profile while the core is still Gaussian. Therefore the outer regions of absorption lines are good indicators for the pressure and thus for the surface gravity g whereas the center is influenced mostly by temperature induced Doppler broadening. Note that the profile function $\Phi_\nu^{\mathrm{total}}$ describes the frequency dependence of the bound-bound emission and absorption coefficients η_ν and κ_ν and consequently influences the source function S_ν but – strictly speaking – does not give the form of spectral lines. However, the line profile function is by far the most important feature when modeling spectral lines so that there is an almost one-to-one correspondence between them.

The broadening mechanisms explained so far are responsible for microscopic impacts on the shape of spectral lines. However, there are two more effects to be taken into consideration to completely reproduce observations.

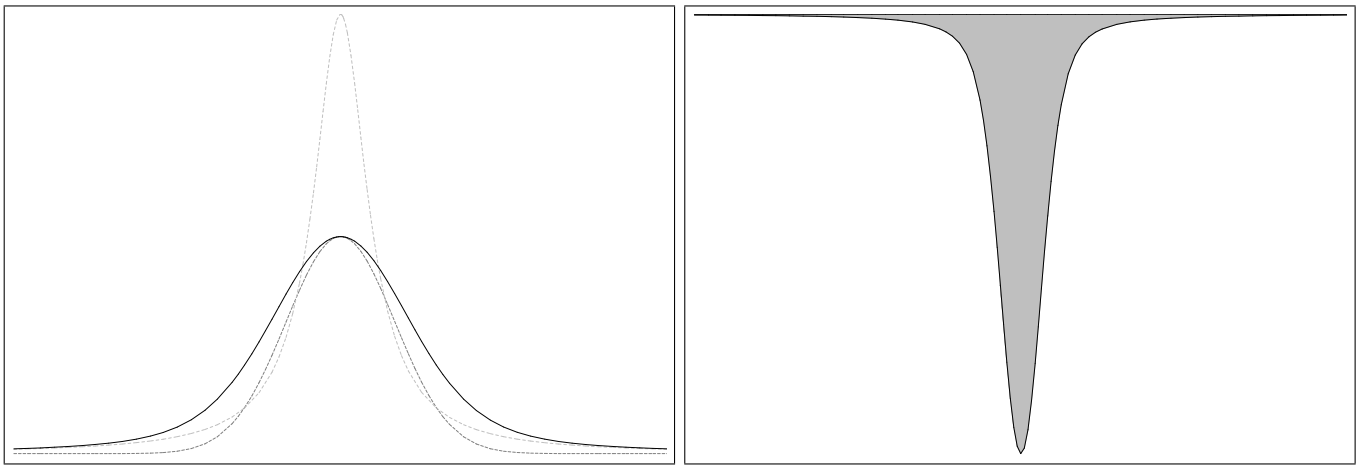

a: Voigt profile b: Equivalent width

Figure 3.10: The Voigt profile (black solid line) is the convolution of a Gaussian (dark-gray dashed line) and a Lorentz (light-gray dashed line) function which are also the limiting cases for tiny and large deviations from the central peak. Note that the Gaussian was rescaled before being plotted in order to fit to the Voigt function. The equivalent width (EW) of a line is defined to be the width of a rectangle of height 1 that encloses the same area (gray) between the normalized flux and the line of value unity.

- **Rotational broadening:** The equatorial rotational velocity $v_{\rm rot}$ of stars ranges from a few up to several hundreds of kilometers per second being sometimes close to the individual break-up velocity. In particular, young objects are often fast rotators. The actually observed rotational velocity $v_{\rm rot}^{\rm observed}$ is the projection of the velocity vector on the line-of-sight direction, commonly expressed by the inclination angle i between rotational axis and line-of-sight: $v_{\rm rot}^{\rm observed} = v_{\rm rot} \sin i$. This observed velocity component leads once more to a Doppler shift of photon wavelengths, but this time on macroscopic scales.

  To account for rotation, one has to sum up the geometrically weighted fluxes emerging from different parts of the projected disk of the rotating star as resolving the stellar surface is – apart from the Sun and a few other stars – not possible and observed fluxes are hence typically integrated ones. As shown by Gray (2005, pp. 458-467), assuming some minor simplifications this integration can be sufficiently approximated by the much simpler convolution of the normalized flux with the following rotational profile:

$$G(\lambda, \Delta\lambda) = \begin{cases} \dfrac{2(1-\beta)\sqrt{1-\left(\frac{\Delta\lambda}{\Delta\lambda_{\rm max}}\right)^2}+\frac{1}{2}\pi\beta\left(1-\left(\frac{\Delta\lambda}{\Delta\lambda_{\rm max}}\right)^2\right)}{c\pi\Delta\lambda_{\rm max}\left(1-\frac{\beta}{3}\right)}\lambda & , |\Delta\lambda| \leq |\Delta\lambda_{\rm max}| \\ 0 & , \text{else} \end{cases} \tag{3.31}$$

  Here, $\Delta\lambda_{\rm max} = \lambda v_{\rm rot} \sin i\, c^{-1}$ is the maximum Doppler shift and $\beta \approx 0.3$ is the (linear) limb darkening coefficient derived from fitting the simplified law $I_{\rm cont}(\mu) = I_{\rm cont}^{\rm center}(1 - \beta + \beta\mu)$ to sophisticated computations. Hence β describes the decrease in continuum intensity when going from the stellar disk's center to the edges caused by a smaller μ in Eq. 3.6.

  The profile of Eq. 3.31 is plotted in Fig. 3.11a and its effect on spectral lines is illustrated in Fig. 3.11b. Especially the blending of initially distinct lines and the smearing out of weak lines complicate the analysis of fast rotators.

- **Instrumental profile:** Spectral lines are blurred due to the finite resolution of the spectrograph. This broadening is assumed to have a Gaussian form with wavelength dispersion $\sigma(\lambda) = \Delta\lambda(2\sqrt{\ln(2)})^{-1}$. The factor $2\sqrt{\ln(2)}$ arises from the fact that $\Delta\lambda$ is experimentally measured as the full width at half maximum of a Gaussian fit to the emission lines of the reference lamp (Fig. 3.2b) because these are affected essentially by the instrumental profile. In case of an almost constant continuum flux over a

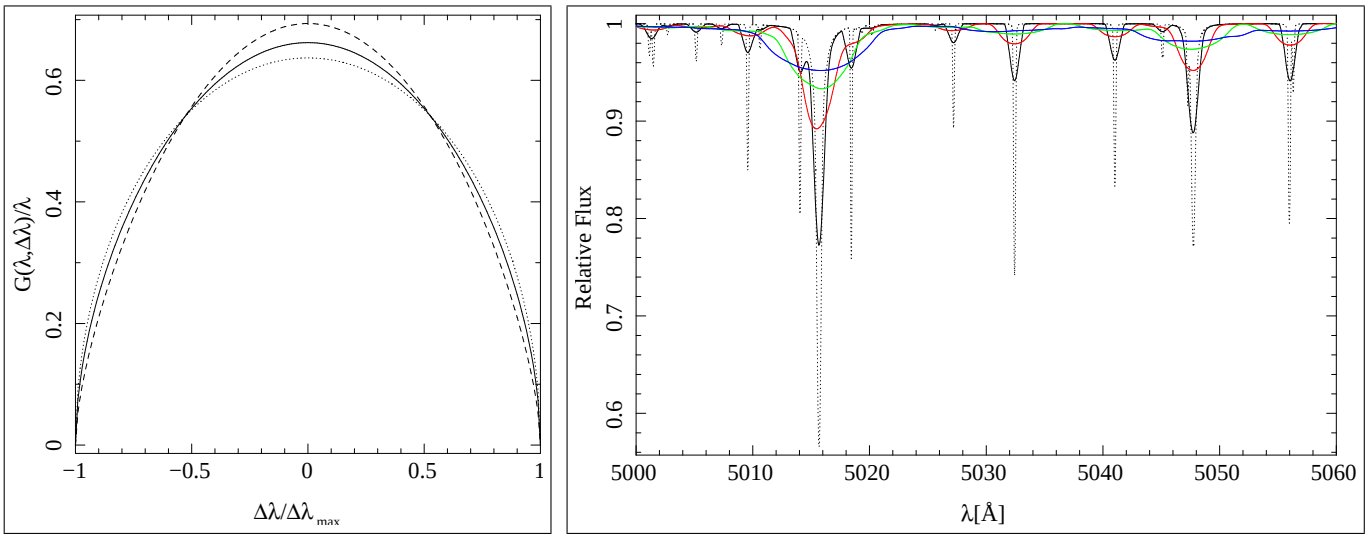

a: Rotational profile

b: Effects of instrumental and rotational broadening

Figure 3.11: The rotational profile of Eq. 3.31 for $\beta = 0.6$ (dashed), $\beta = 0.3$ (solid) and $\beta = 0$ (dotted). The effects of instrumental and rotational broadening are illustrated in the right panel: The dotted line is a synthetic spectrum which includes all microscopic broadening mechanisms. The solid line also accounts for instrumental blurring with resolution power $\lambda/\Delta\lambda = 15\,000$ whereas the colored lines are additionally broadened by rotation (red: $v_{\rm rot} \sin i = 100\,{\rm km\,s^{-1}}$, green: $v_{\rm rot} \sin i = 200\,{\rm km\,s^{-1}}$, blue: $v_{\rm rot} \sin i = 300\,{\rm km\,s^{-1}}$). The blending and smearing out of lines is nicely demonstrated.

wavelength interval $\Delta\lambda$, the instrumental profile can be directly applied to the normalized synthetic flux, otherwise the un-normalized flux and the continuum have to be treated separately.

Note that in contrast to the microscopic broadening mechanisms, rotational and instrumental broadening alter just the shape and not the equivalent width (EW) of a spectral line, whereby EW is defined to be the width of a rectangle of height 1 that encloses the same area between the normalized flux and the line of value unity (see Fig. 3.10b). This property is due to the fact that convolutions with functions of unit area preserve the area under the initial function[1].

3.4 Deriving Spectroscopic Parameters

Spectroscopic parameters are derived by matching models to observation. A very practical tool to do so is the *Spectrum Plotting and Analysis Suite* (SPAS) developed by Heiko A. Hirsch[2]. Based on a χ^2 downhill simplex algorithm, it allows synthetic spectra to be fitted to observed ones on an objective basis. A necessary input for SPAS is a grid of model spectra in the parameter space that defines the atmosphere. However, as there exist so many degrees of freedom ($T_{\rm eff}$, g, $\{X_Z\}$, ξ, $v_{\rm rot} \sin i$), it is far too complicated to construct a complete grid in the whole multi-dimensional parameter space. Hence the problem is split up and solved iteratively.

An initial guess for the effective temperature can be made by visual inspection of the observed spectrum in combination with Fig. 2.1. Moreover, a rough estimate for the surface gravity in hot stellar objects can be deduced from the wings of hydrogen lines since these are very sensitive to pressure by means of the linear Stark

[1] Strictly speaking, the invariance of the EW to rotational and instrumental broadening is valid only when the continuum does not vary much over an sufficiently large wavelength interval so that $EW = \int_{\lambda_0-\Delta}^{\lambda_0+\Delta}(1 - F_\lambda^{\rm norm}){\rm d}\lambda \approx 2\Delta - (\int_{\lambda_0-\Delta}^{\lambda_0+\Delta} F_\lambda {\rm d}\lambda)/F_\lambda^{\rm cont}$. The latter term is not changed when convolving F_λ with the normalized profiles of rotation or of the instrument, respectively.

[2] http://www.sternwarte.uni-erlangen.de/~hirsch/index.html

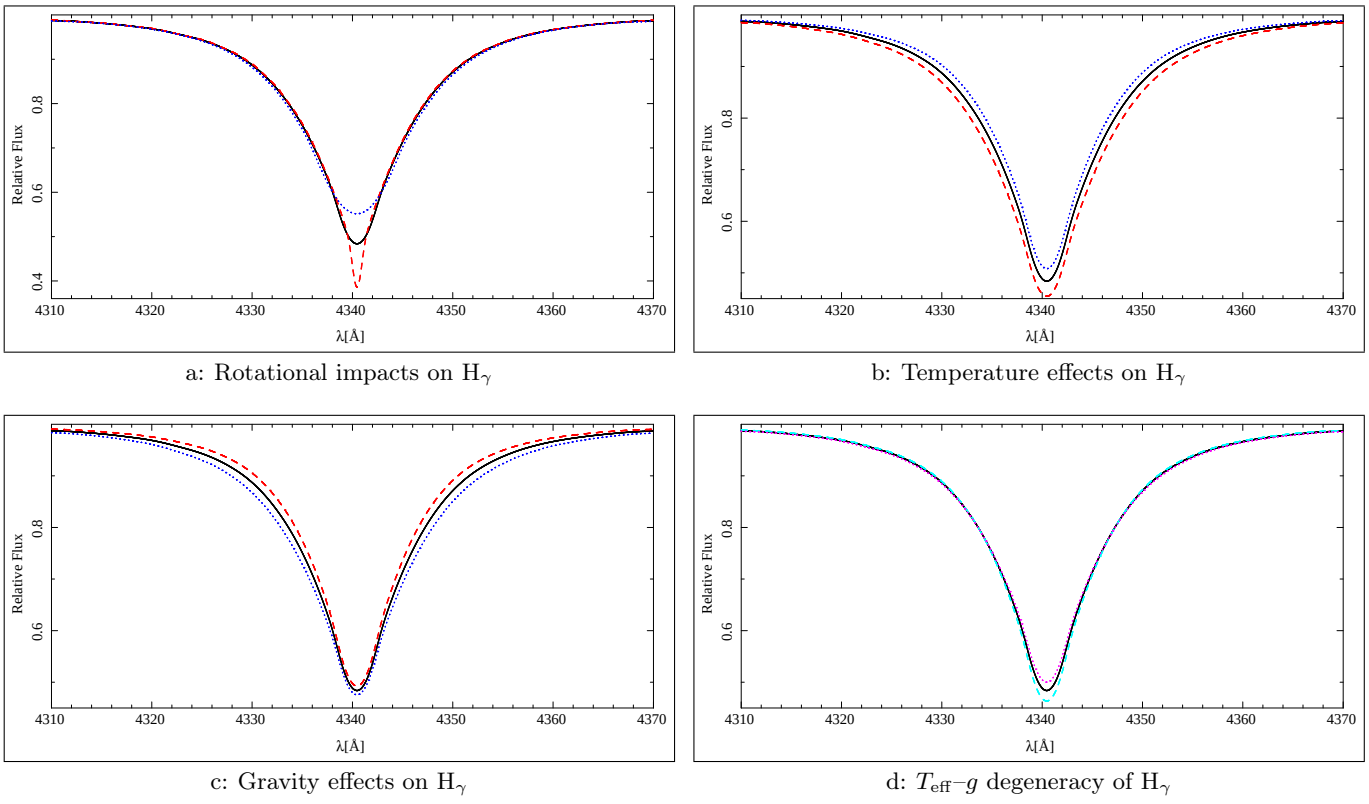

a: Rotational impacts on H_γ

b: Temperature effects on H_γ

c: Gravity effects on H_γ

d: $T_{\rm eff}$–g degeneracy of H_γ

Figure 3.12: Rotational, temperature and gravity effects on hydrogen lines: blue dotted/red dashed lines indicate an increase/decrease of rotational velocity ($\Delta v_{\rm rot} \sin i = \pm 150\,{\rm km\,s^{-1}}$), temperature ($\Delta T_{\rm eff} = \pm 1500\,{\rm K}$) and gravity ($\Delta \log(g\,[{\rm cm\,s^{-2}}]) = \pm 0.2$) with respect to the solid black reference curve ($\log(g\,[{\rm cm\,s^{-2}}]) = 4.10$, $T_{\rm eff} = 16\,500\,{\rm K}$, $v_{\rm rot} \sin i = 150\,{\rm km\,s^{-1}}$). The purple ($\log(g\,[{\rm cm\,s^{-2}}]) = 4.30$, $T_{\rm eff} = 18\,000\,{\rm K}$, $v_{\rm rot} \sin i = 150\,{\rm km\,s^{-1}}$) and cyan ($\log(g\,[{\rm cm\,s^{-2}}]) = 3.90$, $T_{\rm eff} = 15\,000\,{\rm K}$, $v_{\rm rot} \sin i = 150\,{\rm km\,s^{-1}}$) lines illustrate the $T_{\rm eff}$–g degeneracy of hydrogen wings.

effect. The values derived in this way are used to define the subspace in which the grid of model atmospheres has to be calculated. Typically, it is three-dimensional with variables $T_{\rm eff}$, g and ξ. The composition $\{X_Z\}$ is taken to be solar for the moment, an assumption which is empirically shown to be a good approximation for many stars. Once the grid is available, the first parameters to be constrained are effective temperature and surface gravity as they are most fundamental. Because the projected rotational velocity is not known so far, one has to focus on quantities that do not depend on $v_{\rm rot} \sin i$. In B-type stars, this is the case for the wings of hydrogen lines as these are so broad that even the convolution with rotational profiles of very fast rotators does not significantly affect their shape (see Fig. 3.12a). Unfortunately, hydrogen wings are kind of degenerate with respect to $T_{\rm eff}$–g pairs (see Fig. 3.12d): Changing the effective temperature alters the population number densities and thus the line strength according to Fig. 2.1. Increasing $T_{\rm eff}$ reduces the line strength and consequently narrows the wings (see Fig. 3.12b). However, this can be compensated to some extent by raising the surface gravity to enhance pressure induced broadening as mentioned in the previous section (see Fig. 3.12c). In this way, one obtains for each microturbulence an individual curve of possible values in the $T_{\rm eff}$–g plane. To fix the remaining free parameters, a second constraint is needed and usually given by a so-called ionization equilibrium. The fraction of atoms in a certain ionization stage is a function of temperature and surface gravity: A hotter environment implies higher particle velocities finally leading to more collisions capable to ionize atoms whereas a larger gravity results in a denser plasma enhancing the possibility of electron capture. Therefore, lines of the lower ionization stage are weak for high $T_{\rm eff}$ and small g and vice versa for the upper stage. Ionization equilibria commonly available in B-type stars are among others O I/O II, Fe II/Fe III and Si II/Si III/Si IV. As outlined before, a rotational invariant measure for the

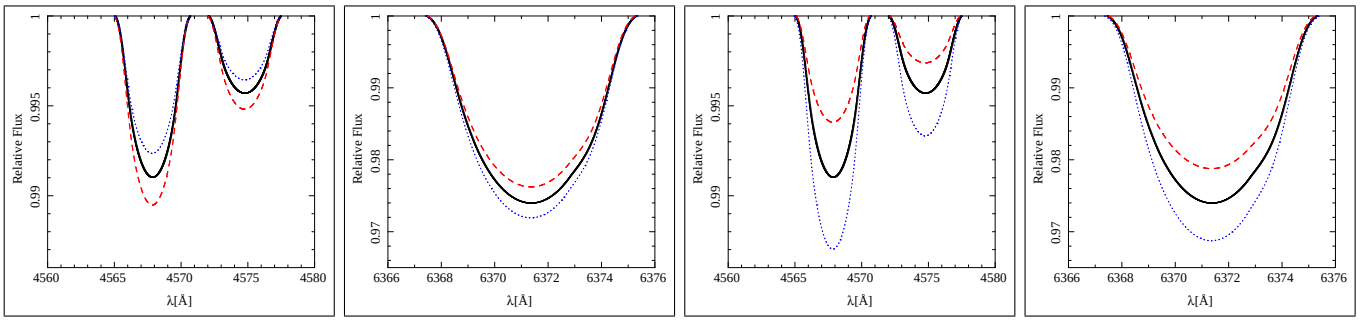

a: Gravity effects on Si III b: Gravity effects on Si II c: Abundance effects on Si III d: Abundance effects on Si II

Figure 3.13: Gravity and abundance effects on the silicon ionization equilibrium: blue dotted/red dashed lines indicate an increase/decrease of gravity or silicon abundance with respect to the solid black reference curve. Changes in abundance act in the same way on Si II and Si III while gravity yields opposing results.

strength of lines is the equivalent width of metal lines since these are generally narrow hence providing the necessary constant continuum behavior. In contrast to hydrogen lines, the EWs of some metal lines are very sensitive[1] to microturbulence and to the abundance[2] of the respective element. So the task is to choose the abundance X and surface gravity g for fixed ξ and varying $T_{\rm eff}$ in such a way that the EWs of lines of both ionization stages are reproduced. Since the impact of ξ on the equivalent width depends on the line strength itself (see below), it is advisable to restrict this step to lines of similar equivalent width $EW_{\rm IE}$. The use of more than one ionization stage is required to avoid an X–g degeneracy similar to the $T_{\rm eff}$–g degeneracy for hydrogen. This is due to the fact that the abundance affects the line strengths of both stages of ionization in the same manner while g acts contrary on the two stages (see Fig. 3.13). The result of this procedure is one extra curve in the $T_{\rm eff}$–g plane for each microturbulence whereby all points are additionally labeled by the corresponding abundance of the metal. The intersection of "hydrogen" and "ionization" curve gives values for $T_{\rm eff}$, g and metal abundance X as function of ξ (see Fig. 3.14a). So the next step is to determine the microturbulence.

In a simplified picture – neglecting the curve of growth – the broadening of metal lines is dominated by microscopic Doppler instead of natural or pressure broadening. When the Doppler broadening by non-thermal motions exceeds the thermal component, meaning $\xi > v_0 = \sqrt{2kT/m}$, the line broadening and consequently a considerable part of the equivalent width is mainly influenced by ξ. Recalling that absorption lines result from looking into layers with different temperatures (see Fig. 3.9b) – the larger the absorption line the lower the temperature of the emitting layer – it is evident that the stronger lines are more sensitive to ξ than the weaker ones. This implies that values for the microturbulence above/below the actual one will give higher/lower EWs than measured with the discrepancy becoming bigger with growing deviations from $EW_{\rm IE}$. The microturbulence is therefore determined by requiring that all equivalent widths of the ionization equilibrium metal are reproduced simultaneously and no systematic shifts occur (see Fig. 3.14b).

The next step is to deduce the projected rotational velocity. This is a simple task since the abundance of the ionization equilibrium metal is already known. Hence there is only $v_{\rm rot} \sin i$ left as free parameter when trying to fit the shape of its spectral lines. Having gained the rotational velocity, the same method can in turn be used to constrain the abundances of the remaining elements. In contrast to the ionization equilibrium metal, where synthetic models with varying abundances have to be calculated for a whole grid of atmospheric parameters $T_{\rm eff}$, g and ξ, the latter are fixed now reducing the number of required additional model atmospheres to be computed to a minimum. Note that unknown abundances are always assumed to be solar implying that intermediate synthetic models are based on incorrect compositions and thus cannot

[1] The sensitivity depends on the curve of growth, for more information see Gray (2005).

[2] From now on, elemental abundances are given as fraction by number and not by weight as originally introduced in Sect. 2.3. To distinguish between them, the new notation is just X instead of X_Z whereby X is replaced by H, He, Li, ...

be entirely correct. What one can do is to repeat the whole procedure described before using the gained parameters as starting values. The iterations are continued until the outcomes do not differ significantly from each other.

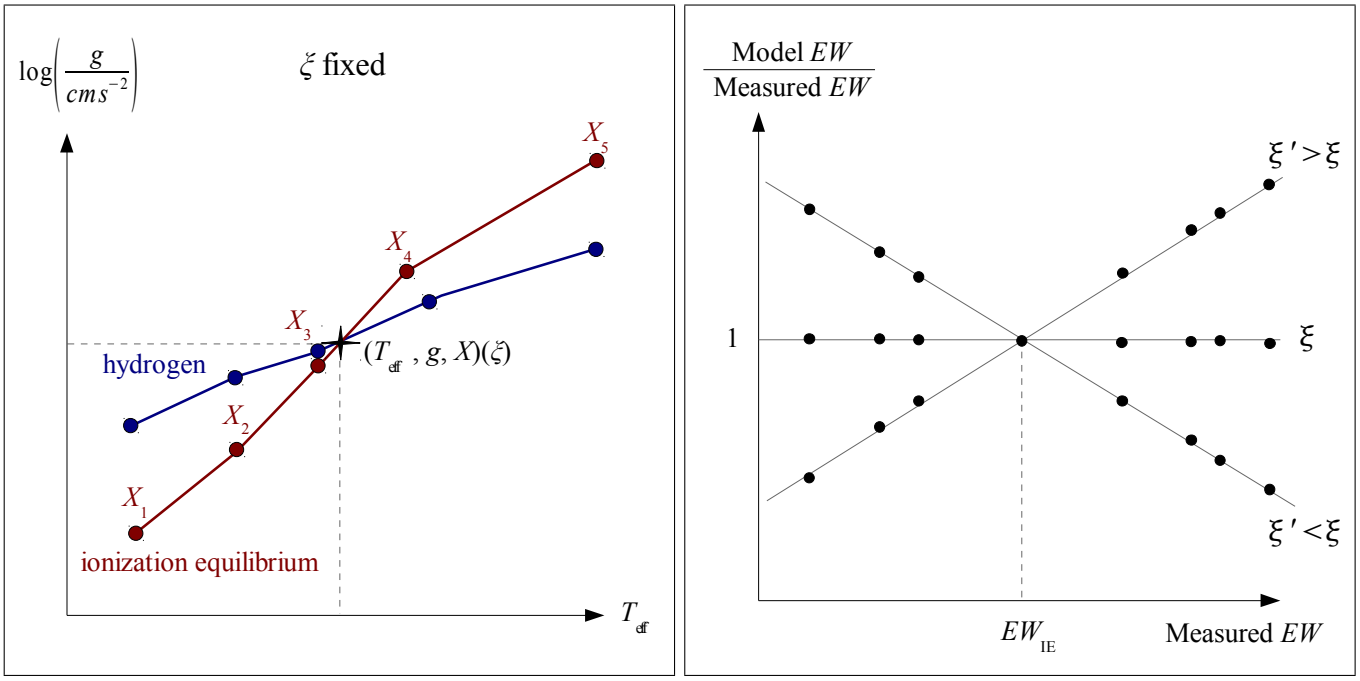

a: $T_{\rm eff}$–g determination

b: ξ determination

Figure 3.14: Determination of effective temperature, surface gravity and microturbulence by means of an ionization equilibrium: filled circles symbolize data points. $T_{\rm eff}$, g and metal abundance X as a function of ξ can be deduced from the intersection point of the degeneracy curves of hydrogen and ionization equilibrium metal. The microturbulence is fixed by demanding that all equivalent widths of the respective metal reproduce the observation. This is by construction the case for those in the vicinity of $EW_{\rm IE}$.

4 Quantitative Analysis of HIP 60350

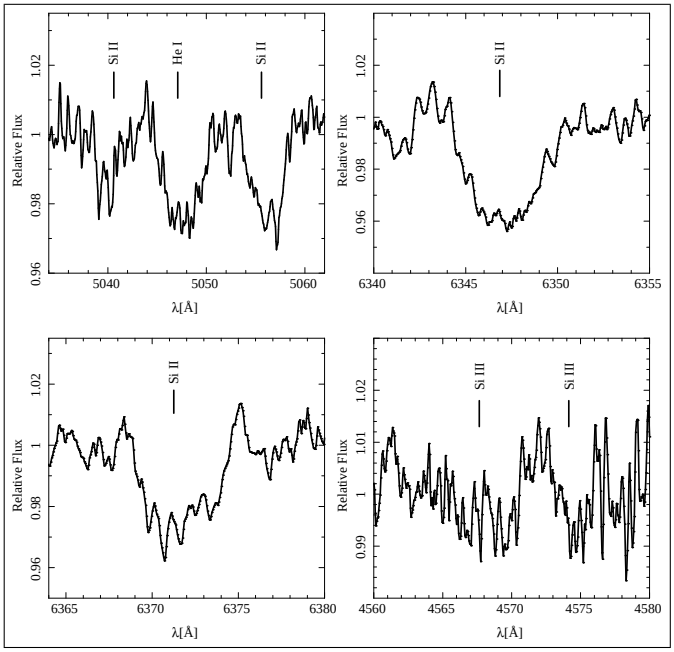

a: Si II/Si III ionization equilibrium

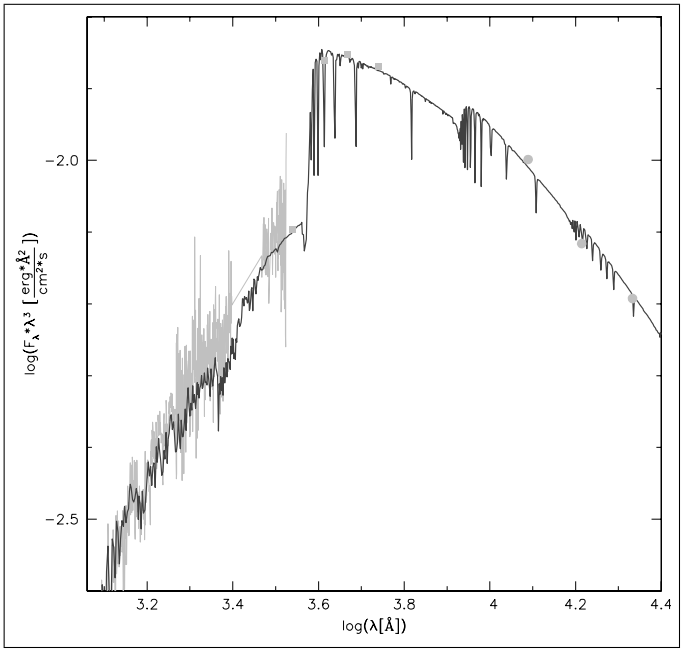

b: Spectral energy distribution

Figure 4.1: Si II/Si III ionization equilibrium and spectral energy distribution: The spectrum of HIP 60350 provides, apart from two tiny Si III lines, no access to an ionization equilibrium. Thus, a further indicator to constrain $T_{\rm eff}$ and g is necessary, viz. the spectral energy distribution represented by the gray line and filled circles/squares which are additionally overplotted by a synthetic flux distribution calculated from the ATLAS9 model for $T_{\rm eff} = 16\,100\,\mathrm{K}$ and $\log(g\,[\mathrm{cm\,s^{-2}}]) = 4.10$ (black line, see below).

The spectroscopic analysis of HIP 60350 was in principle carried out as described in the previous sections. However, some circumstances complicated the investigation and required special treatment. An ubiquitous problem during the entire analysis was a combination of three effects: Firstly, HIP 60350 lies in a temperature region where the optical spectrum shows very few strong but many weak metal lines. Secondly, a considerable fraction of the latter is smeared out due to the high projected rotational velocity, as demonstrated in Fig. 3.11b. Thirdly, the S/N ratio of the acquired spectrum is not sufficient to resolve most of the blurred spectral lines. In particular, the sole ionization equilibrium available – Si II/Si III – suffered extremely from these conditions as all Si III lines were too weak to be measurable except for the two tiny lines in Fig. 4.1a. It is evident that a further indicator was required to reliably constrain the two basic parameters $T_{\rm eff}$ and g, namely, the spectral energy distribution (SED) of Fig. 4.1b. As can be seen, it consists of three independent parts: I) ultra-violet spectrophotometry taken by the *International Ultraviolet Explorer*[1] (IUE, gray line), II) optical photometry (gray filled squares, Tobin, 1985) and III) infrared photometry (gray filled circles, Cutri et al., 2003). Those data can be compared to the predictions of model atmospheres to give constraints especially for the effective temperature. Note that the measurements have to be corrected for extinction, i.e., absorption of light due to interstellar matter between the star and Earth, which was done in Fig. 4.1b by making use of the extinction chart by Schlegel, Finkbeiner & Davis (1998). In general, the SED is merely used as a consistency check as its accuracy cannot keep up with that of the ionization equilibrium method.

In case of HIP 60350, ionization equilibrium and SED were weighted equally to constrain $T_{\rm eff}$. Because the former tended to lower, the latter to higher temperatures, a compromise with intermediate $T_{\rm eff} = 16\,100 \pm 500\,\mathrm{K}$ had to be made to match both indicators satisfactorily. The wings of the hydrogen lines as well as the

[1] http://archive.stsci.edu/iue/

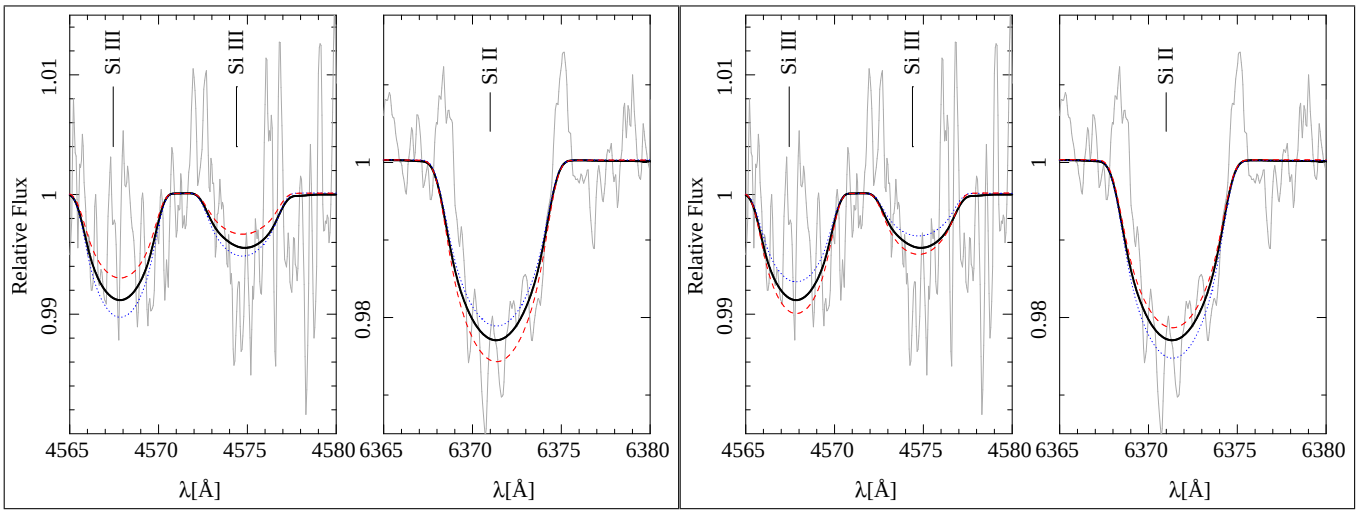

a: Effective temperature b: Surface gravity

Figure 4.2: Visual estimation of uncertainty in effective temperature and surface gravity by means of the ionization equilibrium of Si II/Si III: blue dotted/red dashed lines indicate an increase/decrease either of temperature ($\Delta T_{\mathrm{eff}} = \pm 500\,\mathrm{K}$) or pressure ($\Delta \log(g\,[\mathrm{cm\,s^{-2}}]) = \pm 0.15$) with respect to the best fit (black solid line) of the observation (gray solid line) and visually confirm the error bars of Table 4.1.

Si II/Si III equilibrium were then reproduced pretty well by a surface gravity $\log(g\,[\mathrm{cm\,s^{-2}}]) = 4.10 \pm 0.15$ and a silicon abundance fraction by number $\mathrm{Si} = (3.4 \pm 1.6) \cdot 10^{-5}$. From the few Si II lines, a microturbulence of $\xi = 5 \pm 2\,\mathrm{km\,s^{-1}}$ and a rotational velocity of $v_{\mathrm{rot}} \sin i = 150 \pm 5\,\mathrm{km\,s^{-1}}$ was derived. These data together with the abundances of those metals, for which lines were visible and hence could be analyzed, are summarized in Table 4.1. The abundances of all other elements were assumed to be solar. Estimating the uncertainties of the parameters is an extremely nontrivial task as so many quantities are correlated with each other. Moreover, a thorough error analysis would tremendously increase the effort it takes to analyze one single star as changing an atmospheric parameter involves to calculate new model grids and to determine abundances again and again. In order to simplify this procedure, one assumes the parameters to be independent hence leading on the one hand to an overestimation of errors but on the other hand to an huge saving of time. Another important problem lies with the continuum determination as that it is responsible for a great deal of uncertainty and, what is more, it is strongly influenced by the person performing the investigation. In particular, spectra with low S/N ratio and weak lines are affected by this issue as there are several reasonable possibilities to place the continuous flux. Moreover, some weak lines in these spectra could be misinterpreted as continuum in the normalization process of data reduction and thus accidentally erased (see Fig. 4.6). The spectroscopic uncertainties given in this work are primarily based on visual inspection, i.e., atmospheric parameters visually reproduce the observations when being altered within their error margins and all other quantities held fixed (see Figs. 4.2 and 4.3).

The excellent agreement of final SURFACE spectrum with HET observation is illustrated for strategic regions in Figs. 4.5, 4.6 and 4.7 whereas the good match of the corresponding final ATLAS9 model flux distribution with the observed SED can be seen in Fig. 4.1b. The reason for choosing the spectral energy distribution of ATLAS instead of DETAIL or SURFACE is that the latter are optimized for the visual range but lack some minor features that influence other parts of the electromagnetic spectrum.

The information gathered so far can be used to derive two additional highly important quantities, namely, the stellar mass $M_\star$ and evolution time T_{evo}. As was illustrated in sections 2.3 and 2.4, it is possible to compute evolution tracks of stars with given initial conditions. By comparing the time dependent properties of the model star to those deduced from spectroscopy, one is able to constrain $M_\star$ and T_{evo}. For this work, evolution tracks of solar metalicity by Schaller et al. (1992) are applied. Newer ones exist (Maeder & Meynet, 2005),

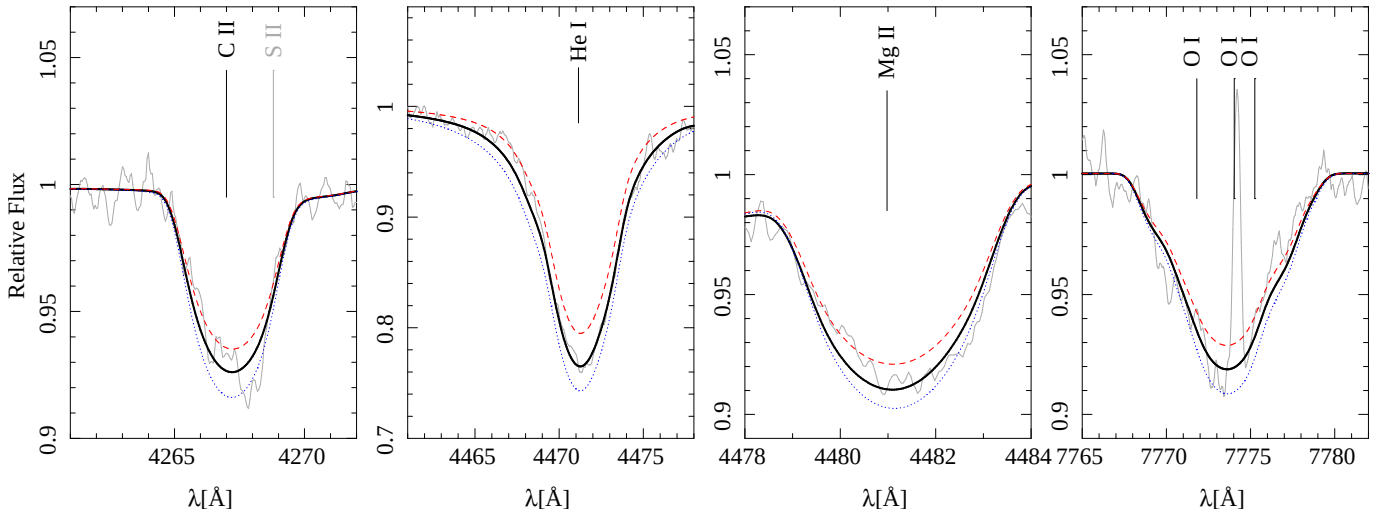

Figure 4.3: Visual estimation of abundance uncertainties demonstrated in the cases of carbon, helium, magnesium and oxygen: the observation (gray solid line) is reproduced best by the parameters of Table 4.1 (black line). The corresponding errors are deduced visually by varying the abundance of an individual chemical species while keeping all others fixed. Blue dotted/red dashed lines stand for an increase/decrease of abundance according to Table 4.1.

which also include, e.g., rotation-induced mixing that affects stellar lifetimes, but are unfortunately not available in the necessary parameter region. The mass and age of HIP 60350 is obtained from the $T_{\rm eff}$–$\log g$ diagram in Fig. 4.4 to be $M_\star = 4.9 \pm 0.2\,M_\odot$ and $T_{\rm evol} = 45^{+15}_{-30}$ Myr.

By means of the relation $g = GM_\star R_\star^{-2}$ introduced in Eq. 3.7, the stellar radius is given by $R_\star = 2.8 \pm 0.2\,R_\odot$. Use of Eq. 2.5 yields $\log(L/L_\odot) = 3.3 \pm 0.6$.

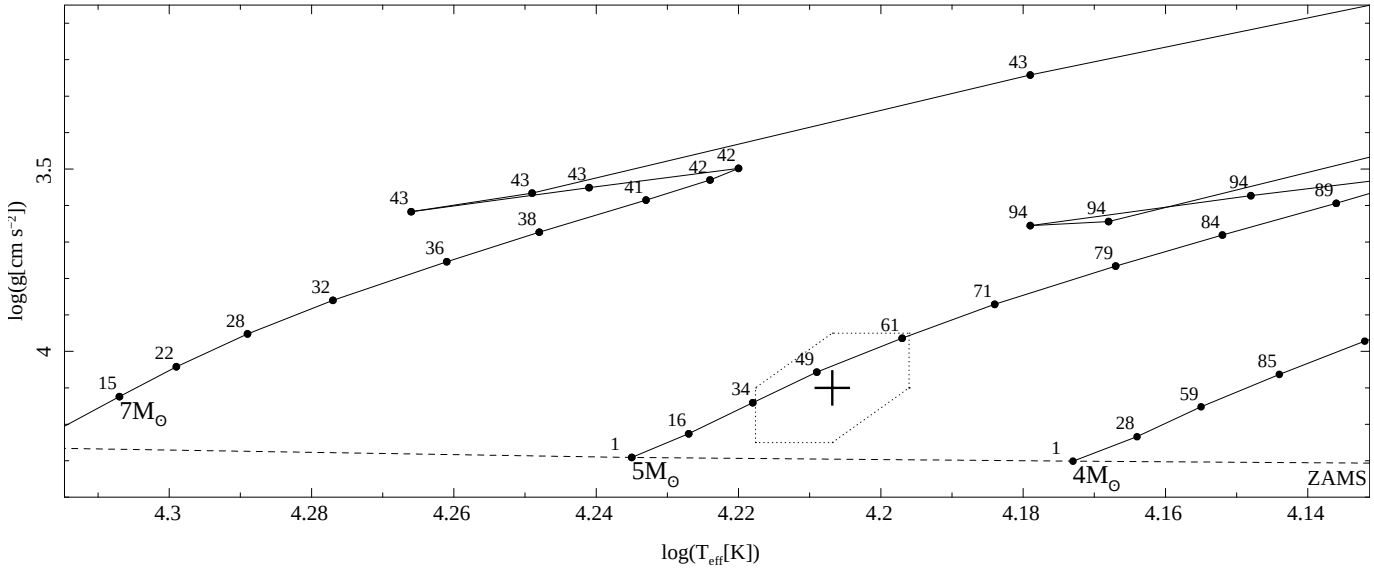

Figure 4.4: Position of HIP 60350 in a $T_{\rm eff}$–$\log g$ diagram with evolution tracks calculated by Schaller et al. (1992). Time steps are marked by filled circles giving the age in Myr. Uncertainties are indicated by the dotted hexagon. The locus of the zero-age main sequence is displayed as well.

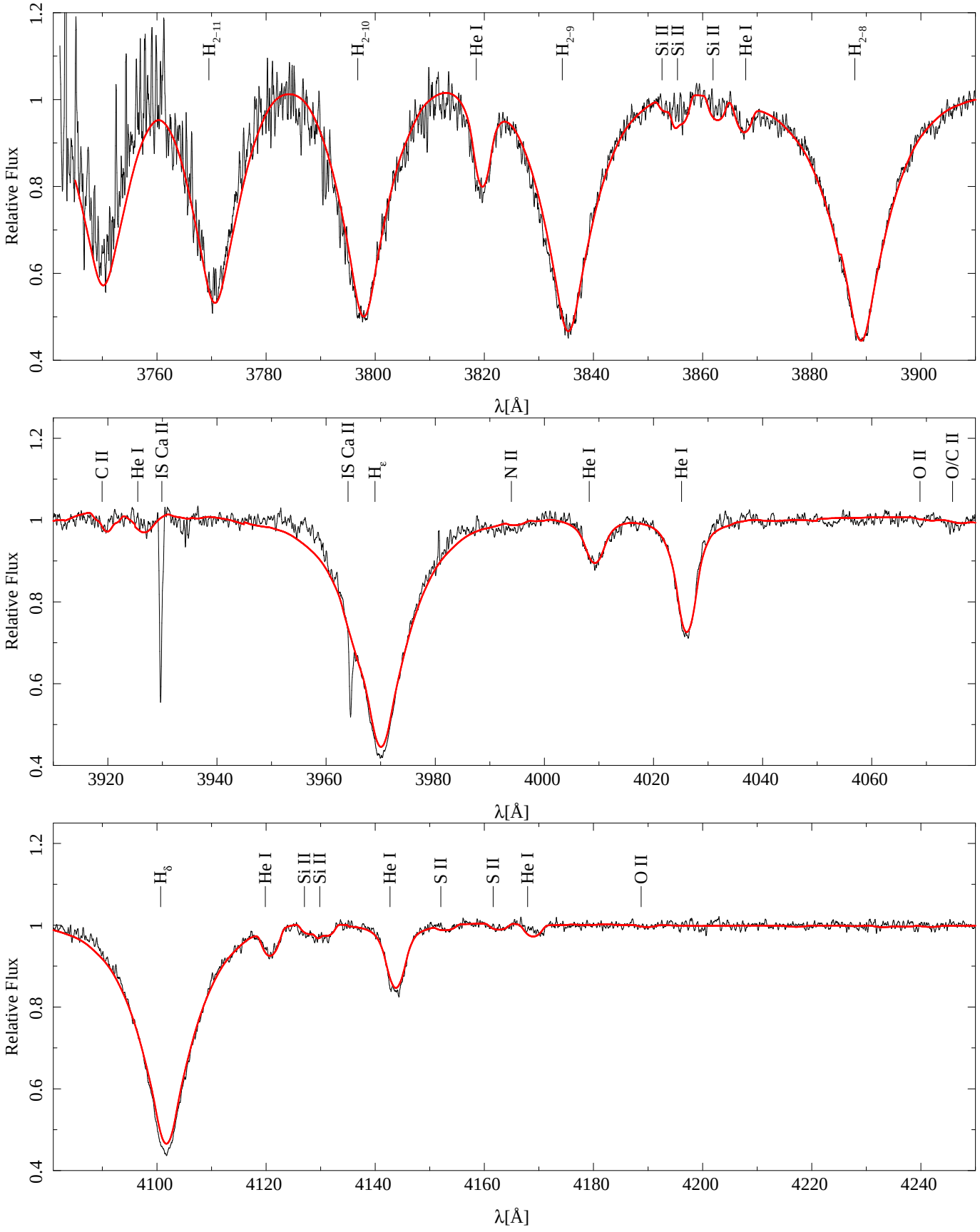

Figure 4.5: Comparison of observation (black) with final synthetic spectrum (red): the increasing discrepancy with decreasing wavelength ($\lambda < 3900$Å) is owed to a drop in signal strength and thus in the signal-to-noise ratio excluding this part from any meaningful investigation. Sharp interstellar absorption Ca II lines are given the prefix "IS". The asymmetric form of H_ε is certainly an artifact of data reduction and by no means authentic.

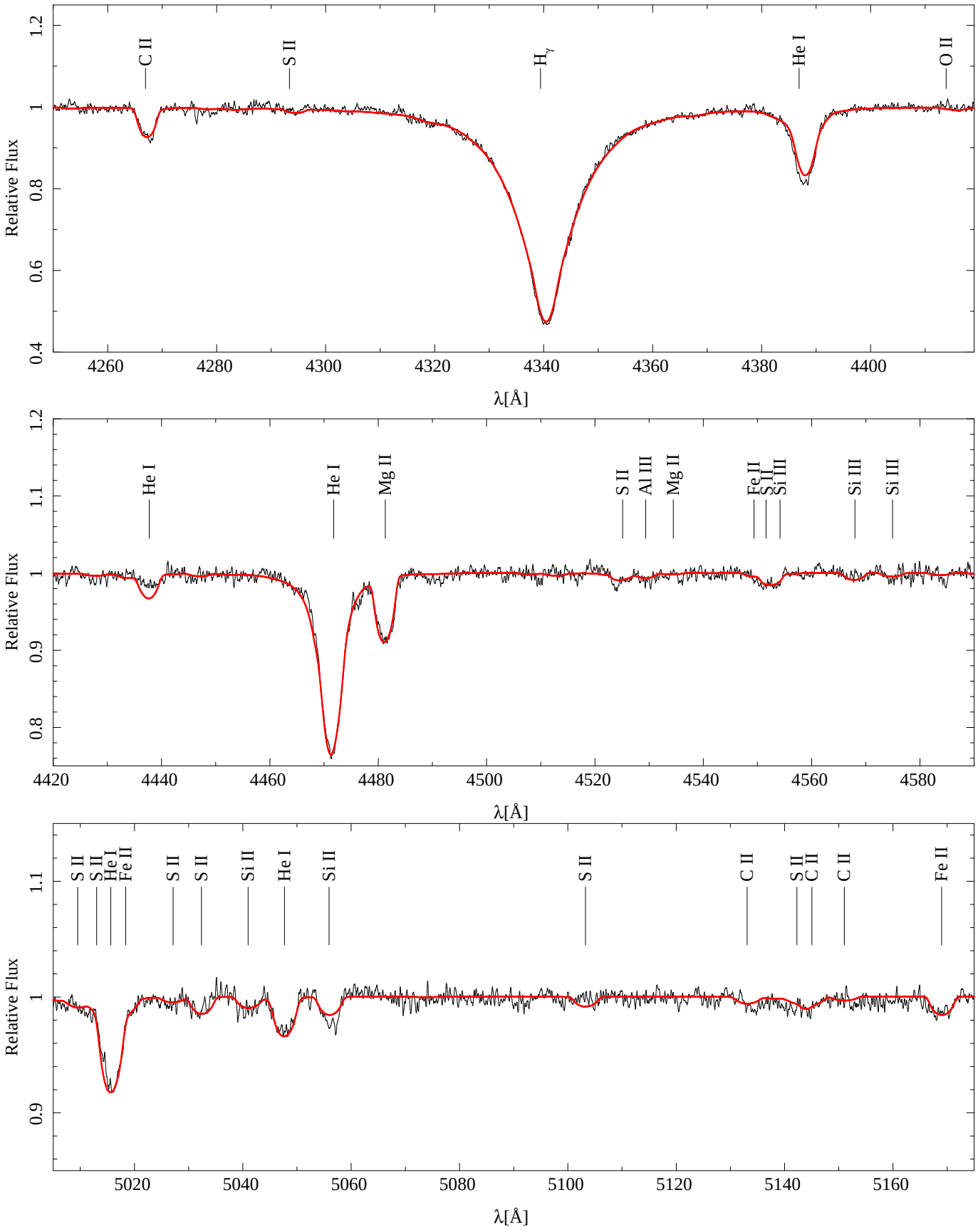

Figure 4.6: Comparison of observation (black) with final synthetic spectrum (red): the mismatch of He I λ4438 is a result of a data reduction error, as proven by its good match in the TWIN spectrum.

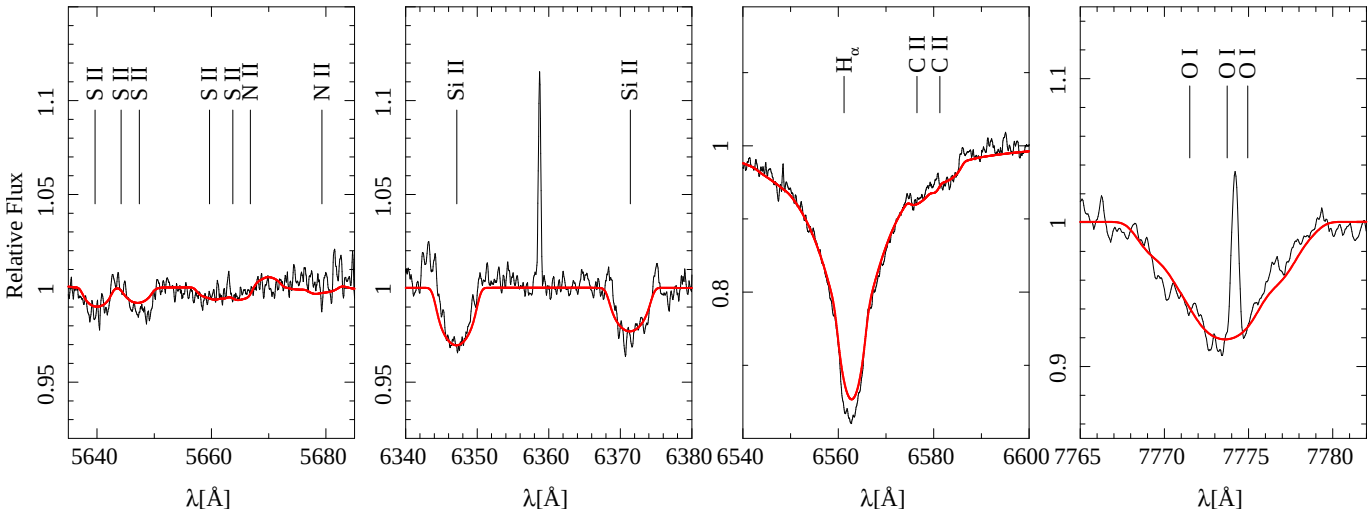

Figure 4.7: Comparison of observation (black) with final synthetic spectrum (red) for some selected lines. The narrow peaks (λ6359, λ7774) are consequence of insufficient subtraction of skylines.

The last quantity that can be directly measured from the observed spectra is the radial velocity of the star. Due to this line-of-sight velocity v, a corresponding Doppler shift $\Delta\lambda$ in wavelength occurs:

$$\frac{\Delta\lambda}{\lambda} = \frac{v}{c} \tag{4.1}$$

Note that v includes the radial velocity of the Earth around the Sun which can reach values up to $\pm 30\,\mathrm{km\,s^{-1}}$ depending on the season and the position of the star on the celestial sphere. To get rid of this unwanted effect, one usually applies a barycentric correction, meaning that one calculates the relative velocity with respect to the solar system's center of mass. Radial velocities v_{rad} given in this work are barycentric. The determination of v_{rad} is carried out by fitting Gauss-Lorentz functions to unblended spectral lines yielding the central wavelength of the line. The deviation $\Delta\lambda$ from the theoretical or laboratory value λ gives the radial velocity via Eq. 4.1. Assigning v_{rad} to an observed spectrum is typically one of the first steps of an analysis since co-adding spectra for improving the S/N is only feasible after a radial correction has been performed. The available TWIN and HET spectra mutually give $v_{\mathrm{rad}} = +262 \pm 5\,\mathrm{km\,s^{-1}}$. Bearing in mind the different time intervals between each measurement, the star is unlikely a binary unless seen pole on.

Table 4.1: Stellar parameters and elemental abundances of HIP 60350: Abundances are given as fraction by number in a linear as well as logarithmic scale (with respect to hydrogen), the latter being commonly used in astronomy. Uncertainties were primarily estimated by visual inspection.

Parameter	Value	Element	X	log(X/H) + 12
T_{eff} [K]	$16\,100 \pm 500$	He	0.140 ± 0.05	11.21 ± 0.18
$\log(g\,[\mathrm{cm\,s^{-2}}])$	4.10 ± 0.15	C	$(4.8 \pm 2.2) \cdot 10^{-4}$	8.75 ± 0.20
$\xi\,[\mathrm{km\,s^{-1}}]$	5 ± 2	N	$(1.1 \pm 0.8) \cdot 10^{-4}$	8.10 ± 0.30
$v_{\mathrm{rot}} \sin i\,[\mathrm{km\,s^{-1}}]$	150 ± 5	O	$(7.2 \pm 2.5) \cdot 10^{-4}$	8.93 ± 0.15
$v_{\mathrm{rad}}\,[\mathrm{km\,s^{-1}}]$	262 ± 5	Mg	$(2.1 \pm 1.0) \cdot 10^{-5}$	7.38 ± 0.20
T_{evo} [Myr]	45^{+15}_{-30}	Si	$(3.4 \pm 1.6) \cdot 10^{-5}$	7.62 ± 0.20
$M_\star/M_\odot$	4.9 ± 0.2	S	$(1.4 \pm 0.9) \cdot 10^{-5}$	7.23 ± 0.25
$R_\star/R_\odot$	2.8 ± 0.2	Fe	$(1.3 \pm 0.7) \cdot 10^{-5}$	7.19 ± 0.25
$\log(L/L_\odot)$	3.3 ± 0.6			

5 Kinematics

The study of the kinematics of runaway stars can yield valuable information about their spatial origins and nature. An essential ingredient to perform such an investigation is detailed knowledge of the object's three-dimensional position and velocity components as well as a reliable model of the Galactic gravitational potential. Based on the preceding results, this chapter illustrates the finding of the full phase space information of HIP 60350 and outlines the subsequent orbit computations intended to gain some indications of possible ejection scenarios. The most crucial step to achieve this goal is to determine the distance to the star.

5.1 Distance determination

The proper definition of the visual magnitude V, which was already mentioned in Sect. 2.1, reads:

$$V = -2.5 \log \left(\frac{\int_0^\infty r_V(\lambda) f_\lambda \mathrm{d}\lambda}{\int_0^\infty r_V(\lambda) f_\lambda^{\mathrm{Vega}} \mathrm{d}\lambda} \right) \tag{5.1}$$

Here, f_λ denotes the stellar flux that is measured on Earth and r_V is the visual response function listed in Ažusienis & Straižys (1969) and plotted in Fig. 5.1a. The denominator $\int_0^\infty r_V(\lambda) f_\lambda^{\mathrm{Vega}} \mathrm{d}\lambda = \text{constant}$ ensures that the zero point of the visual magnitude scale is given by the standard star Vega, which has historical reasons. The accurately calibrated Vega flux $f_\lambda^{\mathrm{Vega}}$ can be found, e.g., in Tüg, White & Lockwood (1977) and is depicted in Fig. 5.1b. Neglecting for the moment the loss of photons due to absorption by interstellar matter, energy conservation implies that the amount of energy that passes through an imaginary sphere enclosing the star is constant. Assuming the stellar body to be spherically symmetric, this statement is equal to:

$$4\pi R_\star^2 F_\lambda = 4\pi d^2 f_\lambda \quad \Rightarrow \quad f_\lambda = \frac{R_\star^2}{d^2} F_\lambda \tag{5.2}$$

$R_\star$ is the stellar radius, F_λ the flux emanating from the star's surface and d the distance to the object. Once again making use of the formula $g = G M_\star R_\star^{-2}$, this leads to:

$$f_\lambda = \frac{G M_\star}{g d^2} F_\lambda \tag{5.3}$$

Inserting Eq. 5.3 in 5.1 yields:

$$d = d(g, M_\star, F_\lambda, V) = \sqrt{\frac{G M_\star \int_0^\infty r_V(\lambda) F_\lambda \mathrm{d}\lambda}{g \int_0^\infty r_V(\lambda) f_\lambda^{\mathrm{Vega}} \mathrm{d}\lambda} 10^{0.4V}} \tag{5.4}$$

Interstellar extinction reduces the observed flux and is formally corrected by substituting $V \rightarrow V - A_V$ in Eq. 5.4:

$$d = d(g, M_\star, F_\lambda, V - A_V) = \sqrt{\frac{G M_\star \int_0^\infty r_V(\lambda) F_\lambda \mathrm{d}\lambda}{g \int_0^\infty r_V(\lambda) f_\lambda^{\mathrm{Vega}} \mathrm{d}\lambda} 10^{0.4(V - A_V)}} \tag{5.5}$$

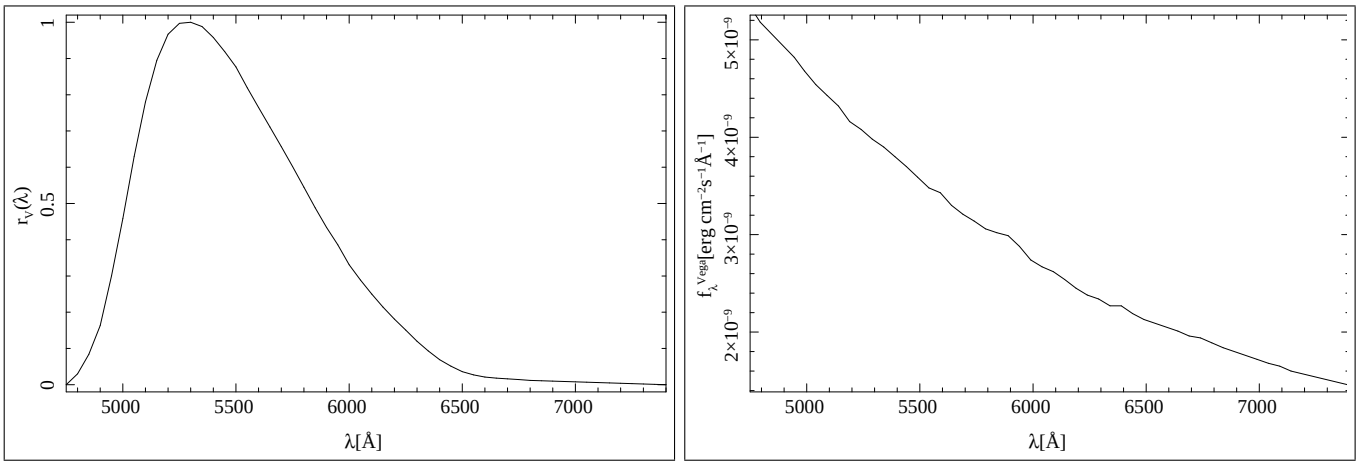

a: Visual response function b: Calibrated Vega flux

Figure 5.1: The visual response function r_V and the calibrated Vega flux $f_\lambda^{\mathrm{Vega}}$ are used to define the visual magnitude V of a star by means of Eq. 5.1.

According to Schlegel, Finkbeiner & Davis (1998), the reddening A_V can be expressed by $A_V = 3.1\,E(B-V)$ with $E(B-V)$ being the color excess depending on the position on the celestial sphere. The extinction charts by Schlegel, Finkbeiner & Davis list numerical values as function of coordinates.

Error estimation is again a nontrivial task since g, $M_\star$ and F_λ are correlated. However, for the sake of simplicity they are assumed to be independent leading to an overestimate of uncertainty via the standard formula of error propagation:

$$\Delta d = \sqrt{\left(\frac{\partial d}{\partial g}\Delta g\right)^2 + \left(\frac{\partial d}{\partial M_\star}\Delta M_\star\right)^2 + \left(\frac{\partial d}{\partial \int_0^\infty r_V(\lambda)F_\lambda \mathrm{d}\lambda}\Delta\int_0^\infty r_V(\lambda)F_\lambda \mathrm{d}\lambda\right)^2 + \left(\frac{\partial d}{\partial(V-A_V)}\Delta(V-A_V)\right)^2} \tag{5.6}$$

To deduce $\Delta\int_0^\infty r_V(\lambda)F_\lambda \mathrm{d}\lambda$, the flux integral is numerically computed for four additional synthetic models with effective temperature $\tilde{T}_{\mathrm{eff}} = T_{\mathrm{eff}} \pm \Delta T_{\mathrm{eff}}$ and surface gravity $\log(\tilde{g}\,[\mathrm{cm\,s^{-2}}]) = \log(\mathrm{g}\,[\mathrm{cm\,s^{-2}}]) \pm \Delta\log(\mathrm{g}\,[\mathrm{cm\,s^{-2}}])$. The uncertainty in the integrated flux is then taken to be:

$$\Delta\int_0^\infty r_V(\lambda)F_\lambda \mathrm{d}\lambda = \text{maximum}\left\{\left|\int_0^\infty r_V(\lambda)F_\lambda(T_{\mathrm{eff}},g)\mathrm{d}\lambda - \int_0^\infty r_V(\lambda)F_\lambda(\tilde{T}_{\mathrm{eff}},\tilde{g})\mathrm{d}\lambda\right|\right\} \tag{5.7}$$

Using the values for g and $M_\star$ from Table 4.1, $V = 11.60 \pm 0.01$ mag (Tobin, 1985), $E(B-V) = 0.023$ mag (Schlegel, Finkbeiner & Davis, 1998) and the flux integral from model atmospheres, Eqs. 5.5 and 5.6 yield a distance to HIP 60350 of $d = 3.1 \pm 0.6$ kpc.

5.2 Orbit calculation

The (almost) constant rotation axis of the Earth provides a quite natural coordinate system for astronomers, namely, equatorial coordinates given by right ascension α and declination δ using the celestial equator as plane of reference. Right ascension is measured along the celestial equator from the vernal equinox point, i.e., the fixed direction defined by the intersection of the celestial equator plane with the ecliptic occurring in spring, to the object in east direction. Declination is measured from 0° to ±90° between celestial equator

and the north/south celestial pole. Tangential velocities are given by proper motions μ_α and μ_δ, which are the angular velocities in α and δ, via $v_\alpha = d\cos(\delta)\,\mu_\alpha$ and $v_\delta = d\mu_\delta$. Gaining proper motions is hence the final step to obtain the full six-dimensional phase space information. Fortunately, HIP 60350 was among the $\sim 120\,000$ targets that were observed by the *Hipparcos Space Astrometry Mission*[1] measuring proper motions with unprecedented accuracy. According to its latest reduction (van Leeuwen, 2007), these are given by $\mu_\alpha \cos(\delta) = -13.51 \pm 1.31$ milli-arcseconds per year and $\mu_\delta = 16.34 \pm 1.37$ milli-arcseconds per year. Moreover, the Vizier database[2] (Ochsenbein, Bauer & Marcout, 2000) lists five ground-based measurements that excellently confirm the Hipparcos values.

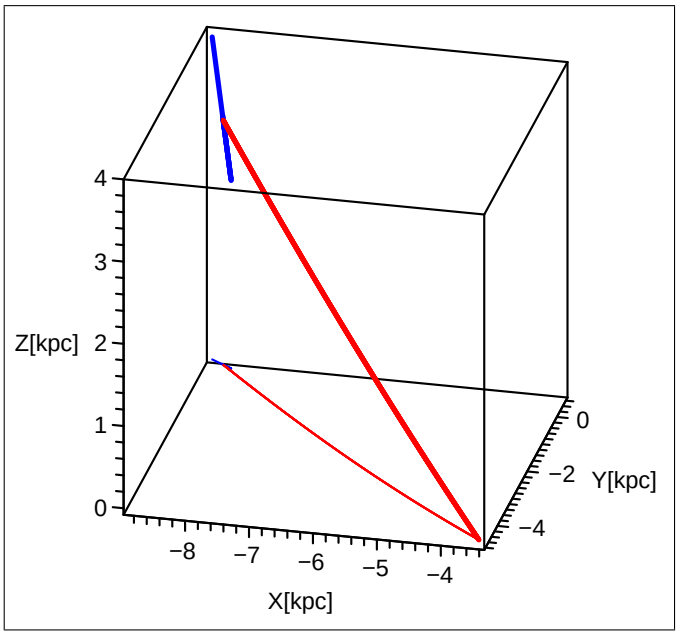

Figure 5.2: Current position (blue) and exemplary orbit of HIP 60350 (red): For better orientation, the projections onto the $X-Y$ plane are displayed as well.

Once 3D coordinates and velocities were available, the orbit of the investigated star was numerically traced back to the Galactic disk using the code of Odenkirchen & Brosche (1992) and the Galactic potential of Allen & Santillan (1991). The latter as well as the coordinate system used in the calculations were explained in Sect. 2.6. Due to the numerical solution of the problem, an analytical error estimation is impossible. Uncertainties were therefore constrained via a Monte Carlo method[3] that simultaneously and independently varied the six components[4] of position and velocity, assuming for each a Gaussian distribution. The following results are average or median values of a sample of 50 000 trajectories. Uncertainties are expressed by the standard deviation.

Figure 5.2 shows a typical trajectory and the locus of possible current positions of HIP 60350. The latter is solely influenced by the uncertainty in distance d to the object and accordingly a straight line. The statistics of the sample of orbits gives $X = -8.7 \pm 0.1$ kpc, $Y = 0.5 \pm 0.1$ kpc and $Z = 3.0 \pm 0.4$ kpc placing the star in the Milky Way's inner halo. Due to the large Galactic rest frame velocity of $v_{\rm grf} = \sqrt{{v_X}^2 + {v_Y}^2 + {v_Z}^2} \approx 530 \pm 36\,{\rm km\,s^{-1}}$ (see Fig. 5.3a), the orbit itself is also almost linear because the deceleration by the Galactic potential is weak under these circumstances. This space velocity can be compared to the local Galactic escape velocity $v_{\rm esc}(X,Y,Z)$, separating bound from unbound states and deduced from the condition of vanishing total energy $E = E_{\rm kin} + E_{\rm pot}$:

$$E_{\rm kin} + E_{\rm pot} = \frac{1}{2} M_\star v_{\rm esc}^2 - \Phi(X,Y,Z) M_\star \stackrel{!}{=} 0 \quad \Rightarrow \quad v_{\rm esc}(X,Y,Z) = \sqrt{-2\Phi(X,Y,Z)} \tag{5.8}$$

The distribution of $v_{\rm grf} - v_{\rm esc}$ over the sample of orbits is displayed in Fig. 5.3b and reveals that more than half of the trajectories calculated for HIP 60350 are indeed unbound (median value of $v_{\rm grf} - v_{\rm esc}$ is $5\,{\rm km\,s^{-1}}$). Because the Galactic center can be excluded as the star's possible birthplace ($R_{\rm int} = 6.1 \pm 0.6$ kpc), HIP 60350 does not qualify as a hyper-velocity star but is rather a promising hyper-runaway candidate. A further point supporting the runaway scenario is the fact that the average travel time $T_{\rm flight} = 14.3 \pm 2.5$ Myr (see Fig. 5.3c) lies at the very lower end of $T_{\rm evo} = 45^{+15}_{-30}$ Myr – a necessary condition for all runaway objects. A quantity being extremely helpful in this context is the ejection velocity $v_{\rm ej}$, which is the space velocity at disk intersection relative to the rotating Galactic rest frame and thus to the center of mass of the runaway star's home system. Its distribution is depicted in Fig. 5.3d giving an average value of $v_{\rm ej} = 389 \pm 43\,{\rm km\,s^{-1}}$. As explained in the next chapter, the ejection velocity can be used to put strong constraints on possible progenitor systems when considering the ejection by a supernova explosion in a binary system.

[1] http://www.rssd.esa.int/index.php?project=HIPPARCOS
[2] http://vizier.u-strasbg.fr/viz-bin/VizieR
[3] implemented by Eva-Maria Pauli
[4] In fact, only four parameters were altered as uncertainties in α and δ are negligible.

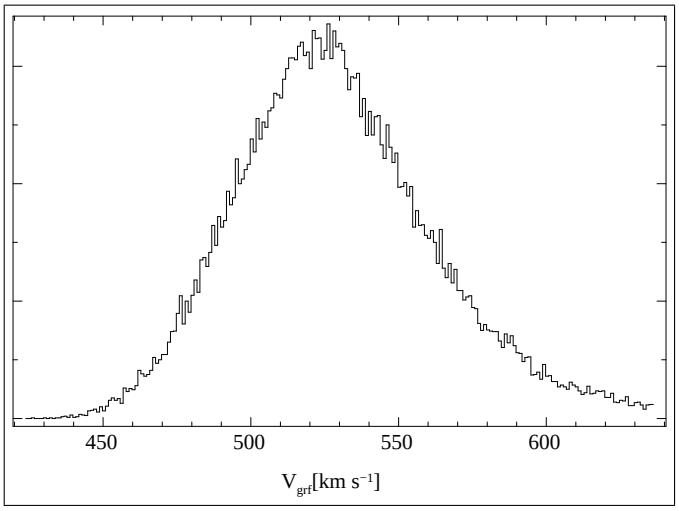

a: Absolute current space velocity

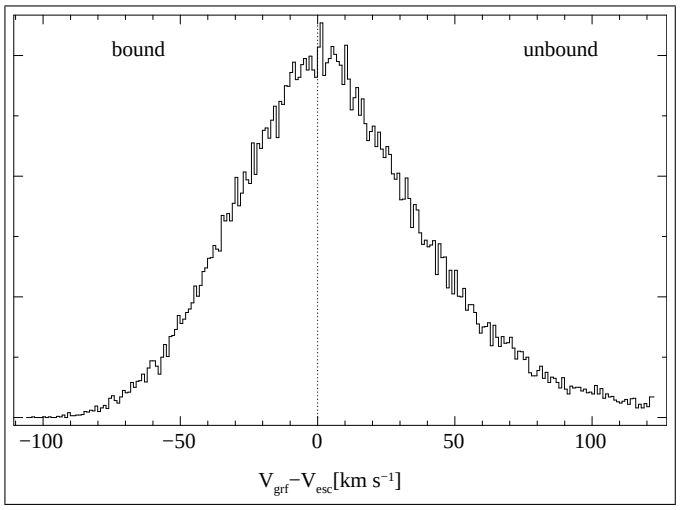

b: Distribution of bound/unbound orbits

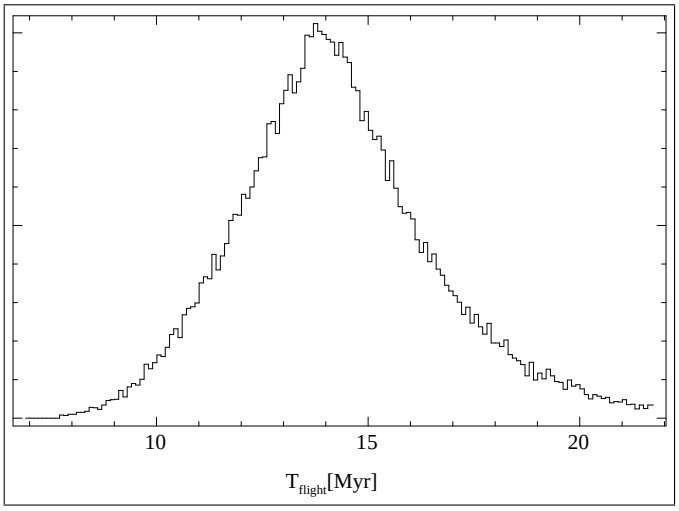

c: Time of flight

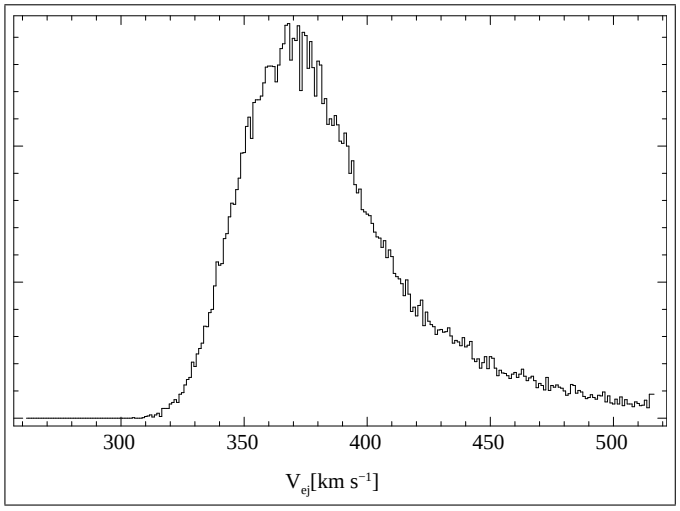

d: Absolute ejection velocity

Figure 5.3: Distribution of current space velocity, bound orbits, travel times and ejection velocities in a sample of 50 000 trajectories computed for HIP 60350.

Table 5.1: Results of the kinematic study of HIP 60350 derived from Monte Carlo simulations of 50 000 independent orbit calculations: Quantities at the moment of disk intersection are given the additional subscript "int" to distinguish them from current values.

Variable	Median	Average	Uncertainty	Variable	Median	Average	Uncertainty
X [kpc]	−8.7	−8.7	0.1	$X_{\rm int}$ [kpc]	−3.4	−3.2	1.6
Y [kpc]	0.5	0.5	0.1	$Y_{\rm int}$ [kpc]	−4.8	−4.9	1.0
Z [kpc]	3.0	3.0	0.4	$Z_{\rm int}$ [kpc]	0	0	0
R [kpc]	9.2	9.2	0.3	$R_{\rm int}$ [kpc]	6.0	6.1	0.6
v_X [km s^{-1}]	−324	−327	43	$v_{X\,\rm int}$ [km s^{-1}]	−401	−401	47
v_Y [km s^{-1}]	371	373	22	$v_{Y\,\rm int}$ [km s^{-1}]	335	335	16
v_Z [km s^{-1}]	182	182	13	$v_{Z\,\rm int}$ [km s^{-1}]	231	231	5
$v_{\rm grf}$ [km s^{-1}]	527	530	36	$v_{\rm grf\,int}$ [km s^{-1}]	572	572	33
$v_{\rm grf} - V_{\rm esc}$ [km s^{-1}]	5	8	39	$v_{\rm ej}$ [km s^{-1}]	379	389	43
$T_{\rm flight}$ [Myr]	14.1	14.3	2.5				

6 Dynamical Interaction versus Binary Supernova Scenario

The kinematic analysis in Chap. 5 undoubtedly points to a runaway history of HIP 60350 as this scenario is consistent with all observations while *in situ* star formation in the halo has serious problems, e.g., to explain the extraordinary large current space velocity $v_{\rm grf}$. In this chapter, the two most likely runaway ejection mechanisms – dynamical ejection or a supernova explosion in a binary system – will be discussed based on kinematic and spectroscopic criteria. As will be seen, both scenarios have their justifications and arguing for one of them depends on the interpretation of the derived abundance pattern shown in Fig. 6.1.

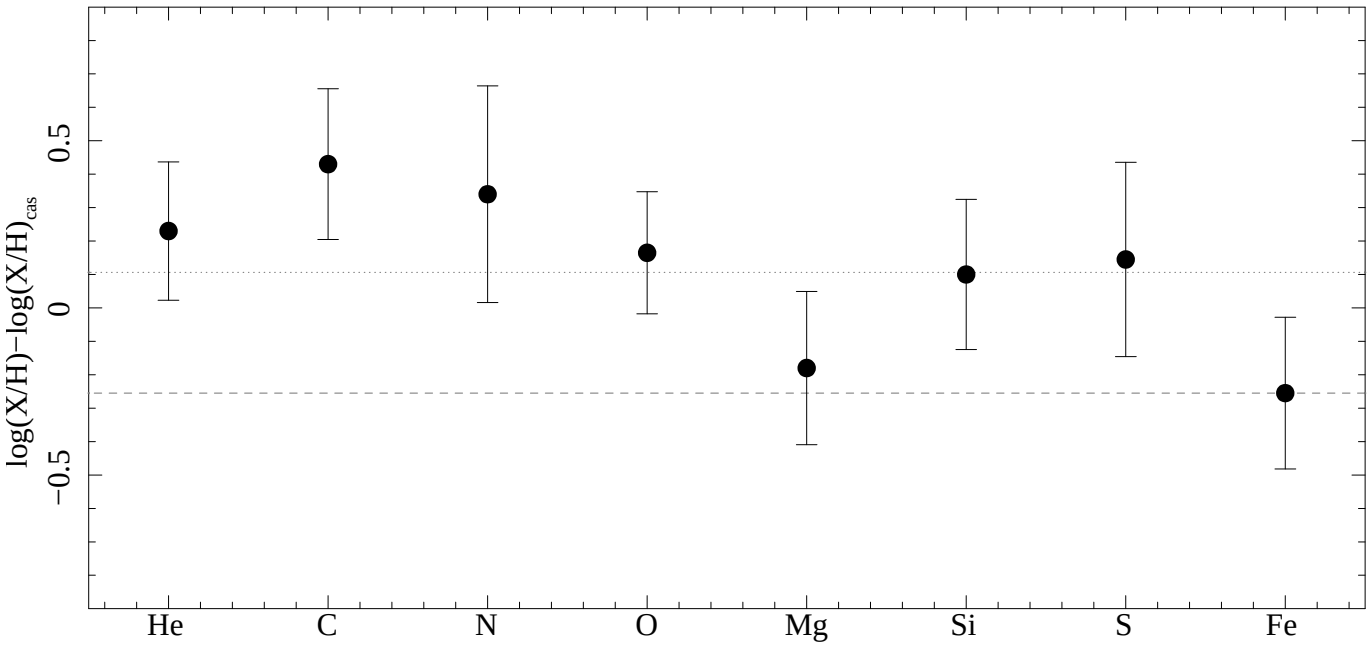

Figure 6.1: Abundance pattern of HIP 60350: values are given relative to the cosmic abundance standard by Przybilla, Nieva & Butler (2008), i.e., the chemical composition of a representative sample of B-stars in the solar neighborhood. The missing sulfur abundance in the cosmic standard is complemented by $\log({\rm S/H}) + 12 = 7.08 \pm 0.11$ derived from the nearby B-star HD 209008 (Nieva & Przybilla, priv. comm.). Systematic errors of 0.1 were added in quadrature to those listed in Table 4.1. The dotted line marks the data points' average, the dashed one the value for iron.

6.1 Dynamical Interaction in Star Clusters

The chemical evolution within the Galactic disk depends on the distance to the center because the gravity induced increasing density of interstellar matter towards smaller radii raises the star-formation rate in the inner regions. With more stars being born, a larger amount of hydrogen will be converted to metals during the evolution of the individual stars. Due to supernovae explosions, those metals are returned to the interstellar medium enhancing its baseline metallicity with time. Later stellar generations are therefore more metal rich than previous ones. The higher star-formation rate in the vicinity of the center is thus expected to result in a Galactic metallicity gradient which is indeed observed (see for instance Daflon & Cunha, 2004). Recalling that HIP 60350 stems from a region $R_{\rm int} = 6.1 \pm 0.6$ kpc away from Milky Way's center and hence closer to it than the Sun, one expects to find a slightly higher metallicity in this star when compared to similar objects in the solar neighborhood. This comparison is done in Fig. 6.1 and can be read as almost uniform relative shift to a larger average metallicity (dotted line in the figure) owing to the error bars. Note that magnesium

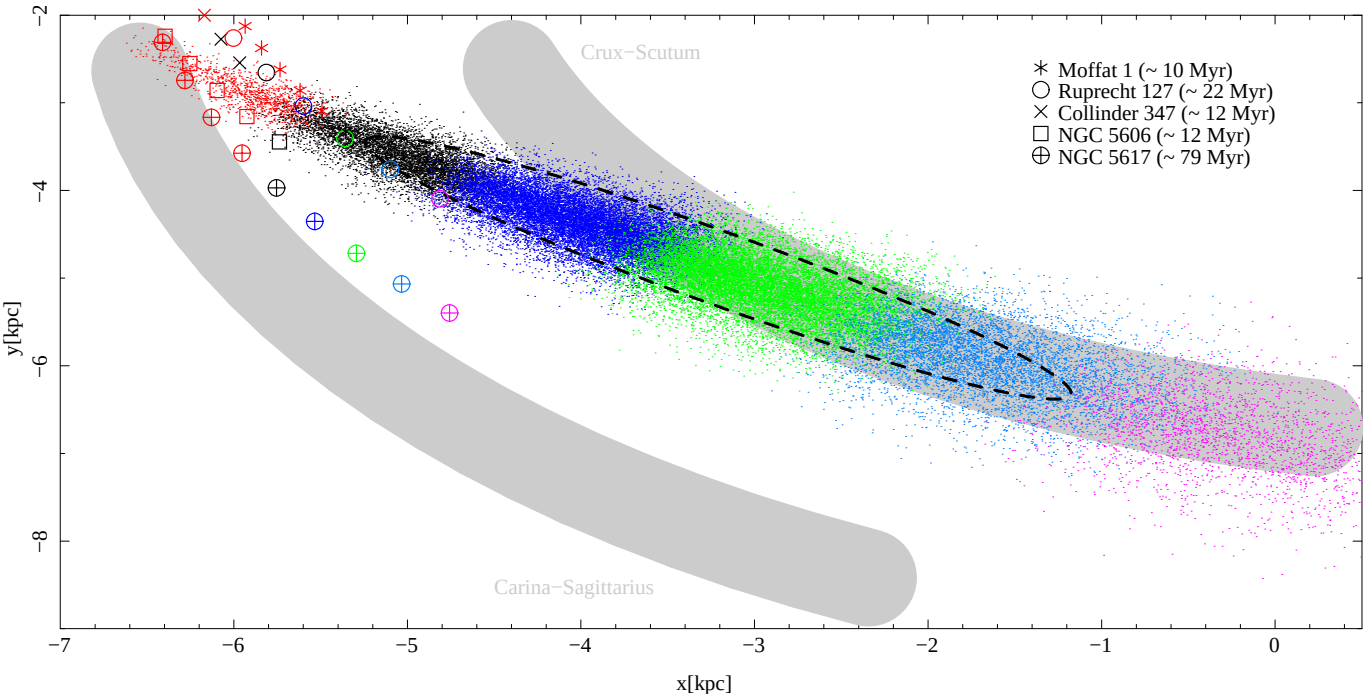

Figure 6.2: Galactic disk intersection region of the sample of orbits (dots): The dashed ellipse marks the 1σ scatter, i.e., it contains $\sim 68\%$ of the data points. Additionally, the trajectories of the best open cluster candidates are depicted using data from Dias et al. (2002). The travel time in Myr is color-coded as follows: < 10 (red), 10-12 (black), 12-14 (dark blue), 14-16 (green), 16-18 (light blue) and 18-20 (magenta). The gray-shaded regions schematically represent the locus of the two spiral arms Crux-Scutum and Carina-Sagittarius 14 Myr ago. Their positions were estimated from the polynomial logarithmic arm model of Hou, Han & Shi (2009) and the Galactic rotation curve of Allen & Santillan (1991).

and iron abundances may be underestimated as there were only very few lines visible for these species leading to less trustable low number statistics. The interpretation of an uniform metallicity enhancement would rule out a significant capture of supernova products by the runaway star. Consequently the supernova scenario could be excluded for HIP 60350 as its extremely high ejection velocity $v_{\rm ej} = 389 \pm 43\,{\rm km\,s^{-1}}$ requires a very close progenitor system leading to a large geometrical cross section. Under this assumption, one may instead focus on dynamical interactions in star clusters to explain the runaway event. A necessary condition for this scenario is the finding of clusters that were close in space and time to the star's disk intersection region. The currently most thorough catalogue of Galactic open clusters is given by Dias et al. (2002). Based on the positions and – if available – velocities therein, those clusters were selected that shared the same region in spacetime as HIP 60350 when its trajectories crossed the Galactic plane. The result of this investigation is summarized in Fig. 6.2. As can be seen there, at least five suitable open clusters could be found: Ruprecht 127 (age in Myr: ~ 22), NGC 5606 (~ 12), NGC 5617 (~ 79), Collinder 347 (~ 12) and Moffat 1 (~ 10). Note that the catalogue contains full three-dimensional velocity information for the first three objects while the others were assumed to move on circular orbits around the Galactic center. Two important things are here to mention: Firstly, accounting for errors in the cluster trajectories analogously to the stellar orbit would noticeably increase the overlap. Secondly, the accumulation of clusters to the left is due to the fact that many promising candidates, e.g., located in the Crux-Scutum spiral arm of the Milky Way, are very likely obscured by interstellar extinction being very strong in this direction and hence have not yet been discovered. Having a closer look at the ages of the above mentioned clusters reveals that three of them are quite similar to the star's travel time $T_{\rm flight} = 14.3 \pm 2.5\,{\rm Myr}$ and to the lower limit of its evolutionary age $T_{\rm evo} = 45^{+15}_{-30}\,{\rm Myr}$ implying an ejection in the initial dynamical relaxation phase of the cluster (Poveda, Ruiz & Allen, 1967). The supersolar helium abundance of HIP 60350 (see Fig. 6.1) might be the consequence of a merger event that occurred in the course of the dynamical ejection as suggested by Leonard (see 1995).

One may wonder why it is absolutely necessary to find open cluster candidates when arguing for the dynamical interaction scenario. In principle, the parent cluster of the runaway star could dissolve during its time of flight, indeed a very likely fate especially for small clusters or associations. However, the time it takes to dissolve depends on the size of the cluster: the bigger the object, the longer the dissolution process. Since the probability for dynamical interactions is growing with the number of bodies involved, almost always the dense, massive and thus long-living clusters with dissolution times considerably exceeding the travel time eject runaway stars. The finding of a cluster is necessary but not sufficient to argue for dynamical ejection since clusters are also sites for supernova explosions.

6.2 Supernova Explosion in a Binary System

As outlined before, the supernova scenario does not require the existence of suitable open clusters or associations because these could have already dissolved due to their possible smallness. On the contrary, observing an α-enhanced abundance pattern should be an unquestionable proof for it. According to the last section, the baseline metallicity of HIP 60350 is expected to exceed the one derived from the solar neighborhood due to abundance gradients in the Milky Way. However, various recent measurements of the Galactic metallicity gradient (e.g. Daflon & Cunha, 2004; Pedicelli et al., 2009; Rudolph et al., 2006) show a large scatter of abundances for individual stars. Hence, the low iron abundance of Table 4.1 may not be in contradiction to the star's birthplace $\sim 6\,\mathrm{kpc}$ away from the Galactic center and may in fact represent HIP 60350's baseline metallicity.

A quantitative interpretation of Fig. 6.1 within the framework of the supernova scenario is far beyond the scope of this work and would require detailed knowledge of the chemical composition and structure of the pre-supernova primary, complex hydrodynamical simulations of the interactions between ejected shell and runaway star and advanced models for the mixing of accreted material within the atmosphere of the secondary. Some qualitative conjectures concerning the observed abundance pattern can yet be made. Provided that the iron abundance is correct, Fig. 6.1 reveals a striking enhancement of the α-elements carbon, oxygen, silicon and sulfur which are characteristic for core-collapsing supernovae. The low value for the α-element magnesium is unexpected and hardly to explain in a qualitative picture, especially as its fuel carbon is so enriched. Perhaps it is also underestimated due to the shortage of analyzable lines. In analogy to HD 271791 (Przybilla et al., 2008), the following scenario can be devised to account for the enhancement in helium and nitrogen as well as for the kinematic properties of HIP 60350. Together with a primary star of at least $25\,M_\odot$ on the zero-age main sequence, it formed a binary system (see Fig. 6.3a). Due to the large mass difference of the two components, their evolution was quite different. The primary quickly burned its hydrogen fuel and started its giant phase while HIP 60350 was and still is on the main sequence. During the expansion to a giant, the primary filled its Roche lobe, i.e., the region around a star in a rotating binary system where matter is bound to it by gravitation (see for instance Hilditch, 2001), leading to mass transfer – for the main part hydrogen – to the secondary. However, the mass overflow was so rapid that the secondary was not able to accrete the material such that it eventually filled its Roche lobe, too, forming a common-envelope around both stars (see Fig. 6.3b). According to Vanbeveren, De Loore & Van Rensbergen (1998), this scenario requires a mass ratio of primary/secondary ≥ 5 as already implied by demanding $M_{\mathrm{pr}} \geq 25\,M_\odot$. The resulting viscous forces between the stars and the common-envelope triggered the spiraling-in of the stellar components until their common-envelope was expelled due to the deposition of orbital energy (see Fig. 6.3c), resulting in a very close binary system (see Fig. 6.3d). By losing its hydrogen shell, the primary became a hot, compact Wolf-Rayet star of approximately $M_{\mathrm{wr}} = 15\,M_\odot$. As mentioned in Sect. 3.3.2 when talking about the effects of radiative pressure, Wolf-Rayet stars are characterized by strong stellar winds leading to non-negligible mass loss. As the hydrogen shell was already ejected at the end of the common-envelope phase, the atmosphere of the Wolf-Rayet star is dominated by helium and nitrogen implying that the star is of class WN. Finding

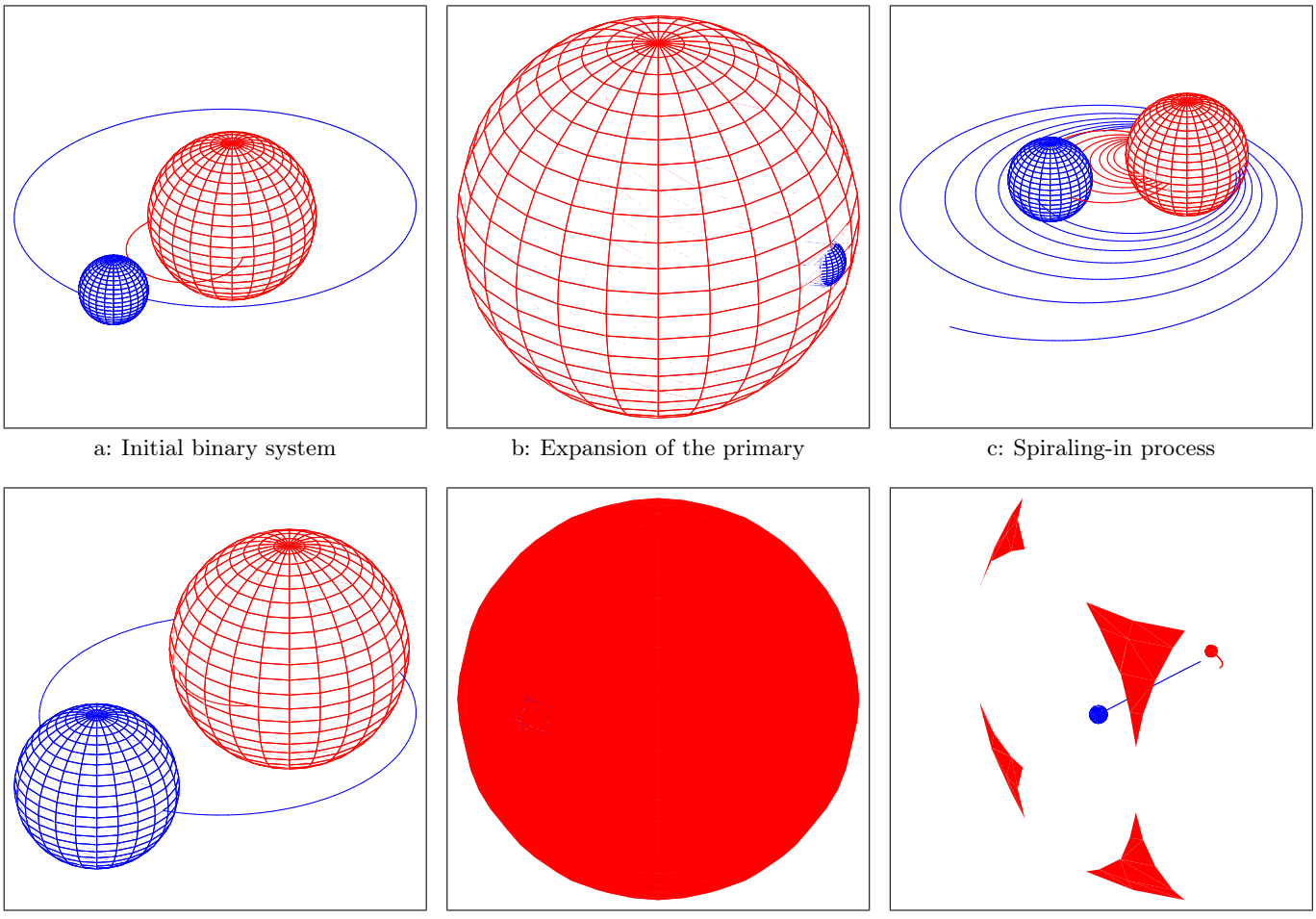

a: Initial binary system
b: Expansion of the primary
c: Spiraling-in process
d: Close binary system
e: Supernova explosion
f: Release of the runaway star

Figure 6.3: Possible supernova progenitor system of HIP 60350: The initial binary system (a) underwent a common-envelope phase caused by the expansion of the primary (red) when becoming a red giant (b). The resulting spiraling-in process of the stars (c) left behind a close system (d) that was eventually disrupted by the supernova explosion of the post-common-envelope primary (e) releasing the runaway star (blue) (f). For details on this figure see Sect. A.3.

a lot of nitrogen is the result of the CNO bi-cycle of hydrogen burning which converts a considerable part of carbon and oxygen into nitrogen when running in equilibrium (Clayton, 1983, Chap. 5.4). Consequently the dense stellar wind, accreted by the secondary star, consisted primarily of these two chemical species hence being responsible for their striking enhancement in Fig. 6.1. While its wind deposited a significant amount of helium and nitrogen on the secondary, the rapid evolution of the Wolf-Rayet star continued and higher nuclear burning stages were ignited in its core eventually leading to the supernova event of Type I b outlined in Sect. 2.4 (see Fig. 6.3e). The α-enriched, ejected shell of the explosion is partly accreted by the secondary giving rise to the observed pattern of Fig. 6.1. Due to the mass loss in the binary system and the associated drop in the attractive gravitational potential, the companion star is released from the left-behind supernova remnant of mass M_{sr} with high ejection velocity $v_{\mathrm{ej}} = 389 \pm 43\,\mathrm{km\,s^{-1}}$ (see Fig. 6.3f) derived in Sect. 5.2. Making some conjectures that simplify things a little bit, one is able to reconstruct the possible progenitor system to see whether it is realistic or not. These assumptions encompass:

1. The supernova remnant is a neutron star (Heger et al., 2003) with typical mass of $M_{\rm sr} = M_{\rm ns} = 1.4\,M_\odot$.

2. Orbits of the post-common-envelope binary system are circular. With P denoting the orbital period and $a_{\rm ra}$ the radius of the orbit of the future runaway star, circularity implies:

$$v_{\rm ra}^{\rm orb} = \frac{2\pi a_{\rm ra}}{P} \tag{6.1}$$

3. Orbital and rotational motions are synchronized meaning that orbital and rotational axes as well as periods equal each other. This is justified by noting that after the spiraling-in process the post-common-envelope system is very close resulting in strong tidal forces. These cause a friction-induced torque that synchronizes the motions (Hilditch, 2001, pp. 152-156). Synchronization constrains the equatorial rotational velocity $v_{\rm rot}$:

$$v_{\rm rot} = \frac{2\pi R_\star}{P} \tag{6.2}$$

4. The supernova explosion is symmetric allowing the post-common-envelope orbital velocity $v_{\rm ra}^{\rm orb}$ of the future runaway star to be related to its ejection velocity $v_{\rm ej}$ with the help of the runaway star's mass $M_{\rm ra}$:

$$v_{\rm ej} = \frac{\sqrt{(M_{\rm wr}-M_{\rm ns})^2 - 2M_{\rm ra}M_{\rm ns} - M_{\rm ns}^2}}{M_{\rm wr}} v_{\rm ra}^{\rm orb} = \frac{\sqrt{M_{\rm wr}^2 - 2M_{\rm wr}M_{\rm ns} - 2M_{\rm ra}M_{\rm ns}}}{M_{\rm wr}} v_{\rm ra}^{\rm orb} \tag{6.3}$$

   The first equality is derived, e.g., in Tauris & Takens (1998) and is valid in this simple form solely for symmetric supernovae and an initially circular system with stationary center of mass. Tauris & Takens also give analytical formulas in the more general case of an asymmetric supernova explosion, a scenario supported by some observations (see van den Heuvel & van Paradijs, 1997) and possibly caused by an asymmetry in the neutrino flux occurring during the iron core collapse. Accounting for the asymmetry introduces additional degrees of freedom parameterized via a "kick" received by the supernova remnant. Consequently, $v_{\rm ej}$ is not only a function of the mass ratio of the involved components but also of their orbital separation and the kick making it impossible to deduce useful constraints on the pre-supernova system from observations.

   The derivation of Eq. 6.3 is based on the fact that the ejection speed of the shell is so large ($\sim 10^4\,\mathrm{km\,s^{-1}}$) that the supernova event can approximately be thought of as going instantaneously from the initial two-body system to a new one with almost identical parameters, the only differences being the diminished primary mass and in case of an asymmetric explosion an additional kick. The task is then to compute the new orbits as function of the initial conditions dictated by the prior system.

Moreover, Kepler's well known third law (Hilditch, 2001, p. 35) is valid in binary systems:

$$\frac{GM_{\rm wr}^3}{(M_{\rm wr}+M_{\rm ra})^2} = 4\pi^2\frac{a_{\rm ra}^3}{P^2} \tag{6.4}$$

G is hereby the gravitational constant. Using $v_{\rm ej} = 389\,\mathrm{km\,s^{-1}}$ and subsequently applying Eqs. 6.3, 6.1 and 6.4 yields $P = 0.9$ days and $a_{\rm ra} = 8.1\,R_\odot$ translating to a relative orbital separation $a = a_{\rm ra}(M_{\rm wr}+M_{\rm ra})/M_{\rm wr} = 10.7\,R_\odot$. Since the radius of HIP 60350 is $R_\star = 2.8 \pm 0.2\,R_\odot$ and that of WN stars with approximately $15\,M_\odot$ is $1.3\,R_\odot \leq R_{\rm wr} \leq 5.3\,R_\odot$ (Hamann, Gräfener & Liermann, 2006) this distance is rather small but not impossible although both stars almost completely fill their Roche lobes $R_{\rm ra}^{\rm Roche} = 2.9\,R_\odot$ and $R_{\rm wr}^{\rm Roche} = 4.7\,R_\odot$ (Hilditch, 2001, p. 161). The situation is further aggravated as $a = 10.7\,R_\odot$ is the separation just before the explosion, but because of mass loss of the Wolf-Rayet star and associated shrinking of the gravitational attraction, a was smaller right after the common-envelope-phase. Note that such close binaries are usually not observed and need special explanations, in this case given by the spiraling-in process during the common-envelope phase. By means of Eq. 6.2, the rotational velocity of HIP 60350 is then given by $v_{\rm rot} = 155\,\mathrm{km\,s^{-1}}$

implying $\sin i \approx 1$ due to $v_{\mathrm{rot}} \sin i = 150 \pm 5\,\mathrm{km\,s^{-1}}$ (Table 4.1). This is also the most likely case as can be seen by the following argumentation: By demanding synchronization of orbital and rotational motions, the rotational axis of the runaway star is perpendicular to its orbital velocity and thus also to its current space velocity $\vec{v}$ as interactions in the two-body problem affect merely the motion in the orbital plane. Hereby, the kick received in an asymmetric supernova as well as interactions with other stellar objects are neglected. Sampling for each of the 50 000 trajectories, which were calculated for HIP 60350, rotational axes $\vec{\omega}$ in the plane normal to $\vec{v}$ and calculating from these axes together with the known line-of-sights $\vec{X}_\star - \vec{X}_\odot$ the sine of the inclination via

$$\sin i = \sqrt{1 - \left(\frac{\vec{\omega} \cdot (\vec{X}_\star - \vec{X}_\odot)}{|\vec{X}_\star - \vec{X}_\odot||\vec{\omega}|} \right)^2} \tag{6.5}$$

results in the distribution displayed in Fig. 6.4. The peak for $\sin i = 1$ is quite natural as one always finds a vector that is perpendicular to $\vec{v}$ and $\vec{X}_\star - \vec{X}_\odot$, namely, their vector product $\vec{v} \times (\vec{X}_\star - \vec{X}_\odot)$. Figure 6.4 reveals that there is zero probability to find inclinations below $\sin i \approx 0.45$ and that $\sin i = 1$ is by far most likely as desired.

Recalling HIP 60350's lifetime $T_{\mathrm{evo}} = 45^{+15}_{-30}\,\mathrm{Myr}$ and travel time $T_{\mathrm{flight}} = 14.3 \pm 2.5\,\mathrm{Myr}$, one recognizes that there was enough time for the massive primary star, which of course was born at the same time as its companion star, to undergo its complete evolution. Hence, the scenario of Fig. 6.3 is more or less consistent with all observational constraints making the supernova ejection mechanism a serious possibility as origin for HIP 60350.

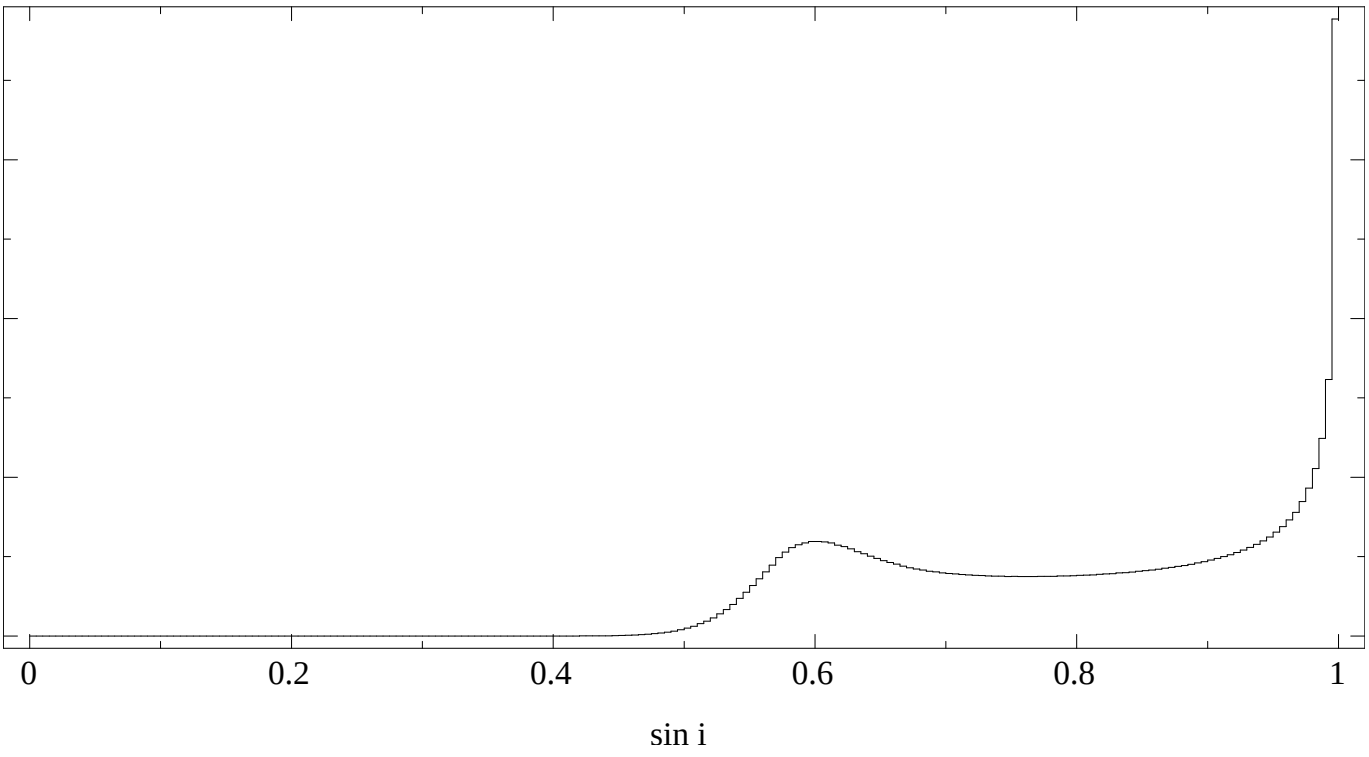

Figure 6.4: Distribution of $\sin i$ in the sample of orbits assuming a binary supernova origin.

7 Summary and Outlook

The last chapter revealed that both common runaway scenarios – dynamical interaction in star clusters and a supernova explosion in a binary system – may be responsible for the peculiar fate of HIP 60350. Based on the available spectra, a clear preference to one of the two cannot be given as both bear advantages as well as disadvantages. Much depends on the interpretation of the acquired abundance pattern of Fig. 6.1 which unfortunately is not very restricting due to the rather large error bars. These uncertainties, considerably exceeding those from systematic effects, mainly result from the interplay of a low S/N ratio of the observed spectra, dependence on very few visible lines and a large projected rotational velocity. The first two problems could be solved by taking high-quality UV spectra with sufficient long exposure times of the object, a difficult task as it would require satellite measurements, e.g., with the Hubble Space Telescope, to avoid photon absorption by Earth's atmosphere. Nevertheless, it would be tempting to see whether unambiguous indications for α-enhancement were present in such spectra.

There are some quite amazing and reliable results obtained in this work: for the first time, a spectroscopic analysis of HIP 60350 was based on NLTE techniques, allowing the stellar parameters, distance and kinematics to be significantly refined with respect to literature (Maitzen et al., 1998; Tenjes et al., 2001). The outcomes of the presented study resolved the contradiction therein that the travel time exceeded the stellar lifetime, and clearly point to a hyper-runaway nature of HIP 60350. It would be the second of its kind after HD 271791. In analogy to the latter, HIP 60350 was also ejected in direction of Galactic rotation to reach its immense current space velocity of $v_{\mathrm{grf}} = 530 \pm 36\,\mathrm{km\,s^{-1}}$. Moreover, the two stars share a similar α-enhancement pattern and can both be interpreted as the surviving component of a binary system that was disrupted by the supernova explosion of a Wolf-Rayet star. Furthermore, the birthplace of HIP 60350 was probably located in the Crux-Scutum spiral arm of the Milky Way (see Fig. 6.2).

The numerical programs and scripts developed in the course of this thesis – for instance to conveniently compute large grids of model atmospheres, to determine the distance to the star via the method of Sect. 5.1, to easily browse through the database of open clusters to find suitable candidates and some slight improvements of the Monte Carlo code for estimating errors – will considerably speed up future analyses and allow more stars to be studied in the future.

Hence, analogous investigations of other B-type stars in the Galactic halo are planned and will help to clarify whether star formation far away from the Galactic disk is possible at all. In the more likely case that these objects are the result of an event prompting them to run away from the Milky Way's plane, their spectroscopic and kinematic examination could give new insights into the processes that trigger the ejection. Hereby, the disruption of a binary system by a supernova explosion is of special interest as it offers a so far not exploited opportunity to gain observational constraints on supernova nucleosynthesis. The comparison with numerical models of supernova explosions, simulations of the interaction of the ejected shell with the runaway star and of the subsequent mixing of supernova ejecta with its atmosphere will allow α-enhancement patterns to be interpreted qualitatively and will help to improve supernova models, leading to a deeper understanding of its underlaying physics.

With these prospects in mind, this thesis together with the International Year of Astronomy 2009 comes slowly to an end.

A Appendix

A.1 Constants and Units

Table A.1: Constants and Units (see e.g. Karttunen et al., 1994)

Constant	Symbol	Numerical value [SI]	Numerical value [cgs]
Gravitational constant	G	$6.673 \cdot 10^{-11}\,\mathrm{m^3\,s^{-2}\,kg^{-1}}$	$6.673 \cdot 10^{-8}\,\mathrm{cm^3\,s^{-2}\,g^{-1}}$
Planck's constant	h	$6.626 \cdot 10^{-34}\,\mathrm{J\,s}$	$6.626 \cdot 10^{-27}\,\mathrm{erg\,s}$
Boltzmann constant	k	$1.381 \cdot 10^{-23}\,\mathrm{J\,K^{-1}}$	$1.381 \cdot 10^{-16}\,\mathrm{erg\,K^{-1}}$
Stefan-Boltzmann constant	σ	$5.670 \cdot 10^{-8}\,\mathrm{J\,m^{-2}\,s^{-1}\,K^{-4}}$	$5.670 \cdot 10^{-5}\,\mathrm{erg\,cm^{-2}\,s^{-1}\,K^{-4}}$
Speed of light	c	$299\,792\,458\,\mathrm{m\,s^{-1}}$	$29\,979\,245\,800\,\mathrm{cm\,s^{-1}}$
Parsec	pc	$3.086 \cdot 10^{16}\,\mathrm{m}$	$3.086 \cdot 10^{18}\,\mathrm{cm}$
Solar Values	**Symbol**	**Numerical value [SI]**	**Numerical value [cgs]**
Mass	$M_\odot$	$1.989 \cdot 10^{30}\,\mathrm{kg}$	$1.989 \cdot 10^{33}\,\mathrm{g}$
Radius	$R_\odot$	$6.96 \cdot 10^{8}\,\mathrm{m}$	$6.96 \cdot 10^{10}\,\mathrm{cm}$
Luminosity	$L_\odot$	$3.85 \cdot\ 10^{26}\,\mathrm{J\,s^{-1}}$	$3.85\,10^{33}\,\mathrm{erg\,s^{-1}}$

A.2 List of Acronyms

CAHA Centro Astronómico Hispano Alemán

CCD Charged coupled devices

CNO Carbon-nitrogen-oxygen

CSIC Instituto de Astrofísica de Andalucía

EW Equivalent width

HR diagram Hertzsprung-Russell diagram

HET Hobby-Eberly Telescope

IUE International Ultraviolet Explorer

LTE Local thermodynamic equilibrium

MPIA Max-Planck Institut für Astronomie

NLTE Non-local thermodynamic equilibrium

ODFs Opacity distribution functions

OS Opacity sampling

PP Proton-proton

SED Spectral energy distribution

SPAS Spectrum Plotting and Analysis Suite

UV Ultra-violet

ZAMS Zero-age main sequence

A.3 Animations

At http://www.sternwarte.uni-erlangen.de/~irrgang/animations/ animated GIF files of Figs. 2.10, 2.11 and 6.3 are available. The animations/figures were created using the computer algebra system Maple 10[1] and a fourth-order Runge-Kutta method to solve the equations of motions resulting from Newton's gravitational law. Assuming the same density for all stars, stellar radii were scaled according to their mass via $R_\star/R_\odot = \sqrt[3]{M_\star/M_\odot}$.

The binary-binary interaction of Fig. 2.10 was calculated in three dimensions with three stars of $M_\star = 5\,M_\odot$ (red, blue, cyan) and one star with $M_\star = 1\,M_\odot$ (black). The initial conditions were chosen such that two separate, bound binary systems approach each other finally resulting in a very close encounter that releases the least massive star with large velocity. It is fascinating to see that the red star exchanges its partner at first, after a certain time, however, the expelled cyan star returns to its previous companion forming a stable triple system with the others.

In contrast to the binary-binary interaction, the following computations on single binary systems were restricted to a planar geometry. The supernova explosion of Fig. 2.11 was simulated in the same way as Eq. 6.3 is derived, namely, by an instantaneous transition from a binary system with $a = 11\,R_\odot$, $M_{\mathrm{pr}} = 15\,M_\odot$ (red sphere) and $M_{\mathrm{ra}} = 4.9\,M_\odot$ (blue sphere) to one with $M_{\mathrm{sr}} = 1.4\,M_\odot$ (red sphere). Note that the expanding shell was added solely for aesthetic reasons but was not accounted for in the calculations.

Figure 6.3 is produced in a similar manner as Fig. 2.11. The spiraling-in of the stars during the common-envelope phase is simulated by adding a velocity dependent friction term in the equations of motions. Starting conditions are determined by demanding that the post-common-envelope system is a close, circular system with the parameters of Sect. 6.2. Masses are again given by $M_{\mathrm{pr}} = 15\,M_\odot$ (red sphere), $M_{\mathrm{ra}} = 4.9\,M_\odot$ (blue sphere) and $M_{\mathrm{sr}} = 1.4\,M_\odot$ (red sphere). The common-envelope as well as the supernova shell were included for the sake of illustration and not implemented in the computations.

[1] http://www.maplesoft.com/products/Maple/index.aspx

Bibliography

Allen, C., & Santillan, A., 1991, RMxAA, 22, 255

Ažusienis, A., & Straižys, V., 1969, Soviet Astronomy, 13, 316

Blaauw, A., 1961, Bull. Astron. Inst. Netherlands, 15, 265

Burbidge, E. M., Burbidge, G. R., Fowler, W. A., & Hoyle, F., 1957, Reviews of Modern Physics, 29, 547

Butler, K., & Giddings, J. R., 1985, in Newsletter of Analysis of Astronomical Spectra, No. 9 (Univ. London)

Cameron, A. G. W., 1957, AJ, 62, 9

Carroll, B. W., & Ostlie, D. A., 1996, An Introduction to Modern Astrophysics, (Reading, Massachusetts et al.: Addison-Wesley), 1st edition

Clayton, D. D., 1983, Principles of Stellar Evolution and Nucleosynthesis, (Chicago and London: The University of Chicago Press), 1st edition

Cutri, R. M., et al., 2003, 2MASS All Sky Catalog of point sources (The IRSA 2MASS All-Sky Point Source Catalog, NASA/IPAC Infrared Science Archive. http://irsa.ipac.caltech.edu/applications/Gator/)

Daflon, S., & Cunha, K., 2004, ApJ, 617, 1115

Dias, W. S., Alessi, B. S., Moitinho, A., & Lépine, J. R. D., 2002, A&A, 389, 871

Fowler, W. A., 1984, Bulletin of the American Astronomical Society, 16, 537

Giddings, J. R., 1981, Ph.D. thesis, Univ. London

Goeppert Mayer, M., 1964, Science, 145, 999

Gray, D. F., 2005, The Observation and Analysis of Stellar Photospheres, (New York: Cambridge University Press), 3rd edition

Gualandris, A., Portegies Zwart, S., & Eggleton, P. P., 2004, MNRAS, 350, 615

Hamann, W., Gräfener, G., & Liermann, A., 2006, A&A, 457, 1015

Heber, U., Edelmann, H., Napiwotzki, R., Altmann, M., & Scholz, R.-D., 2008, A&A, 483, L21

Heger, A., Fryer, C. L., Woosley, S. E., Langer, N., & Hartmann, D. H., 2003, ApJ, 591, 288

Hilditch, R. W., 2001, An Introduction to Close Binary Stars, (Cambridge: Cambridge University Press), 1st edition

Hills, J. G., 1988, Nature, 331, 687

Hoogerwerf, R., de Bruijne, J. H. J., & de Zeeuw, P. T., 2001, A&A, 365, 49

Hou, L. G., Han, J. L., & Shi, W. B., 2009, A&A, 499, 473

Huang, W., Gies, D. R., & McSwain, M. V., 2009, ApJ, 703, 81

Israelian, G., Rebolo, R., Basri, G., Casares, J., & Martín, E. L., 1999, Nature, 401, 142

Karttunen, H., Kröger, P., Oja, H., Poutanen, M., & Donner, K., 1994,Fundamental Astronomy,(New York Berlin Heidelberg: Springer Verlag), 2nd edition

Kurucz, R. L., 1993, CD-ROM 13 (Cambridge: SAO)

Leonard, P. J. T., 1995, MNRAS, 277, 1080

Leonard, P. J. T., & Duncan, M. J., 1988, AJ, 96, 222

Maeder, A., & Meynet, G., 2005, A&A, 440, 1041

Maitzen, H. M., Paunzen, E., Pressberger, R., Slettebak, A., & Wagner, R. M., 1998, A&A, 339, 782

Nieva, M. F., & Przybilla, N., 2006, ApJ, 639, L39

Nieva, M. F., & Przybilla, N., 2007, A&A, 467, 295

Nieva, M. F., & Przybilla, N., 2008, A&A, 481, 199

Ochsenbein, F., Bauer, P., & Marcout, J., 2000, A&AS, 143, 23

Odenkirchen, M., & Brosche, P., 1992, Astron. Nachr., 313, 69

Pedicelli, S., et al., 2009, A&A, 504, 81

Poveda, A., Ruiz, J., & Allen, C., 1967, Boletin de los Observatorios Tonantzintla y Tacubaya, 4, 86

Przybilla, N., Butler, K., Becker, S. R., & Kudritzki, R. P., 2006, A&A, 445, 1099

Przybilla, N., Nieva, M., & Butler, K., 2008, ApJ, 688, L103

Przybilla, N., Nieva, M. F., Heber, U., & Butler, K., 2008, ApJ, 684, L103

Rudolph, A. L., Fich, M., Bell, G. R., Norsen, T., Simpson, J. P., Haas, M. R., & Erickson, E. F., 2006, ApJS, 162, 346

Schaller, G., Schaerer, D., Meynet, G., & Maeder, A., 1992, A&AS, 96, 269

Schlegel, D. J., Finkbeiner, D. P., & Davis, M., 1998, ApJ, 500, 525

Seeger, P. A., Fowler, W. A., & Clayton, D. D., 1965, ApJS, 11, 121

Tauris, T. M., & Takens, R. J., 1998, A&A, 330, 1047

Tenjes, P., Einasto, J., Maitzen, H. M., & Zinnecker, H., 2001, A&A, 369, 530

Tillich, A., Przybilla, N., Scholz, R., & Heber, U., 2009, A&A in press (arXiv:0910.5174)

Tobin, W., 1985, A&AS, 60, 459

Tüg, H., White, N. M., & Lockwood, G. W., 1977, A&A, 61, 679

van den Heuvel, E. P. J., & van Paradijs, J., 1997, ApJ, 483, 399

van Leeuwen, F., 2007, Astrophysics and Space Science Library 350, *Hipparcos*, the New Reduction of the Raw Data (Berlin: Springer)

Vanbeveren, D., De Loore, C., & Van Rensbergen, W., 1998, A&A Rev., 9, 63

Wallerstein, G., et al., 1997, Reviews of Modern Physics, 69, 995

Wallerstein, G., Vanture, A. D., Jenkins, E. B., & Fuller, G. M., 1995, ApJ, 449, 688

List of Figures

List of Tables

Acknowledgements

Many people supported me during the course of this work and their efforts shall never be forgotten nor go unrewarded. And what higher reward can be expected than being mentioned in this groundbreaking thesis?

First of all, I would like to thank most of my teachers at school and university for holding very instructive lectures giving me the necessary scientific background for this work. Furthermore I am grateful to Sonja Schuh for organizing the HET spectrum, Heinz Edelmann and Thomas Kupfer for their help concerning data reduction of Echelle spectra, and the latter together with Sebastian Müller for taking and reducing the TWIN spectra of Calar Alto. Thanks goes also to Stephan Geier for solving the puzzle of shifted radial velocities in the TWIN spectra. Thanks to Alfred Tillich for valuable discussions about orbit computations, Florian Schiller for various pieces of advice and of course for frequently giving me a ride, Heiko A. Hirsch for providing access and support of SPAS and Maria Fernanda Nieva for hints on the use of SPAS and quantitative spectroscopy. I am very grateful to Moritz Böck for proof-reading a part of the thesis and for a lot of hints about its layout, but also for giving assistance to me concerning the use of ISIS, Linux, Jed and programming. A special thanks goes to Manfred Hanke, who invested a considerable amount of his precious time to proof-read the thesis and to patiently solve all my problems which were by any means related to computers (there were many of them) and who also supplied me with many programs and pieces of advice that simplified work.

Three persons deserve special mentioning as they had the most influence on the thesis: first of all I am extremely grateful to Markus Firnstein. Being my roommate makes him my first person of contact resulting in a lot of questions from any field of physics. I am deeply impressed by his patience when answering all of them, no matter how long it takes. Without his daily support, I would not have made it so far. I am greatly thankful to Norbert Przybilla for uncountable explanations concerning the theory of stellar atmospheres, ATLAS, DETAIL, SURFACE, for writing a part of my Ph.D. application, for proof-reading the thesis and for answering the same questions again and again. Of course, special thanks goes to my first supervisor, Uli Heber, not only for making it possible for me to work on this interesting topic in this wonderful building located in this beautiful city of Bamberg, but also for writing the other part of my Ph.D. application and for leaving his office door always open enabling me to ask for pieces of advice whenever necessary.

Thanks to all[1] members of the observatory for the pleasant ambience which makes life easier and much more fun.

Thanks to my second supervisor, Jaroslav Fabian, for managing the formalities in Regensburg allowing me to perform my thesis here at the observatory and for fulfilling all my requests.

Finally, I am grateful to my brother for supporting my studies especially during our common stay in Regensburg. Thanks to my parents for financial as well as non-material support and for letting me go my own way.

[1] On special request of Christian Schmid I would like to point out that he was not scientifically involved in this work by any means.

DECLARATION

Hereby I declare that I wrote this diploma thesis autonomously and that I have not used other resources than those quoted in this work.

ERKLÄRUNG

Hiermit erkläre ich, dass ich die Diplomarbeit selbstständig angefertigt und keine Hilfsmittel außer den in der Arbeit angegebenen benutzt habe.

Bamberg, November 2009 _____

(Andreas Irrgang)